UTRECHT UNIVERSITY

MASTERS THESIS

VIS/NIR Photocurrent Spectroscopy on Organic Semiconductors by Lock-in Amplification

Author:
A.L. VAN DER FELTZ, BSc[‡]

Supervisors:
Prof. dr. B. FRABONI[†]
dr. A. CIAVATTI[†]
Examiners:
Prof. dr. T. PEITZMANN[‡]
dr. D. VAN OOSTEN[‡]

A thesis submitted in fulfilment of the requirements for the degree of Master of Science

in the

Organic Semiconductors and Devices Group
Department of Physics and Astronomy

August 30, 2016

[†]University of Bologna, Viale Berti Pichat 6/2, 40127 Bologna, Italy
[‡]University of Utrecht, Princetonplein 5, 3584 CC Utrecht, The Netherlands

Declaration of Authorship

I, A.L. VAN DER FELTZ, declare that this thesis titled, "VIS/NIR Photocurrent Spectroscopy on Organic Semiconductors by Lock-in Amplification" and the work presented in it are my own. I confirm that:

- This work was done wholly or mainly while in candidature for a research degree at this University.
- Where any part of this thesis has previously been submitted for a degree or any other qualification at this University or any other institution, this has been clearly stated.
- Where I have consulted the published work of others, this is always clearly attributed.
- Where I have quoted from the work of others, the source is always given. With the exception of such quotations, this thesis is entirely my own work.
- I have acknowledged all main sources of help.
- Where the thesis is based on work done by myself jointly with others, I have made clear exactly what was done by others and what I have contributed myself.

Signed: _____

Date: _____

"Ché non fa scïenza, sanza lo ritenere, avere inteso"
"Knowledge comes, of learning well retain'd, unfruitful else."

Dante Alighieri, Divina Commedia 'Paradiso', canto V, l.41.

UTRECHT UNIVERSITY

Abstract

Faculty of Science
Department of Physics and Astronomy

Master of Science

VIS/NIR Photocurrent Spectroscopy on Organic Semiconductors by Lock-in Amplification

by A.L. VAN DER FELTZ

Photocurrent spectroscopy provides a nondestructive method to study optoelectronic properties of semiconducting materials based on the photo-absorption induced current. This research reports of the successful development of a novel photocurrent spectroscopy setup that uses lock-in amplification to measure currents down to $0.1\,\mathrm{pA}$ with a spectral resolution of $0.63\,\mathrm{nm}$. The setup has been applied to study three small molecule organic semiconductors of various morphology. Measurements on rubrene single crystals indicate an oxidation triggered antibatic photocurrent response with respect to the spectral absorption. Rubrene thin film samples revealed an impact of the film thickness on photo-conductive behavior up to a thickness of $52\,\mathrm{nm}$. A comparative study has been conducted on different morphologies of the novel organic semiconductor TIPS pentacene. The TIPS pentacene inkjet-printed crystal was studied for the first time. These crystals exhibit a photocurrent response and bandgap equivalent to single crystalline samples. Finally, this research reports the first measurements on TIPG pentacene. A pentacene derivative similar to TIPS pentacene with substituted germanium (Ge). The Ge substitution causes a slight blueshift but no further significant change in the photo-conductive response of the material.

Contents

Declaration of Authorship i

Abstract iii

Contents iv

List of Abbreviations vi

1 Introduction 1
- 1.1 Preface to Organic Semiconductors . . . 1
- 1.2 Outline of this research . . . 3

2 Theory 4
- 2.1 Organic Semiconductors . . . 4
  - 2.1.1 Van der Waals Forces . . . 4
  - 2.1.2 Bandstructure . . . 5
    - 2.1.2.1 Davydov Splitting . . . 6
  - 2.1.3 Morphologies . . . 6
    - 2.1.3.1 Single Crystals . . . 7
    - 2.1.3.2 Thin Films . . . 7
    - 2.1.3.3 Inkjet Printed Crystals . . . 7
  - 2.1.4 Conductivity in Molecular Organic Semiconductors . . . 7
    - 2.1.4.1 Defects, Impurities and Trapping . . . 8
    - 2.1.4.2 Excitons . . . 9
  - 2.1.5 Materials . . . 10
    - 2.1.5.1 Rubrene . . . 10
    - 2.1.5.2 TIPS Pentacene . . . 11
    - 2.1.5.3 TIPG Pentacene . . . 11
  - 2.1.6 Photocurrent Spectroscopy . . . 12
    - 2.1.6.1 Photoconductivity Phenomena . . . 13
- 2.2 Optics . . . 14
  - 2.2.1 Spectroscopy . . . 14
    - 2.2.1.1 Diffraction Gratings . . . 14
    - 2.2.1.2 Resolution . . . 15
  - 2.2.2 Optical Throughput . . . 16
    - 2.2.2.1 Magnification . . . 17
  - 2.2.3 Detectors . . . 17
    - 2.2.3.1 Photodiode . . . 17
    - 2.2.3.2 Pyroelectric . . . 18
- 2.3 Lock-in Amplification . . . 19
  - 2.3.1 Phase-Sensitive Detection . . . 19
  - 2.3.2 Low-Pass Filters . . . 19
  - 2.3.3 Two-phase Detection . . . 19

3 Methodology 20
- 3.1 Experimental Setup . . . 20
  - 3.1.1 Setup Part I: Spectral Source . . . 21
  - 3.1.2 Setup Part II: Signal Control . . . 21
    - 3.1.2.1 Monochromator . . . 21

3.1.3 Setup Part III: Signal Detection . . . 23
3.1.3.1 Noise . . . 23
3.1.3.2 Lock-in Amplifier . . . 25
3.1.4 Measurement Protocol . . . 28
3.2 Samples . . . 29
3.2.1 Electrodes . . . 30
3.2.1.1 Photocurrent Anisotropy . . . 30

4 Results **31**
4.1 Setup Parameters . . . 31
4.1.1 Spectral Calibration . . . 31
4.1.1.1 Monochromator Broadening . . . 32
4.1.2 Photon Flux . . . 33
4.1.3 Signal Processing . . . 34
4.1.4 Noise Analysis . . . 35
4.2 Rubrene . . . 36
4.2.1 Photocurrent in Rubrene Single Crystals . . . 36
4.2.1.1 Symbatic and Antibatic Photocurrent Response . . . 36
4.2.1.2 Photocurrent Anisotropy . . . 37
4.2.2 Photocurrent in Rubrene Thin Films . . . 38
4.2.2.1 Coplanar TOP electrodes . . . 38
4.2.2.2 Coplanar and Biplanar Electrode Geometries . . . 41
4.2.3 Photocurrent in Rubrene Single Crystals vs Thin Films . . . 42
4.2.3.1 Coplanar TOP Electrodes . . . 42
4.2.3.2 Coplanar and Biplanar Electrode Geometries . . . 42
4.3 Pentacene . . . 44
4.3.1 Photocurrent in TIPS Single Crystals . . . 44
4.3.2 Photocurrent in TIPS Thin Films . . . 45
4.3.3 Photocurrent in TIPS Printed Crystals . . . 46
4.3.4 TIPS Morphology Comparison . . . 47
4.4 TIPG . . . 48
4.5 Experimental Error . . . 49
4.5.1 Systematic Error . . . 49
4.5.2 Statistical Error . . . 49

5 Discussion **50**

6 Conclusions **52**

7 Outlook **53**

Acknowledgements **54**

List of Figures **55**

List of Tables **57**

A Etendue **58**

B Detector Specifics **59**

C Noise **61**

Bibliography **63**

Glossary **67**

List of Abbreviations

Notation	Description
AC	alternating current
AFM	atomic force microscopy
C	carbon
CB	conduction band
DC	default current
FET	field-effect transistor
FWHM	full width at half maximum
GaAs	gallium arsenide
GaN	gallium nitride
Ge	germanium
Hg	mercury
HOMO	highest occupied molecular orbital
IP	inkjet printed
LP	low-pass
LUMO	lowest unoccupied molecular orbital
NA	numerical aperture
NEP	noise equivalent power
OFET	organic field-effect transistor
OLED	organic light emitting diode
OMBE	organic molecular beam epitaxy
OSSC	organic semiconducting single crystal
PC	photocurrent
PD	photodiode
PED	pyroelectric detector
PET	polyethylene terephthalate
PLL	phase-locked-loop
PSD	phase-sensitive detector
PVT	physical vapour deposition
PZT	lead zirconate titanate
QTH	quartz tungsten halogen
RMS	root-mean-squared
SC	single crystal
SD	standard deviation
Si	silicon
TIPG	TIPG pentacene
TIPS	TIPS pentacene
TTL	transistor-transistor logic
UVS	ultraviolet enhanced
VB	valence band

To my friends and family

Chapter 1

Introduction

Perhaps you are using them right now, whilst reading this thesis from your computer screen. Or maybe, for those who prefer reading from paper, in a few years a printed version is commercially available. Both are, or might be, possible thanks to increasing knowledge of the application of semiconductors. Presently an alternative for the rare-earth element inorganic semiconductors is gaining interest rapidly. Organic semiconductors provide exciting new opportunities for research and industry. They are becoming increasingly important also in everyday life in electronic devices such as your computer screen or tomorrow's printed organic semiconductors in the form of flexible sheets.

1.1 Preface to Organic Semiconductors

Semiconductors in Society
Semiconductors are a crucial part in electronic circuitry. The steady digitization of society has fueled an increasing demand for the semiconductors used in the computer chips, essential for that development[58]. Traditionally these semiconductors are made of inorganic materials such as silicon (Si), gallium arsenide (GaAs) or gallium nitride (GaN). However, organic semiconductors rapidly gain interest as alternative to their inorganic counterparts[33].

Organic semiconductors open up new doors in terms of fabrication techniques, cost reduction and applicability in devices. Furthermore, the virtually unlimited availability of organic material, compared to the scarcely available rare-earth elements in inorganic semiconductors, offer a solution to the ever increasing demand in electronics. Additionally, the unrestricted access to organic material allows the fabrication of organics semiconductors anywhere. Meanwhile the elements found in inorganic semiconductors originate primarily from mines in China, increasing also political and economic interests[3]. Last but not least, the organically based semiconductors leave a smaller ecological footprint than the inorganic semiconductors.

The significance of organic semiconductors is exemplified by the i-FLEXIS project that encompasses this research[23]. i-FLEXIS is a European consortium between academia and industry aimed at the development and incorporation of organic semiconductors in radiation detection applications. The objective, taken from the project website, combines some of the advantages organic semiconductors have to offer society:

> The target of i-FLEXIS is the development of an innovative, large-area and low-cost integrated X-ray sensor system based on heterogeneous components, away from silicon technology or other similar covalent materials based devices/systems.

Advantages and Applications
The interest in organic semiconductors derives largely from diverse properties making possible the fabrication of new, low-cost and easily tunable devices[46]. The relatively low melting and boiling temperatures are such properties. They permit lower processing temperatures, enabling a broad range of fabrication and processing techniques inapplicable to inorganic semiconductors[35]. Another welcome property of many organic semiconductors is their solubility in organic solvents. Solubility further adds to the amount of available techniques, for example wet processing[80].

The abundance of fabrication methods reduces associated costs and makes it possible to produce different morphologies[17, 18, 30]. An interesting example is the possibility to make large area films. Films are often the preferred morphology for devices thanks to their large active area. Additionally, the fabrication of mechanically flexible morphologies has sparked a variety of research and industrial applications.

Furthermore the substrates onto which the semiconducting material is deposited are no longer restricted to high-temperature resistant material, such as glass. One can select from a variety of possible substrates. Polyethylene terephthalate (PET) is such a material that offers a flexible substrate. The fabrication of flexible organic field-effect transistors (OFETs) is an excellent example of the flexible devices made possible by the combination of the aforementioned substrates and mechanically bendable organic morphologies[22, 55].

Another interesting property of organic semiconductors is there chemical tunability. The variety of available organic semiconducting compounds is due to the relative ease with which new materials can be synthesized or existing materials are altered. Consequently organic semiconductors can be chemically adjusted, changing their properties to better fit application purposes[16].

The appliance of organic semiconductors as X-ray detectors is such an application for which their tunability is of specific interest. Organic semiconductors are proposed as direct[1] detectors of ionizing radiation, converting the high energy radiation directly into electrons that are measured as an electrical signal[24, 25]. The mechanical flexibility and possibility to fabricate semiconductors with large active area fuel the interest in organic radiation detectors.

Generally high stopping power is preferred for X-ray detectors. Increased stopping power increases the probability that the radiation interacts with the detector material and is absorbed. This is an issue for organic detectors due to the relatively light elements in organic compounds[2]. The tuning the organic semiconductor by substituting atoms in the organic detector for heavier elements might offer a solution as the stopping power is increased. This tunability enables a wide range of applications from high stopping power detectors to specific applications of X-ray detection in healthcare that prefer detectors with less stopping power. Organic semiconductors allow radiation detectors made of all-organic material equivalent to organic tissue. As a result organic semiconductors also enable biocompatible device applications[82].

Challenges and Hurdles

The scientific research concerning organic semiconductors still trails behind that of inorganic semiconductors[9, 56]. Consequently there is still much to be gained in the understanding of the electronic transport mechanism and photoelectronic properties of the involved organic materials.

Moreover, typically organic materials are more sensitive to oxidation and humidity than inorganic materials. The oxidation changes the molecular structure of the semiconductor affecting associated properties. As a result organic semiconductors display stability issues originating from oxidation over time or environmental changes in humidity. In general, the role of defects in the material's structure, such as oxidation, has proven to be significant in the behavior of organic semiconductors. The affected stability limits performance capabilities of organic semiconductor applied in devices.

[1] The indirect mode of operation makes use of scintillators. These absorb the radiation and re-emit photons in the visible spectral range. The re-emitted, visible photons then are detected and converted to an electrical readout signal.

[2] Organic compounds typically have a lower atomic Z number than inorganic materials. The stopping power is dependent on the interaction cross-section of the material that depends on Z.

1.2 Outline of this research

The primary aim of this research is the development of a novel experimental setup for photocurrent spectroscopy to investigate optoelectronic properties of semiconducting materials. Subsequently this technique is applied to three different organic semiconductors. These materials are selected with the intention to firstly offer a validation of the setup's performance. The goal for the second selection is to study the impact of different fabrication techniques on the material's performance. The experimental aim for the last material is to examine the effect on the performance due to the substitution of heavier elements in the material's molecular structure.

Chapter 2

Theory

In this chapter the relevant theoretical concepts are introduced for photocurrent spectroscopy by means of lock-in amplification. It contains an introduction on organic semiconductor theory, then a part considering the optics and finally a part concerning the theory of lock-in amplification.

2.1 Organic Semiconductors

Organic semiconductors differ from their inorganic counterparts in several properties. In the following section an introduction is given concerning the theory relevant to organic semiconductors physics.

2.1.1 Van der Waals Forces

The common[1] distinction between organic and inorganic compounds is that the former consist of carbon-based material. From this broad category[2] the solid molecular organic semiconductors particularly are of interest as the counterpart to inorganic semiconductors. Molecular organic semiconductors are carbon-based compounds with intra-molecule covalent atom bonding and inter-molecule Van der Waals bonding. Conversely, inorganic semiconductors only exhibit covalent bonding[61]. This distinction has significant consequences for the crystal lattice structure and electronic bandstructure.

Molecular organic semiconductors consist of benzene molecules. These groups of carbon (C) atoms are held together by conjugated bonds: alternating single and double covalent carbon-carbon bonds, shown schematically as Kekulé structure[3] in fig. 2.1a. Carbon is a IV-type element with four valence electrons meaning that two electrons are bound in σ bonds[4] along the benzene ring and the third bound to the hydrogen atom. The double bond is due to the fourth valence electron that leaves a nonhybridized p_z orbital in the plane perpendicular to the benzene ring. It can form π bonds with free valence electrons on adjacent C-atoms. This characterizing feature, shared by all molecular organic semiconductors, allow them to form molecular p orbitals.[46] When a bond is formed the orbital is said to be occupied. These Van der Waals type orbitals in their empty and filled states respectively form the conduction band (CB) and valence band (VB) known from inorganic semiconductor bandtheory. The Van der Waals-bonding based conduction- and valence bands set apart organic from inorganic semiconductors.

[1] No clear definition of the term 'organic' exists. The concept organic derives from a historic notion of vitalism; an element of 'life', setting apart living organisms from lifeless things. Later organic has been associated with molecules containing carbon, due to their presence in all living organisms. The term is still used for most materials containing carbon, although many exceptions exist.

[2] Specifically organic semiconducting polymers should be mentioned as an important subcategory. However, although their semiconducting properties are closely related, polymeric organic semiconductors will not be treated in this research.

[3] Note a critique on the Kekulé representation that it suggest that the double bonds are between determinate atoms whereas the bonds actually are delocalized and the benzene resonates between the possible bond configurations.

[4] The s orbitals and p orbitals along with σ and π bonds are part of chemistry nomenclature. s and p denote the atomic orbital occupied by the electron according to the Aufbau Principle. σ bonds are made in the axis between s or p orbital electrons of two adjacent atoms while π bonds are bond parallel to, but outside of, the axis.

2.1.2 Bandstructure

The bandstructure of allowed, quantized energy states follows from solving the quantum mechanic electron wave-equations. Three electrons are covalently bound in molecular orbitals within the benzene structure and to the hydrogen. The remaining free electron occupies a p_z molecular orbital. Hence organic semiconductors have a bandstructure of molecular orbitals. Figure 2.1b is a schematic representation of these orbitals. On either side the sp_2 and p_z orbitals are shown for separate atoms and in the center part the bound case with formed σ and π bonds.

Electrons can be excited to unoccupied higher energy states. When they are, they leave behind vacant energy states. Instead of a vacant state, it can also be regarded as a state that is occupied by a virtual particle with opposite charge. These virtual particles are commonly referred to as holes. The negatively charged electrons and positively charged holes attract each other by Coulombic interaction. Excited electrons can recombine with holes when their energies match. The excited electron then relaxes back to the VB, neutralizing the hole.

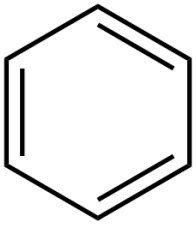

2.1 (A) Schematic Kekulé structure representation of benzene. Single bonds and delocalized double bonds are illustrated as single and double lines between the carbon atoms located on the stucture angles. Hydrogen atoms are ommitted.

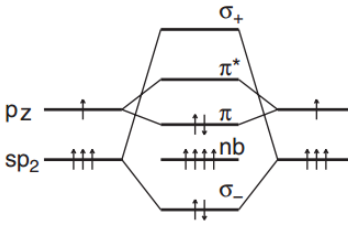

2.1 (B) The energy level diagram for interacting carbon atoms. The sp_2 and p_z orbitals for both unbound atoms are shown on the outer energy levels. They form σ, π and unbound molecular states in the interacting state shown in the center. *Image from* Stallinga [70]

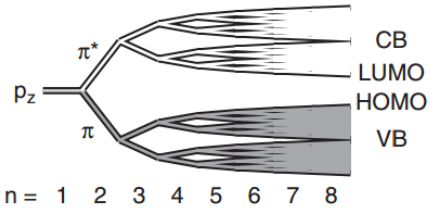

2.1 (C) There is decreased degeneracy when the number of n carbon atoms and p_z orbitals increases. High n results in a CB and VB separated by a bandgap. The HOMO and the LUMO are the states on either side closest to the bandgap. *Image from* Stallinga [70]

A semiconductor contains many molecules that all interact with nearby molecules through their inter-molecular Van der Waals bonding. The interaction lifts the degeneracy of energy levels and causes a splitting of energy levels. In section 2.1.2.1 an example specific to organic semiconductor is treated in more detail. The splitting of energy states increases the amount of accessible states into which electrons can be excited, illustrated in fig. 2.1c. Besides the splitting, the Van der Waals bonding and correlated spacing between the molecules, may cause energy states of adjacent molecules to interact such that they overlap. For $n \gg 1$ molecules and sufficient overlap of the states, instead of discrete energy levels localized per atom, the semiconductor rather has delocalized energy bands; the conduction band (CB) and valence band (VB).

The most interesting of the states within these bands are the highest occupied molecular orbital (HOMO) and the lowest unoccupied molecular orbital (LUMO) on either side of the bandgap. The HOMO contains the electrons in the groundstate with the highest energy and therefore that are most likely to be excited into the LUMO. The bandgap is the material specific range of energy levels that electrons quantum mechanically are prohibited to occupy. The

bandgap is a crucial characteristic for semiconductors as it is the minimally required electron excitation energy to enter the excited states in the CB. Electrons in the CB may function as charge-carriers[5] contributing to the conductivity of the semiconductor which will be further addressed in section 2.1.4.

2.1.2.1 Davydov Splitting

In 1948 A.S. Davydov established a fundamental property of organic semiconductors now known as Davydov splitting[61]. The electronic bandstructure exhibits Davydov splitting as a result of the Van der Waals bonding. It is due to the interaction of superimposed molecular orbitals. Considering the simplified case of a dimer, a pair of equivalent adjacent molecules, their wave-functions couple $\phi_D = \phi_1\phi_2$. When a one of the two molecules is excited, the dimer wavefunction becomes a linear superposition $\phi_D^* = \frac{1}{\sqrt{2}}(\phi_1\phi_2^* \pm \phi_1^*\phi_2)$ according to the quantum mechanical principle of indistinguishability. As a result of the Van der Waals potential between the molecules the energy levels are different, splitted, for the different linear positions: $E_D = E_0 + E^* + D' \pm I_{12}$. Where $E_0 + E^*$ is the energy of the ground state added with the energy of a single excited molecule if there was no interaction. D' denotes the Coulomb interaction energy between a molecule in the ground state and one in the excited state. I_{12} is the energy associated with the resonance between the two quantum states in the superposition. The energy difference between the two resonating states I_{12} is half the Davydov splitting energy ΔE_D given by eq. 2.1:

$$\Delta E_D = \frac{I_{12}}{2} = \frac{1}{2}\langle\phi_1^*\phi_2|V_{vdw}(\vec{r},\vec{r}')|\phi_1\phi_2^*\rangle \tag{2.1}$$

The Van der Waals potential is expressed by $V_{vdw}(\vec{r},\vec{r}')$ and depends on the distance and relative orientation between the molecules. Consequently the magnitude of the Davydov splitting is closely related to the the relative positioning of the semiconductor's molecules.

2.1.3 Morphologies

Beside the bandstructure (section 2.1.2) also the crystallization of organic semiconductors is influenced by the Van der Waals force. The correlated influence of Van der Waals bonding on the bandstructure and crystallinity, the crystalline order[6], is an important motivation to investigate the impact of different morphologies on the optoelectronic properties in organic semiconductors .

The Van der Waals force's relative weakness[7] is expressed in the degree of crystalline order, susceptibility for defects and the material's rigidity. These properties are characteristic for molecular organic semiconductors of various morphologies and corresponding crystallinitiy. Three types of those morphologies are single crystals, thin films and inkjet printed crystals.

[5] The type of charge carrier in organic semiconductors is a debated topic. There is support for the common notion of electrons freely moving through the conduction band with their hole counterparts in the valence band. The other side argues for polaron charge carriers. This concept entails that an electron causes a lattice deformation (phonon) and a resulting polarization. The actual carrier then is an electron-phonon combination[70]. This research will not further address this distinction and uses the general term 'charge-carrier'.

[6] The aforementioned disorder in the various organic semiconductor morphologies is not associated with broken chemical bonds. The crystalline disorder occurs on a molecular level while the covalent bonds within the organic molecules remain intact. This is unlike the disorder in inorganic semiconductors. The consequences of disorder do however strongly affect the conductive properties of molecular organic semiconductors.

[7] From the tight binding model a $\sim$0.1 eV interaction integral is calculated for Van der Waals compared to $\sim$4 eV for covalent bonds[13, 46].

2.1.3.1 Single Crystals

The single crystal (SC)[8] is the best performing morphology in terms of charge-carrier mobility, exciton diffusivity, defect concentration and operational stability[55]. This is largely due to the fact that single crystals are the form with the highest degree of crystalline order, chemical purity and suffer less from grain boundary effects. Combined with the dense packing of SC and the low density of defects, their surfaces are more resistant to oxidation. Especially the possibility of making high-quality crystal interfaces is an important result for qualitative p-n junction in organic transistors.

The minimized disorder in SC allows studying their physical behavior without being masked by trapping and scattering due to defects[38]. A characteristic property that is studied is the anisotropy seen for crystalline organic semiconductors. The carrier-mobility depends on the crystal axis as a consequence of the π bond packing along that direction.

Single crystals are a common morphology and are easier to fabricate than thin films. However, the biggest disadvantages to SC's are that they are rigid materials with a relatively small active area. Therefore SC's are no ideal solution for many applications.

2.1.3.2 Thin Films

Thin films often are the preferred morphology for practical purposes thanks to their large ativea area and flexible form. However, they exhibit performance issues related to their molecular structure. The molecular structure of thin films generally show less order, a large number of imperfections and are dominated more by effects due to grain boundaries. The increased difficulty in fabrication techniques for thin films results in significant disorder that dominates thin film performance in terms of charge-carrier mobility, exciton diffusivity, defect concentration and operational stability.

Moreover, the molecular structure of a film is strongly affected by the structure of the substrate on which the film is grown. In fact, it has been observed that films contain coexisting phases for the bulk and the material close to the film-substrate interface. This distinct feature has much more impact for thin films with a large surface-to-bulk ratio compared to bulky single crystals[22].

Furthermore thin films show increased sensitivity for deteriorating caused by stress, such as electrical bias and aging. The disorder-limited properties make thin films more complicated to study compared to single crystals[55].

Thin films with thicknesses going down to several nanometers are available. Films with such thickness can easily be laminated onto a substrates by means of electrostatic attraction.

2.1.3.3 Inkjet Printed Crystals

Inkjet printing presents a novel technique that deposits material directly onto a substrate effectively printing a crystal of arbitrary thickness[68]. It allows low-cost production of organic semiconductors but the technique does not provide much control of the crystallization process, affecting the material purity and crystalline order. The resulting samples indicate localized order (see section 3.2). Furthermore it is easy to make large area and mechanically flexible samples. The thickness of these inkjet printed (IP) crystals resembles that of single crystals rather than thin films, presenting an interesting intermediate morphology in terms of thickness and crystalline order.

2.1.4 Conductivity in Molecular Organic Semiconductors

The conductivity of any medium depends on the ability of charge-carriers to travel through the medium. The mechanism how charge-carriers drift through organic semiconductors is a debated topic between two theoretic schools, known as the Poole-Frenkel and hopping transport[70].

[8] In literature organic semiconducting single crystal is sometimes abbreviated as OSSC. However, all considered samples in this research are organic semiconductors. Therefore, avoiding the misinterpretation that the other samples are not organic semiconductors, this research uses the abbreviation SC.

Poole-Frenkel theory is derived from inorganic semiconductor bandtheory. It argues that charge-carriers are locally bound in HOMO states but can be exited to the LUMO and travel through the medium, contributing to the current. To travel through these bands the LUMO and HOMO of accessible states need to be well-delocalized so that adjacent molecular orbitals overlap, resulting in Davydov splitting (see section 2.1.2.1)[70]. However the Van der Waals type bonding between adjacent molecules is relatively weak. This causes charge-carriers rather to be locally bound to molecules on the crystal lattice instead of having delocalized planewaves throughout the material.

Hopping transport of charge-carriers is the alternative paradigm related to molecular localized charges. It states that charge-carriers are practically always trapped in localized states. Carriers only relocate by instantaneous 'hopping' between these local traps without first entering the LUMO.

The parameter describing how fast charge-carriers drift through the medium for an applied electric field is called the charge-carrier mobility μ. The conductivity σ depends on the mobility and the density of the charge-carriers $n = {}^{N}/_{V}$ that are negatively charged and the positively charged holes p as illustrated in eq. 2.2.

$$\sigma = e(n\mu_n + p\mu_p) \tag{2.2}$$

2.1.4.1 Defects, Impurities and Trapping

In section 2.1.3 the importance of defects was mentioned in organic materials. The weakly bound molecules in the crystal make it prone to defects. Basically[9] the distinction between impurity defects and structural defects can be made. The former results from alien molecule or atom substitution for the host particles. For example substituted oxygen atoms due to oxidation of the material (see page 8). The latter can roughly be subdivided in point defects, such as vacant sites and dislocations in the crystal lattice, and grain boundaries, naturally found at interfaces and surfaces, but occasionally in the bulk of the material.

The shared consequence of defects is a difference in the available valence electrons compared to the regular crystal lattice. These added, missing or differently bound electrons present new energy levels in the bandstructure. Charge-carriers can occupy these levels. Depending on their energy, these levels may present states onto which the carriers get locally bound or recombine. The bound carrier is no longer able to drift through the medium and add to the current. The carrier is said to be trapped. Depending on the energies and density associated with the traps, the conductive properties of the semiconductor may be limited.

Oxidation

Oxidation is a common phenomenon for organic materials and consequently oxygen impurities are a prevailing type of defect for organic semiconductors. Oxidation occurs at the organic-oxygen interface at the material surfaces. Oxygen impurities can be created from that surface downward into the bulk following an exponential decay with depth. The oxidized material ends up with an altered chemical structure (see for example fig. 2.3 in section 2.1.5.1) that leads to different optoelectronic properties.

An important feature of the oxidation process is that it is triggered by light[41, 71]. In fact, some organic samples kept in a dark, pure oxygen chamber remain unoxidized[52]. Moreover, the penetration depth of the incident light that triggers the oxidation also determines the depth upto which defects may form. Consequently the oxygen traps have a density distribution from the surface downward following a Beer-Lambert law with a coefficient proportional to the absorption coefficient α. Changing the the wavelength of the incident light then changes the depth of the oxidation.

[9] An extensive treatise on crystallographic defects goes beyond the scope of this research. Good introductions on the type of defects and their impact on the conductivity in organic semiconductors can be found in Bube [9] and Schwoerer and Wolf [61]

[10] The large spread in mobility values is due to the impact of different morphologies. Typically the highest value correspond to high crystalline order morphologies such as the single crystalline form. Lower mobilities have been found for thin film and amorphous morphologies.

TABLE 2.1: Material properties of the inorganic semiconductor amorphous Silicon[31, 55, 70, 77] and organic semiconductors Rubrene[25, 43, 54, 55, 59, 78, 79] and Pentacene[11, 27, 39, 47, 53].

	Si	Rubrene	Pentacene
Bandgap E_g [eV]	1.12	2.2	1.8
Mobility[10] μ [$\mathrm{cm}^2/\mathrm{V/s}$]	1-500	20-40	1.4-30
Dielectric constant ϵ_r [$\mathrm{F\,m}^{-1}$	11.9	2.65	3
Exciton Lifetime τ [µs]	$> 10^{-3}$	~ 100	$> 10^{-3}$
Exciton Diffusion length l [$\mu\mathrm{m\,V}^{-1}$]	> 1	$3 \sim 8$	> 1

2.1.4.2 Excitons

Excitons[11] are bound pairs of charge-carriers and oppositely charged holes. The charged constituents are held together by Coulombic interaction. Excitons are of increased importance because of the relatively small dielectric constant in organic semiconductors.[9] As a result the Coulombic force binding the excitons is screened less, resulting in stronger bonds and excitons of higher energy. As a result of the increased binding energy the exciton state is more stable and has a longer lifetime.

Excitons have a lifetime τ after which they dissociate into separate charge-carriers. During this lifetime the excitons can migrate distances l through the medium. Dissociation of excitons primarily occurs at the surfaces of the semiconducting medium[51]. However, excitons also dissociate when either the charge-carrier or hole recombines. When the charge-carrier recombines it breaks the bound exciton state, freeing the hole. The opposite is also possible for hole recombination. Recombination can occur if the energies of the charger-carriers and holes match. Usually traps, e.g. at surfaces and grain boundaries, provide a hole or charge-carrier for the free oppositely charged carrier to recombine with. Hence, when a bound charge-carrier or hole recombines automatically the exciton dissociates and the exciton's lifetime is ended.

Therefore the lifetime of excitons depends on the individual lifetimes of the carriers and holes before recombination. The following lifetimes are of importance for excitons and conductivity in general:

1. The carrier/hole lifetime $\tau_{\mathrm{n/p}}$ is the time between excitation and recombination of the carrier/hole. The lifetime is also ended when carriers or holes are extracted from the material without replenishment by an electric field between electrodes.
2. The exciton lifetime τ_{e} last from creation until dissociation, either at spontaneously or when the carrier or hole lifetime is terminated.
3. The free lifetime τ_{f} applies to charge-carrier, holes and excitons alike. It signifies the time during which they are not bound by traps and can freely migrate through the semiconductor contributing to the conductivity. It can maximally be as long as the (total) lifetimes $\tau_{\mathrm{n/p}}$ and τ_{e}, but is usually shorter due to trapping.

The addressed recombination and dissociation processes occur on a fast, nanosecond timescales, resulting in equivalent lifetimes.

Present research suggests another exciton transformation process into other excitonic species[38, 51, 76]. The mechanism for this transformation is still debated but the resulting species is a triplet state. Direct radiative transition between the triplet state is quantum mechanically forbidden. The triplet state has a longer, microsecond timescale, lifetime[51, 61]. An excellent, more extensive, treatise of singlet and triplet exciton dynamics in organic semiconductors is provided by Mikhnenko [49]

[11] This research will refrain from more specific exciton nomenclature such as Frenkel, Warnier or charge-transfer excitons used in other research. An excellent detailed treatise of different excitons can be found in Schwoerer and Wolf [61].

2.1.5 Materials

The molecular organic semiconductors of interest to this research are: rubrene ($C_{42}H_{28}$), TIPS pentacene ($C_{44}H_{54}Si_2$) and TIPG pentacene ($C_{44}H_{54}Ge_2$. Figure 2.2 shows how the molecules are composed of a backbone of benzene molecules in accordance with the molecular organic semiconductor treatise in section 2.1.1. Their side groups affect their specific characteristics that are addressed in the following.

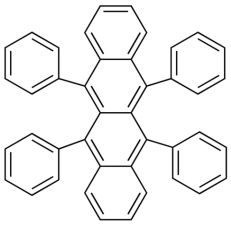

2.2 (A) Schematic Kekulé structure of rubrene. The backbone is tetracene and with benzene side group the molecules becomes rubrene. *Image from* Sigma-Aldrich [67].

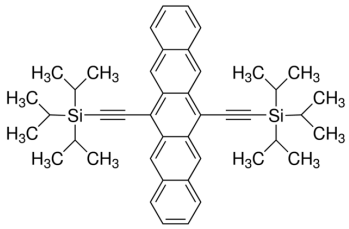

2.2 (B) Schematic Kekulé structure of TIPS pentacene. The backbone is pentacene and the two silicon side groups make it TIPS pentacene. *Image from* Sigma-Aldrich [67].

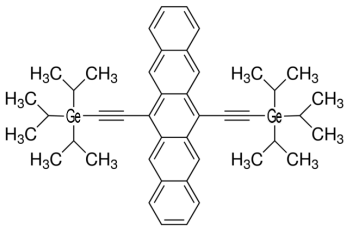

2.2 (C) Schematic Kekulé structure of TIPG pentacene. The backbone is pentacene equivalent to TIPS but with two germanium side groups. *Image altered from TIPS image from* Sigma-Aldrich [67].

2.1.5.1 Rubrene

Rubrene is a broadly studied, reddish coloured molecular organic semiconductor. It is a unipolar p-type[12] semiconductor with the chemical formula $C_{42}H_{28}$ and is also denoted as 5,6,11,12-tetraphenyltetracene[6, 7, 38, 43, 55, 78, 79]. It is wellknown for its record-high charge-carrier mobility of $40\,\mathrm{cm^2V^{-1}s^{-1}}$ and consequently a common benchmark material. It is a tetraphenyl derivative of tetracene that forms orthorhombic crystals[13]. Its unit cell distances are a=26.860(1) Å, b=7.1936(1) Å and c=14.433(1) Å[14]. Crystals can be grown with dimensions upto $10\,\mathrm{mm}$ using physical vapour deposition (PVT)[37].

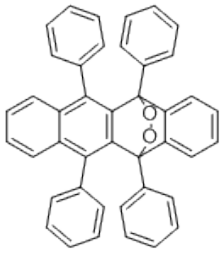

FIGURE 2.3: Rubrene endoperoxide is the primarily occuring oxidized form of rubrene. The oxidation breaks the benzene structure, affecting the conjugated bonds associated with electric properties.

Like all organics, rubrene crystals oxidize when exposed to light (see page 8). The primarily created oxidized form is called rubrene endoperoxide shown in fig. 2.3[75]. The figure shows how the oxidation brakes the benzene's conjugated bonds that provide the electronic states accessed by charge-carriers (section 2.1.2). Consequently oxidation affects conductive properties of rubrene.

Rubrene is not a soluble compound, making the fabrication of large area thin film difficult as common wet fabrication techniques are unusable. Nevertheless, polycrystalline films with thicknesses as thin as a several nanometers have been achieved. Rubrene thin films have been reported to perform with a charge mobility of $5\,\mathrm{cm^2V^{-1}s^{-1}}$ whilst stressed by mechanically bending the film upto a $6\,\mathrm{mm}$ curvature[8].

[12] P-type semiconductors are semiconductors in which the mobility of positively charge holes dictate the semiconducting behavior. The opposite holds for n-type semiconductors.

[13] It can also form monoclinic and triclinic crystals, but the orthorhombic form has the best properties in terms of conductivity[14].

2.1.5.2 TIPS Pentacene

TIPS pentacene (TIPS) is a novel chemical variation on the well documented pentacene. Its chemical formula is $C_{44}H_{54}Si_2$ and full chemical name is 6,13-Bis (triisopropylsilylethynyl) pentacene[39, 53]. TIPS has the same backbone structure made of 5 benzene molecules as pentacene. Regular pentacene, $C_{22}H_{14}$, commonly found as a purple powder, is amongst the longest studied molecular organic semiconductors. Its planar structure consists of 5 linearly bound benzene rings. Pentacene also displays high $30\,\mathrm{cm^2V^{-1}s^{-1}}$ carrier mobility in its single crystalline form[20, 72]. In films mobilities were achieved upto $1\,\mathrm{cm^2V^{-1}s^{-1}}$[40].

In the TIPS molecule triisopropylsilylethynyl-groups are bound to carbon (C) atoms 6 and 13 in the carbon backbone[5]. The π bonding in the benzene structure largely defines the electric properties for regular pentacene and should remain largely unaffected in TIPS. Therefore regular pentacene provides a logical and excellent framework for investigating TIPS.

The most important difference to regular pentacene is that TIPS is soluble, greatly increasing its applicability. For TIPS wet fabrication techniques are possible such as drop-casting and inkjet-printing. Drop-casted TIPS films have been fabricated with high mobility values up to $11\,\mathrm{cm^2V^{-1}s^{-1}}$[15].

Another difference is the crystalline packing. Regular pentacene crystallizes in an edge-to-face fashion commonly referred to as herringbone packing, see fig. 2.4a. Due to the triisopropylsilylethynyl-groups TIPS crystals form face-to-face oriented molecular structures that look like brick walls shown in fig. 2.4b. The brick-wall packing in TIPS improves p orbital overlap, potentially improving conductive properties of the material.

2.4 (A) The Herringbone packing causes inferior carrier mobility.

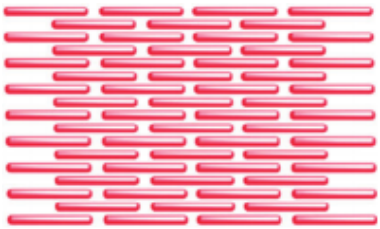

2.4 (B) The brickwall packing provides superior carrier mobility due to better overlap between adjacten molecules.

2.1.5.3 TIPG Pentacene

TIPG pentacene (TIPG) is a similar variation to pentacene like TIPS. It has only recently been synthesized at the University of Kentucky and at the time of this research there is no knowledge of any scientific publications on TIPG. The difference with TIPS is the substitution of germanium (Ge) for the Si in TIPS. The chemical formula is $C_{44}H_{54}Ge_2$. The intention of the Ge substitution is that the high atomic Z number of Ge increases the stopping power of TIPG for ionizing radiation. Theoretically it would provide superior X-ray detector performance. At the time of this research charge-carrier mobility and X-ray response are still under study.

2.1.6 Photocurrent Spectroscopy

Photocurrent (PC) spectroscopy provides a nondestructive technique to characterize optoelectronic properties of semiconductors. The optoelectronic phenomenon of photoconductivity is the increase of electrical conductivity as result of incident electromagnetic radiation. The incident radiation excites bound charge-carriers in the semiconductor after which they contribute to its conductivity.

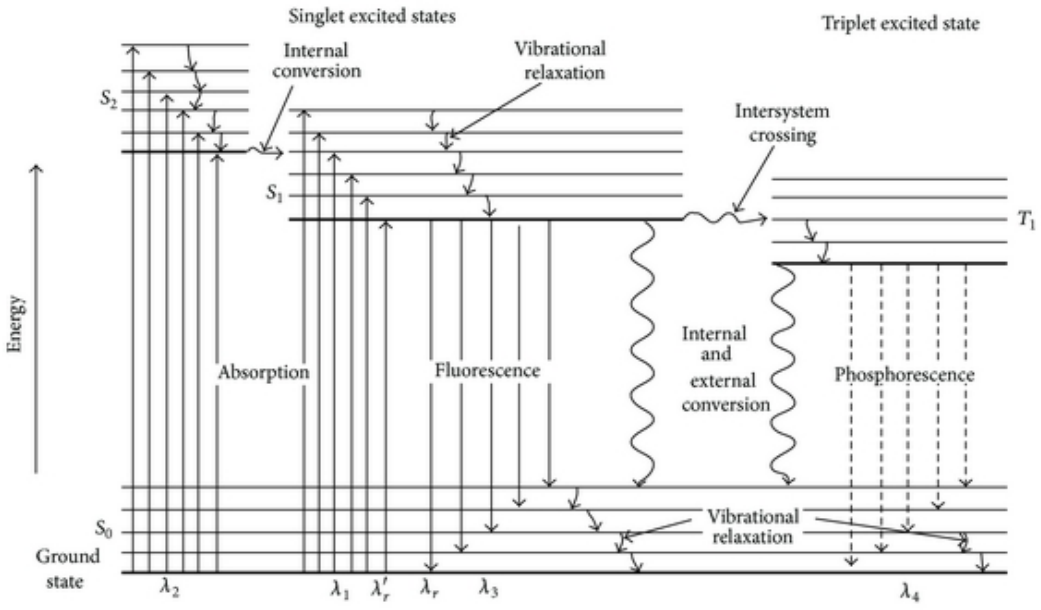

FIGURE 2.5: Jablonski diagram of electronic transitions commonly found for organic semiconductors. Straight upward arrows correspond to absorbed wavelengths and downward solid arrows to fluoresence- and dashed indicate phosphorescence wavelengths. Curved arrows correspond to vibronic and other non-radiative transitions. The S and T levels respectivetly represent singlet and triplet states. Wavelengths shorter than λ_r carry enough energy to bridge the energy gap[21].

The energy diagram shown in fig. 2.5 illustrates electronic transitions commonly found for photoconductors[14]. Charge-carriers are excited from the S_0 ground state in the VB to excited S_1 and S_2 singlet states in the CB. Only absorbed wavelengths shorter than λ_r radiate enough energy to bridge the energy gap. Shorter λ_1 wavelengths excite carriers to higher energy states within the degenerate excited state. Within the CB the excited carrier can relax to lower energy levels through fast vibrational transitions. It follows that the absorption of the radiation is key to PC spectroscopy. In fact, the PC is proportional to the absorption coefficient α, $I_{PC} \propto \alpha$ for wavelengths with energies close to the bandgap[25]. Shorter wavelengths (λ_2) excite carriers to a different, higher energy S_2 singlet states. Non-radiative conversion is possible from the singlet S_2 to S_1 states.

The photo-generated charge-carriers in the excited $S_{1,2}$ states, the created HOMO holes and the combined excitons can travel through the medium. During their lifetime τ they can get trapped or recombine with energy levels associated with traps (see section 2.1.4.1). Excitons can also recombine when the photo-generated $S_{1,2}$ free charge-carriers relax back to the HOMO

[14] A material, typically a semiconductor, that becomes conducting as a result of photo-absorption.

through fluorescence as seen in fig. 2.5. During their lifetime freely migrating charge-carriers add to the conductivity. From eq. 2.2, multiplied with the associated lifetimes τ, the conductivity increases with the increase in available, free charge-carriers and oppositely charged holes $\Delta\sigma = e(\Delta n\mu_n\tau_n + \Delta p\mu_p\tau_p)$. The positive and negative carriers' lifetime is expressed by $\tau_{p/n}$

$$J = (\sigma + \Delta\sigma)E = J_{dark} + J_{PC} \tag{2.3}$$

The increased conductivity is measured as an increase in the current. Equation 2.3 shows how $\Delta\sigma$ multiplied by the applied electrical field E contributes to a rise J_{PC} on top of the J_{dark} current density that is measured without exposure to radiation.

2.1.6.1 Photoconductivity Phenomena

Usually a PC response can be expected to be roughly linear and symbatic to the absorbed photon flux, as illustrated in the previous section. However, recent studies indicate the possibility of more complicated mechanisms influencing the measured photocurrent. These may cause a nonlinear photocurrent response[38, 51] or even complete antibatic[28, 52] PC dependencies to the absorbed radiation.

Triplet States
In section 2.1.4.2 is treated how excitons, when they dissociate in separate charge-carriers, can be collected through electrodes with an applied E-field. But there is also the possibility that excitons might convert into other excitonic species with different lifetimes. Irkhin, Najafov, and Podzorov [38] showed that:

> rubrene exhibits several distinct regimes, in which photocurrent as a function of continuous wave excitation intensity is described by a power law with exponents sequentially taking values 1, $1/3$ and $1/4$.

On the right side of fig. 2.5 is shown how S_1 singlet exciton states can cross to T_1 triplet states. The nonlinear PC response may be attributed to these T_1 triplet states. The triplet states have significantly longer lifetimes and recombination can only occur through slow phosphorescence transition. Without dissociation into separate charge-carriers and holes there is no contribution to the measured PC. The formation of triplet states is less likely to occur than regular excitons. When the absorption of photons is small, the effect of this higher order process very small. For high intensity incident light the number of absorbed photons increases and consequently the impact of triplet state formation. The creation of triplets through singlet fusion might explain explain a nonlinear photocurrent response resulting in a suppressed current for increased intensities.

Antibatic Photocurrent-Absorption Correlation
Traps and specific oxidation are well-known phenomena that impact especially organic semiconductors. The general influence of traps on the available electronic transitions has been treated in section 2.1.4.1. However, recently a more drastic change of the PC in rubrene crystals resulting in an antibatic response has been specifically attributed to oxidation[52]. Instead of the common symbatic PC behavior relative to the absorption spectrum an antibatic response has been seen.

Another possible explanation of the symbatic-antibatic PC transition in pentacene films has been proposed by Gorgolis et al. [28]. A model of the interface between different crystalline phases in the film reproduces the antibatic response. The interface at a certain depth from the surface may affect excitons that are diffused onto that interface. Their resulting dissociation may cause an antibatic response. Gorgolis et al. [28] conclude that:

> the experimental data and the symbatic to antibatic transition depend not only on the film thickness but also on the absolute magnitude of the optical absorption and the diffusion length of the light created species.

2.2 Optics

In the following section a treatise is provided on the theory concerning the optics employed throughout this research.

2.2.1 Spectroscopy

Spectroscopy is a broadly used term referring to experimental techniques that employ the spectrum of electromagnetic waves. Literally meaning image viewing, these techniques 'view' a measured quantity as a function of wavelength. The resolution of the following 'image' depends on the precision with which the individual wavelengths in the spectrum can be separated. A spectrum, covering a broad band of wavelengths, can be spatially separated into narrow bands of light with specific wavelengths by means of diffraction.

2.2.1.1 Diffraction Gratings

A monochromator takes as input a broadband, polychromatic light spectrum and puts out a narrowband, ideally monochromatic, light signal. The diffraction of light lies at the center of the monochromator's workings. The light is diffracted of a grating, described by the diffraction equation 2.4

$$\sin(\alpha) + \sin(\beta) = k\lambda n \tag{2.4}$$

in which α and β denote the angles[15] of the respectively incident and diffracted light, k the diffraction order, λ the wavelength in nm and n the groove density of the grating in mm^{-1}.

In the case of a specific geometry, known as the Czerny-Turner configuration illustrated in fig. 2.6, the light path and the difference between α and β is constant; the grating being the rotating element[50]. Substituting $\alpha \to \theta + \theta_o + \phi$ and $\beta \to \theta + \theta_o - \phi$ in the diffraction equation 2.4 and applying the trigonometric identity $\sin(x) + \sin(y) = 2\cos(\frac{x-y}{2})\sin(\frac{x+y}{2})$ gives eq. 2.5 in terms of the angle of the grating normal with respect to the device axis.

$$2\cos(\phi)\sin(\theta + \theta_o) = k\lambda n \tag{2.5}$$

Equation 2.5 offers variables that better represent the situation where the constant ϕ is the fixed angle between the incident and diffracted beam, θ is the angle between the grating normal and the central monochromator axis and θ_o a constant offset due to any asymmetrical geometry.

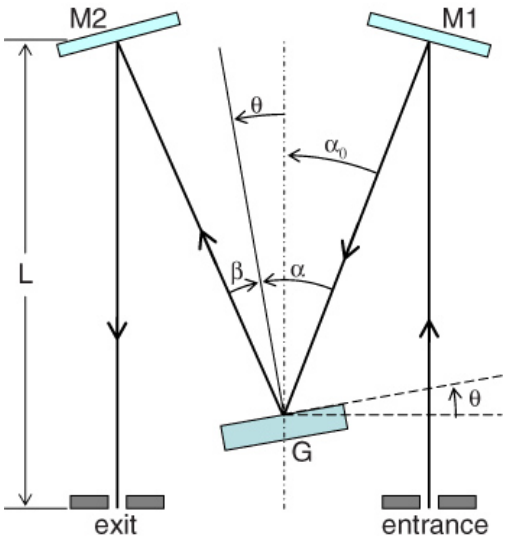

FIGURE 2.6: Schematic symmetric Czerny-Turner configuration with fixed mirrors $M_{1,2}$ and rotating grating G. Light is incident on G at an angleα and diffracted with an angle β. The beampath is fixed with respect to the device axis, α_0 is fixed. Consequently $\alpha + \beta$ is fixed for the wavelength that is collected by M_2. Therefore θ sets the diffracted wavelength that is collected. Due to the symmetry in this configuration, the grating angle offset $\theta_o = 0$. Image from Yun, You, and Bellan [83].

[15] Note that β and α are opposite sign relative to the grating normal.

Blaze

Blazed gratings are modified so that near a chosen blaze wavelength they have increased diffraction efficiency, expressed as the diffracted light intensity relative to stray-light. Blazing is done by cutting the grooves on the grating at a specific angle. Consequently, a ruled[16] grating has an efficiency curve with a spectral dependency. The efficiency drops for wavelengths, i.e. diffraction angles, diverging from the blazed wavelength because of the groove angle.

The rule of thumb for grating choice is using the grating with the highest groove density for the highest resolution. However, high groove density restricts the spectral range for which the grating provides efficient diffraction. This range can roughly be estimated using the "2/3 - 3/2" rule[62].

$$\frac{2}{3}\lambda_b > \lambda < \frac{3}{2}\lambda_b \tag{2.6}$$

Equation 2.6 states that the diffraction is efficient for wavelengths within the range of $^2/_3$ upto $^3/_2$ times the blaze wavelength λ_b. Shorter wavelengths will drop of drastically in intensity. The intensity drops slower for wavelength longer than $^3/_2\lambda_b$. However, s and p polarized light have different cutoff wavelengths resulting in exit radiation with a strong polarization[62].

Dispersion

The monochromator's effectiveness in spatially separating different wavelengths are expressed by the angular and linear dispersion due to its grating. Solving eq. 2.5 for $\theta(\lambda)$ and differentiating with respect to λ yields the angular dispersion $\frac{\partial\theta(\lambda)}{\partial\lambda}$. The reciprocal linear dispersion[17] D is the inverse of the angular dispersion and output focal length product $(L\frac{\partial\theta(\lambda)}{\partial\lambda})^{-1}$, as described by eq. 2.9:

$$\theta(\lambda) = \arcsin(\frac{k\lambda n \sec(\phi)}{2}) - \theta_o \tag{2.7}$$

$$\frac{\partial\theta(\lambda)}{\partial\lambda} = \frac{kn\sec(\phi)}{2}\sec(\theta(\lambda)+\theta_o) \tag{2.8}$$

$$D = \frac{2\cos(\phi)}{Lkn}\cos(\theta(\lambda)+\theta_o) \tag{2.9}$$

In eqs. 2.7 to 2.9 $\theta(\lambda)$ is the angle between the grating normal and monochromator axis, $\frac{\partial\theta(\lambda)}{\partial\lambda}$ the angular dispersion in nm^{-1}, D the reciprocal linear dispersion in $\mathrm{nm\,mm}^{-1}$, k the diffraction order, λ the wavelength in nm, n the grating's groove density in mm^{-1}, ϕ the constant half angle between the incident and diffracted ray, θ_o the grating angle offset and L the output focal length in mm (see fig. 2.6).

2.2.1.2 Resolution

Spectral resolution concerns the separability of spectral lines. An instruments resolution is its precision upto which it can resolve one spectral line from another as defined by the Rayleigh criterion[18]. The resolution of the monochromator is set by the largest slit width:

$$\Delta\lambda = w\,D \tag{2.10}$$

with the slit width w in mm and the reciprocal linear dispersion D from eq. 2.9.

[16] There are several techniques to blaze gratings with their respective pros and cons. The most common are ruled, ion-etched or blazed holographic gratings. These have sharp edged gratings in contrast to standard holographic gratings that typically have a sinusoidal grating profile and to which this theory does not apply.

[17] It is custom to express the linear dispersion in reciprocal distance. It quantifies the bandwidth per millimeter distance along the image plane.

[18] Two spectral lines are resolved if the first order diffraction minimum of the first wavelength coincides spatially with the first order diffraction maximum of the second wavelength.

Resolving Power
The instrument's resolving power is a commonly used figure of merit. It refers to an instrument's ability to distinguish between two spectral lines of different wavelengths. Resolving power is defined as $R = {}^{\lambda}/_{\Delta\lambda}$, the division of a wavelength by the resolution $\Delta\lambda$ between two consecutive wavelengths.

Instrumental Bandpass
The observed resolution depends on all instruments in the optical path. As the optical signal passes through the instruments, the signal is affected according to the transmission function of those instruments. The instrument's transmission of the signal often has a spectral dependency. For a continuous source the spectral bandwidth that is isolated by the instrument and passed through is the bandpass. For monochromatic sources the transmitted signal in practice gets smeared, effectively broadening the original signal. The resulting bandwidth is known as the instrumental line profile or instrumental bandpass. Ultimately, the recorded spectrum is the convolution product of the source spectrum, the instruments' spectral transmission functions and the detector spectral responsivity: $f(\lambda) = f^s(\lambda) * f^d(\lambda) * f_1^{inst}(\lambda) * f_2^{inst}(\lambda) * f_3^{inst}(\lambda) * \ldots$[19]

Instead of determining each instrument's transmission function, a simpler approach is taking into account each instrument's individual bandpass. The combined smearing results in a net bandpass given by eq. 2.11. Finally, the net bandpass restricts the achievable spectral resolution with the setup.

$$BP_{net} = \sqrt{BP_1^2 + BP_2^2 + \ldots} \tag{2.11}$$

The resolution of the setup can also be established experimentally. A precisely known monochromatic input source - for example an atomic emission line - results in broadened measured spectrum signal. Then the full width at half maximum (FWHM) of the recorded peak is the bandpass of the setup and the resolution for the experimental configuration[42].

2.2.2 Optical Throughput

The ability of an optical signal to pass through an experimental setup depends on the geometrical matching of the involved instruments. Several approaches exist to this optimization problem. The most common of these is simply matching the F-numbers, ${}^{F}/_{\#} = \frac{1}{2\tan(\theta_{1/2})} \approx \frac{f}{D}$, or numerical apertures (NAs), $\mathrm{NA} = n\sin(\theta_{1/2}) \approx \frac{1}{2^{F}/_{\#}}$, of all devices in the optical path. However, this procedure is insufficient[19] for proper optimization of the troughput and a more extensive method is wanted based on the concept etendue[20].

The setup's throughput depends on the etendue of each optical component. The instrument with the lowest etendue limits the photon flux through the total system. It is defined in eq. 2.12 as the area A of a source or detector multiplied by its associated solid angle Ω and the refractive index n squared[19]. Subsequently G has units of area and denotes the projected extent corresponding to an area and solid angle. In the case of a detector behind an aperture, the etendue relates to the acceptance cone, projected outward from the detector's active surface through the aperture[26, 44].

$$\boldsymbol{dG} = n^2 \boldsymbol{dA} \cdot \boldsymbol{d\Omega} \tag{2.12}$$

[19] It is based on the assumption of a point-like focus and therefore does not take into account the area of the source, detector or slit. In fact, the concepts of F-numbers and NA are 1 dimensional simplifications of the more generalized concept etendue

[20] Etendue is also often called the geometrical extent, acceptance, collecting power or simply throughput.

In spherical coordinates the infinitesimal solid angle is $d\Omega = \sin\theta d\theta d\phi$. Substituting this in eq. 2.12 and integrating for a cone results in a solid angle of $2\pi(1 - \cos(\theta_{1/2})$, with $\theta_{1/2}$ being the 1-dimensional half-angle of the cone's opening angle, and is equal to the area of a spherical cap.

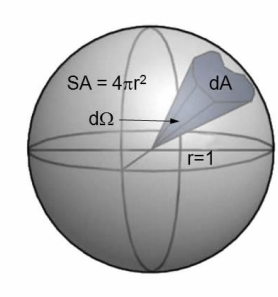

FIGURE 2.7: The projected solid angle on a sphere.

2.2.2.1 Magnification

The combination of lenses with different foci results in (de)magnification of the created image with respect to the original object. The magnification depends on the focusing power of the lenses. Equation 2.13 expresses the magnification M in terms of various connected parameters: object and image surface areas S_O and S_I, object and image separation to the lens q and p, solid angles Ω, NA and F-numbers ${}^{F}/_{\#}$[42].

$$M = \sqrt{\frac{S_O}{S_I}} = \frac{q}{p} = \frac{\sin(\Omega_O)}{\sin(\Omega_I)} = \frac{\mathrm{NA}_{in}}{\mathrm{NA}_{out}} = \frac{{}^{F}/_{\#_{in}}}{{}^{F}/_{\#_{out}}} \tag{2.13}$$

The magnification of the source throughout the optical setup is of importance. As as result of magnification the created image will be large or smaller but the total flux is unaffected. The flux density, however, is.

2.2.3 Detectors

During this research two different detectors have been used for measurement of light flux: a photodiode and a pyroelectric detector. Their application is the same, converting an optical signal into an electrical one, but their principles of operation are different. Below the principle properties fore any radiation detector are listed: the responsivity (eq. 2.14) represents the ratio between the output signal S in V and the incident photon flux Φ in W. The noise equivalent power (NEP) (eq. 2.15) is a measure for the sensitivity of the detector. The NEP is the maximum incident power on the detector that is still equaled by the noise. It depends on the photon flux Φ in W, the signal S in V, the noise N in $\mathrm{V}/\sqrt{\mathrm{Hz}}$ and the detector bandwidth Δf in Hz. Finally, the detectivity (eq. 2.16) is common property to compare different detectors as it is a measure a detector's performance independent of it's active area A.

$$R = \frac{S}{\Phi} \tag{2.14}$$

$$NEP = \frac{\Phi}{{}^{S}/_{N}\sqrt{\Delta f}} \tag{2.15}$$

$$D^* = \frac{{}^{S}/_{N}\sqrt{\Delta f}}{E_e\sqrt{A}} = \frac{\sqrt{A}}{NEP} \tag{2.16}$$

2.2.3.1 Photodiode

The photodiode (PD) mechanism of operation depends on the absorption of light characteristic to the detector material. A common material for photodiodes is Si. The silicon material is doped to create a relatively positively- and a negatively charged region. As a result a p-n junction form with a depletion region in between as shown in fig. 2.8a. In general, any incident light that is absorbed excites electrons in the semiconductor from the VB to the CB. The electrons leave holes in the VB band, creating electron-hole pairs that will eventually recombine. However, holes and electron created in the depletion region will be spatially separated due to the bias,

preventing recombination. Consequently the electrons can flow through the N-doped region of the semiconductor towards the electrodes. The opposite holds for holes in the P-doped region. Subsequently the electrons and holes are collected at the electrodes and contribute to the detected electrical signal. Additionally an external bias may be applied between the two connected electrodes through the material. The bias direction affects the efficiency of electrons and holes conversion into a measured electric signal.

In the case of a forward bias $-\mathcal{E}_{ext}$, the photovoltaic mode of operation, the depletion region width is decreased by the externally applied bias. In the case of a reverse bias $+\mathcal{E}ext$ the method of operation is called photoconductive. The depletion region's width is increased. The latter method yields lower capacitance, a faster response speed and improved linearity. The downside is increased dark current that linearly increases with the applied bias and obscures the measured signal.

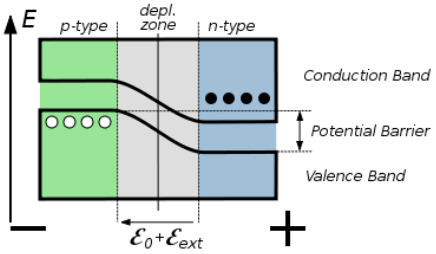

2.8 (A) The p-n junction in a photodiode shows the differently doped regions with holes (white) and electrons (black) and the depletion zone in between. As a result of the doping, there is a natural bias $\mathcal{E}_0$ and an external bias $\mathcal{E}_{ext}$ can be forwardly or backwardly applied depending on the sign.

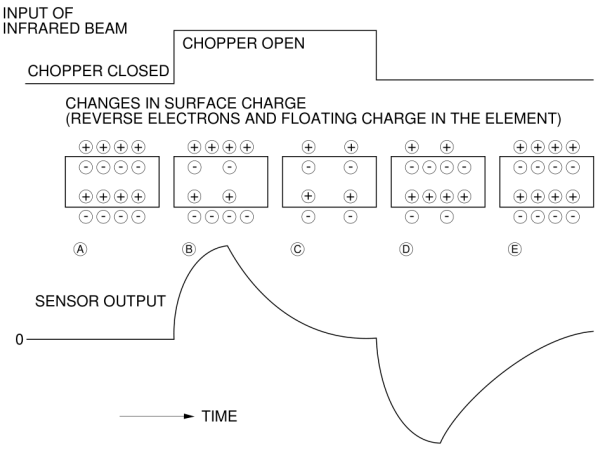

2.8 (B) Mode of operation of a pyroelectric detector in consecutive stages A to E. The top line shows the optical input signal, below the polarization of the pyroelectric material is illustrated and at the bottom the resulting sensor output signal.

2.2.3.2 Pyroelectric

A pyroelectric detector (PED) has no spectral dependence because its operation stems from the pyroelectric property of the detector material. Pyroelectricity entails the change of the material's polarity due to changes in temperature. Due to the thermal origin of the change in electric polarity, a pyroelectric detector has no spectral dependence.

Lead zirconate titanate (PZT) is a electroceramic material with pyroelectric properties that has the chemical formulation $PbZr_xTi_{1-x}O_3$. For temperatures below the material specific Curie temperature the ions in the pyrolectric crystallize in such a manner resulting in a spontaneous net charge potential between the material's opposing sides[45]. The charge difference is compensated by ions in the surrounding air. This is illustrated at step A in fig. 2.8b.

When the PZT is exposed to radiation, the portion that is absorbed heats the material, causing a change in the polarization. The result is a measurable change in voltage over the material (step B). Subsequently the PZT finds a new neutral equilibrium for the current polarization state, neutralizing the earlier potential as shown in step C. It follows modulation of the incident light is required continuous detection with a PED. This is illustrated in step D and E where the previously incident light is blocked by a chopper, the polarization returns to the initial stage (D) and finally is neutralized by nearby ions in the air (E)[12].

2.3 Lock-in Amplification

A lock-in amplifier allows the detection of a small signal obscured by a noise background with up to a million times larger amplitude. It resolves the signal from the noise through an advised scheme of amplification and filtering of the raw input. In order to, preferably, amplify only the signal and filter out only the noise, a lock-in amplifier uses phase-sensitive detection combined with low-pass filters.

2.3.1 Phase-Sensitive Detection

The central component of a lock-in amplifier is a phase-sensitive detector (PSD) that provides detection of a signal based on its frequency. Intuitively a PSD measurement can be imagined by considering an experiment aiming to detect the light of a single lamp in a room filled with various other lights. If one were to repeatedly switch on and off the lamp its contribution to the total detected light would 'flicker' with the same frequency. Then for a 'flickering', or modulation, frequency known beforehand it is not hard to imagine that it is possible to detect the light of a single lamp in a room filled with lamps. A lock-in amplifier operates in a similar way on a modulated signal with a specific reference frequency ω_r.

The PSD takes two inputs; the total input that contains noise and the modulated signal $V_{sig}\sin(\omega_r t + \theta_{sig})$ and a reference signal with the same frequence as the signal modulation $V_r \sin(\omega_r t + \theta_{ref})$, in which θ_{sig} and θ_{ref} are offset-phases due to any delay between signal and modulation. The PSD then effectively multiplies the input and reference signals.

$$\begin{aligned} V_{PSD} &= V_{sig}\sin(\omega_r t + \theta_{sig}) V_r \sin(\omega_r t + \theta_{ref}) \\ &= \frac{1}{2} V_{sig} V_r \cos([\omega_r - \omega_r]t + \theta_{sig} - \theta_{ref}) - \frac{1}{2} V_{sig} V_r \cos([\omega_r + \omega_r]t + \theta_{sig} + \theta_{ref}) \\ &= \frac{1}{2} V_{sig} V_r \cos(\theta_{sig} - \theta_{ref}) - \frac{1}{2} V_{sig} V_r \cos(2\omega_{ref} t + \theta_{sig} + \theta_{ref}) \end{aligned} \tag{2.17}$$

Equation 2.17 shows that the subsequent PSD output contains different components. For equal signal and reference frequencies the difference-term become a default current (DC) voltage, whereas the other terms have a frequency dependence, i.e. alternating current (AC) signals. Any noise at frequencies different than the reference frequency ω_{ref} end up with a frequency dependence in the PSD output. At this point the original raw AC signal with noise is split into a DC component that contains the signal and is, in theory, clearly distinguishable from the AC components that contain the noise and higher orders of the signal.

2.3.2 Low-Pass Filters

As their name suggests, low-pass (LP) filters are used to attenuate high frequency signal and pass through low frequency and DC signals. Applied to the PSD output the AC components $\frac{1}{2} V_{sig} V_r \cos(2\omega_r t + \theta_{sig} + \theta_{ref})$ will be filtered, leaving the DC term $\frac{1}{2} V_{sig} V_r \cos(\theta_{sig} - \theta_{ref})$.

2.3.3 Two-phase Detection

It is possible to obtain V_{sig} without the phase dependence by using two-phase detection. Combining the first PSD above with a second PSD in parallel that however operates on the orthogonal, $\frac{\pi}{2}$ phase shifted, signal $V_{sig}\sin(\omega_r t + \theta_{sig} + \frac{\pi}{2})$ leads to a $V_{PSD_2} = \frac{1}{2} V_{sig} V_r \sin(\theta_{sig} - \theta_{ref})$. Now the final magnitude R of the signal vector can be computed from $V_R = V_{PSD_1} + iV_{PSD_2}$

Note that it is the root-mean-squared (RMS) value of original signal that is detected.

Chapter 3

Methodology

This chapter provides a first section with the description of the experimental setup and how it is applied during the measurement. The second section focuses on the investigated samples. The samples are stimulated with an optical signal that induces charges within the material which are detected as an electric signal. To clearly distinguish them the optical signal shall hereafter be referred to as 'stimulus' and 'signal' shall pertain to the actually measured electrical signal.

3.1 Experimental Setup

The experimental setup can be subdivided into three parts consisting of firstly the stimulus source, secondly the stimulus control and finally the signal detection. The first part collects the full output from a spectral source. In the second part a controlled and spectrally resolved optical stimulus is selected from the broad spectrum output of the source. In the final stage of the setup the optical stimulus is collimated onto the sample and finally the resulting electrical response of the material is measured.

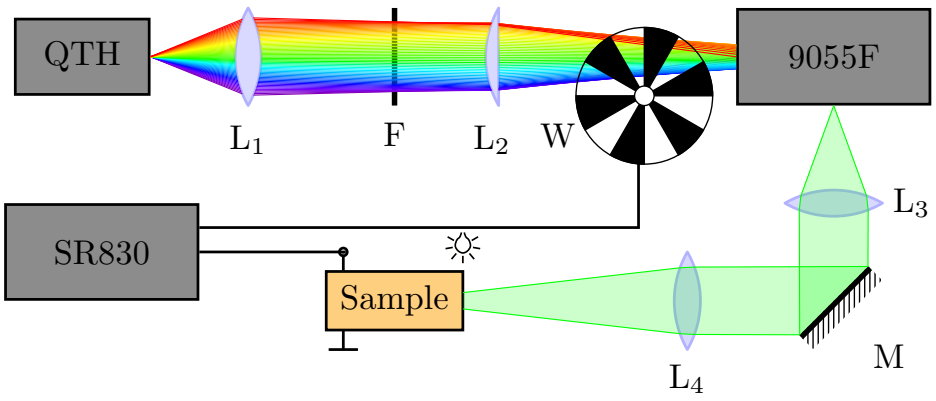

FIGURE 3.1: Schematic overview of the experimental setup. Light from a QTH lamp passes through a monochromator (9055F) lenses L_1 to L_4, a filter F, a chopperwheel W and via a mirror M and finally focussed onto the sample. The sample's electrical response signal and the rotating frequency of chopperwheel W are recorded by a lock-in amplifier (SR830). The light before the monochromator is polychromatic and monochromatic after.

3.1.1 Setup Part I: Spectral Source

A quartz tungsten halogen (QTH) lamp is used as optical spectrum source, whose output is collected through a series of optics and gets focused onto the entrance slit of the monochromator. The lamp is a standard $150\,\mathrm{W}$ QTH filament lamp manufacterd by OSRAM mounted in a Sciencetech lamp housing[32, 63]. The lamp housing redirects the light output into a primary condenser- and a secondary focussing lens system, as illustrated in fig. 3.2. These optics were calibrated to match the etendue of the lamp housing to that of the input slit on the monochromator using eq. 2.12. Matching the etendue ensures maximal light throughput. The system's etendue is limited by the slit widths at $G_{lim} = 277.659 \times 10^{-3}\,\mathrm{mm^2\,sr}$ for $50\,\mu\mathrm{m}$ slits. Appendix A contains a detailed treatise of etendue optimization. Between the two lenses the light is a collimated path beam into which optional optics can easily be added. Bandpass filters were inserted to exclude the second and higher order diffraction of shorter wavelengths than the filter window.(see page 22)[1].

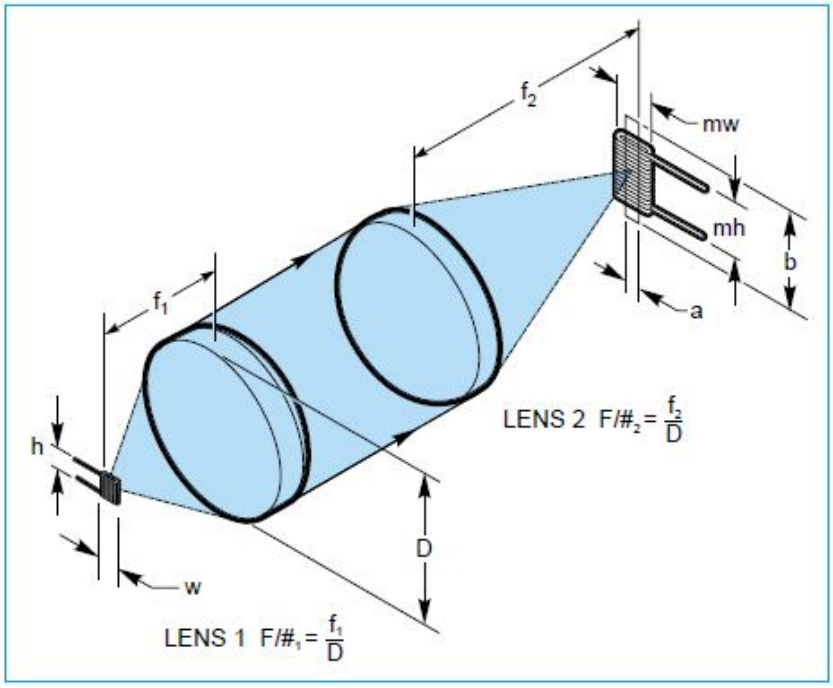

FIGURE 3.2: Condenser-focusing lens system. A condensing lens (LENS 1) matching to the geometry of the radiating source collimates the light. A secondary lens focuses the light according to the acceptance geometry of the device that is illuminated. *Image from AzoOptics [4].*

3.1.2 Setup Part II: Signal Control

The final optical stimulus is controlled by passing the full source output successively through an optical chopperwheel and a monochromator. The chopperwheel temporally modulates the stimulus. This fixes the necessary stimulus carrierwave frequency for later signal measurement. The broadband modulated stimulus enters the input slit of a monochromator, which selects a narrowband modulated stimulus from the input.

3.1.2.1 Monochromator

A monochromator is used to select narrowband optical signal from the broadband spectral source. The 9055F model made by Sciencetech is a Czerny-Turner monochromator with two slots for diffraction gratings and the ability to select between two different output ports[62, 64, 65]. Furthermore it contains three fixed mirrors that, respectively, collimate the incoming

light onto the grating, collect the light that is diffracted of the grating and lastly a flip mirror that optionally deflects the beam toward the side output slit. The gratings are mounted on a rotating turret driven by a USB stepper motor. Consequently the wavelength of the diffraction peak collected by the mirrors depends on the motor position. Rotating the grating turret changes the diffracted light according to eq. 2.5. Calibration of the monochromator is possible by altering the phase angle offset of the rotating grating turret. Its position is accurate up to $0.2\,\mathrm{nm}$ and reproducible up to $0.03\,\mathrm{nm}$.

The 9055F model is an asymmetric monochromator, since the instrument's main axis is no symmetry axis, due to the difference in distances and focal lengths of the mirrors ($200\,\mathrm{mm}$ and $250\,\mathrm{mm}$). The ratio between these lengths causes a magnification M$=1.25$ of the input slit projected onto the output slit. Likewise the monochromator has different F-numbers for the input and output slits altough literature states 2.5 for both apertures[65]. More accurate values were calculated from **??** for the specific slit widths used: ${}^{F}/_{\#_{in}} = 2.7$ and ${}^{F}/_{\#_{out}} = 3.3$. Finally, the input and output ports are fitted with slits bilaterally adjustable from $10.0(5)\,\mu\mathrm{m}$ to $6.0(0)\,\mathrm{mm}$ in width and have a fixed $10\,\mathrm{mm}$ height.

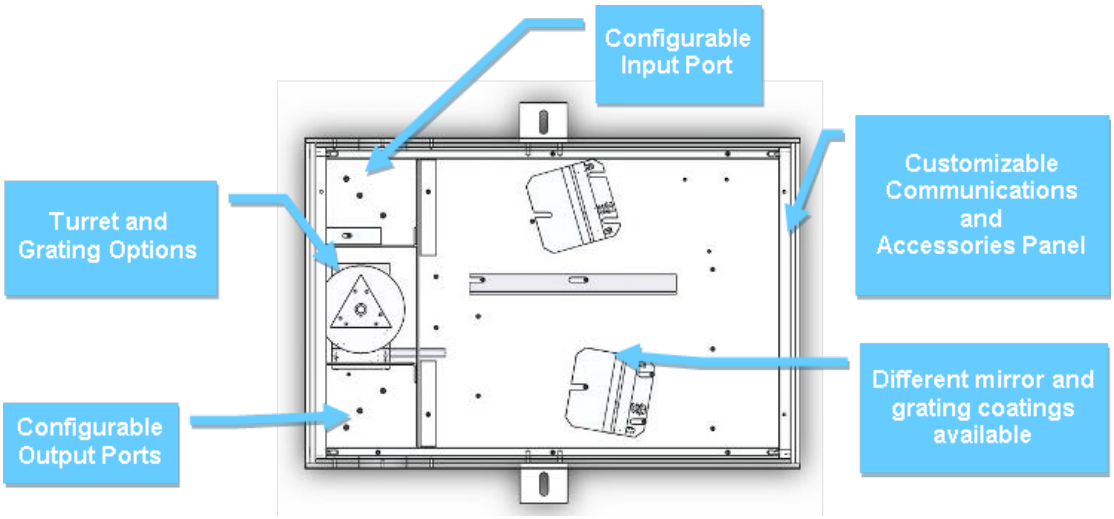

FIGURE 3.3: Internal Czerny-Turner geometry of the Sciencetech 9055F monochromator. Both mirrors are fixed whilst the rotating grating turrent enables changing the diffraction angle. The mirrors are distanced are unequeal length from the grating resulting in a magnification of the input. *Image from* Sciencetech Monochromators & Spectrographs Brochure *[64]*.

Grating

Two $1200\,\mathrm{gr/mm}$ groove density gratings with blaze wavelengths of $300\,\mathrm{nm}$ and $1000\,\mathrm{nm}$ were mounted on the grating turret. Their reported reciprocal linear dispersion is $3.3\,\mathrm{nm\,mm^{-1}}$ which sets the theoretical bandwidth limit at $0.033\,\mathrm{nm}$ for $10\,\mu\mathrm{m}$ slits[62].

The total spectral range of operation roughly spans from $100\,\mathrm{nm}$ to $1500\,\mathrm{nm}$. When scanning through the spectrum, the grating is changed at $700\,\mathrm{nm}$ for optimal diffraction efficiency. Second or higher order diffraction peaks of shorter wavelengths overlap spatially with first order peaks of longer wavelengths and would unintentionally end up in the measured spectrum (see eq. 2.4). To avoid this, a bandpass filter used that cuts out wavelengths shorter than $410\,\mathrm{nm}$.

3.1.3 Setup Part III: Signal Detection

The optical stimulus is focused onto the sample and the resulting electrical signal in the sample is measured with a lock-in amplifier. The sample stage consists of a metal box serving as Faraday cage to minimize noise from external electromagnetic radiation sources. The cage is grounded and contains an insulated BNC cable connector to connect the inner electronics to the lock-in amplifier. Figure 3.4 is a schematic overview of the electronics within the cage. The sample is connected to a low voltage DC bias. Ordinary AA batteries are used to avoid additional noise from the power lines. The circuit allows for both direct measurement of the photocurrent I_S and indirect measurement using a shunt resistance R over which the voltage V_R is measured. On page 27 the conditions are treated for either mode of measurement.

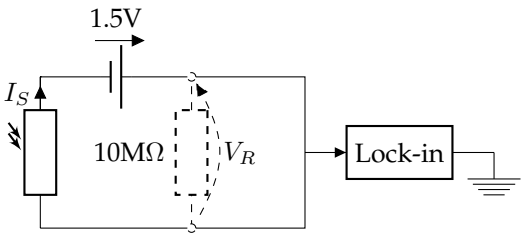

FIGURE 3.4: The electrical circuit connected to the sample consists of an in series connected 1.5 V DC battery and optionally 10MΩ resistance. The current I_S or voltage V_R, depending on the circuit, is measured by the lock-in amplifier.

3.1.3.1 Noise

This experiment's prevailing obstacle is the relatively poor signal to noise ratio. The following paragraph explains why the signal strength is limited and what kind of noise is present.

The signal is small because the optical stimulus is strongly restricted due to the typical experimental boundary conditions and sample intrinsic properties.

- The total emitted power is the integration over all emitted wavelengths. For each measurement only a narrow bandwidth is resolved by the monochromator and just that fraction of the total spectrum is used as optical stimulus.
- Only a part from the incident optical signal gets absorbed and converted into charge carriers resulting into a current.
- All the optical components in the light path decrease the final optical intensity, see appendix A.

Apart from these general restrictions for all types of measurements conducted with a similar setup, the organic samples investigated in this research present added constraints for a clear signal to noise ratio.

- The electrical bias can not be increased to increase the resulting electrical current without the risk of introducing a nonlinear E-field between the electrodes. Additionally a high bias causes sample-strain. Lastly, dependency between resistance, current and voltage in the samples is no longer Ohmic for large voltages.
- At high photon irradiance a nonlinear photocurrent response is seen.

Consequently the applied bias and incident photon irradiance are chosen to be low to avoid the effect of nonlinearity in the results. The downside is a decrease in the measurable signal.

The noise is large relative to the signal and has two components; intrinsic and external noise. The former of which largely consists of Johnson, Shot and 1/f noise.

- Johnson noise is random Gaussian noise due to thermal properties of charge-carriers related to the resistance of the medium[1]. It is of the form $V_{noise}(rms) = \sqrt{4kTR\Delta f}$ where k is the Boltzmann's constant, T the temperature in K, R the resistance in Ω and Δf the frequency bandwidth in Hz. Johnson noise is independent of the frequency, thus broadband.

[1] Johnson-, Nyquist- or Johnson-Nyquist noise is also called thermal noise or white noise.

- Shot noise is Poissonian noise that arises from the quantified charge-carriers in a current. It is of the form $I_{noise}(rms) = \sqrt{2qI\Delta f}$ where q is the electron charge in C, I the current in A (I is the RMS value in case of an AC current), and Δf the frequency bandwidth in Hz. Shot noise is also frequency independent.
- $1/f$ noise noise is omnipresent noise with an inverse proportionality to frequency.[2] that arises from the quantization of energy. Although its origin is debated in literature, its form is given by $S_{noise} \propto 1/f$ with S_{noise} some signal in arbitrary units and f the frequency of that signal. $1/f$ noise decreases with increased frequency, falling off 3dB per octave.

Added to the intrinsic noise, external noise sources might enter the experimental setup. It is important to distinguish between noise that is synchronous or asynchronous to the modulation frequency of the experiment as the former is of greater concern for the experiment (see section 3.1.3.2). Examples of synchronous noise sources are: ground loops, vibrational noise resulting in microphonics, capacitive coupling, inductive coupling and thermocouple effects. The *SR830 User's Manual* [69] provides excellent further information on how to reduced their impact by correct laboratory practice and experiment design.

All aforementioned noise sources are incoherent, meaning that they all add to the total noise as the square root of their summed squares. The resulting total noise is shown in fig. 3.5, which displays the internal noise in the measuring apparatus. In the total spectrum it is easy to distinguish the impact of specific noise components; the line frequency noise peaks, the $1/f$ noise dominating for low frequencies and a roughly constant noise amplitude due to Johnson noise for higher frequencies. From fig. 3.5 can also be deduced that certain frequencies contain less noise. Measuring the signal at those frequencies with a small frequency bandwidth with a lock-in amplifier would likely offer better results.

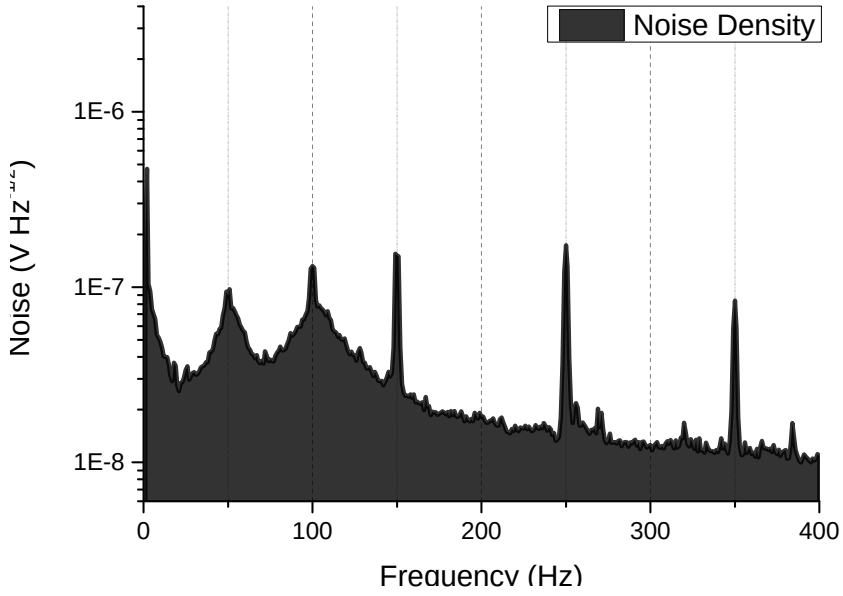

FIGURE 3.5: Internal noise density distribition over the frequency spectrum.

[2] Another name for $1/f$ noise is pink noise.

3.1.3.2 Lock-in Amplifier

In fig. 3.6 the functional block diagram is shown, corresponding to the Stanford Research-systems 830 lock-in amplifier (SR830) used in this research[69]. It schematically shows the process addressed in section 2.3 of how an input voltage or current combined with a reference passes through the electronics in order to resolve a clear signal from the input. Section 3.1.3.1 showed that background noise is an important challenge in this type of experiment. Hence an optimal configuration of the lock-in amplifier is key to this research to improve the ability to resolve the sought after signal. The following part presents a more specific treatise on operation of a lock-in amplifier and the various parameters' impact on the SR830's resolving potential[48].

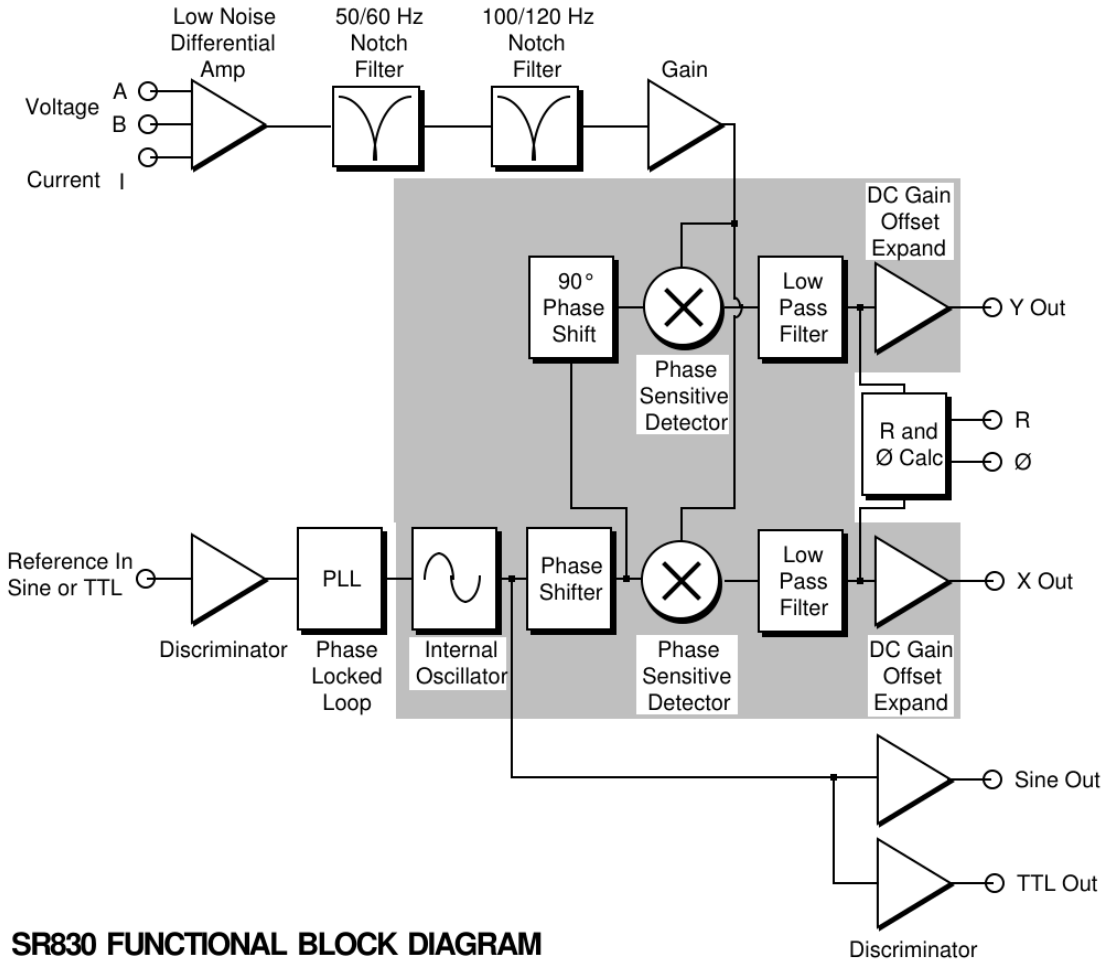

FIGURE 3.6: The functional block diagram of the SR830 Lock-in Amplifier. A schematic overview is provided of the two input signals that pass through the signal processing elements of the lock-in amplifier. The elements within the gray box denotes components in which the signal is digitally processed.

Reference frequency

The reference frequency matched to the signal modulation is required for phase-sensitive detection (see eq. 2.17). Moreover the modulation introduces a carrier-wave frequency that shifts the signal in frequency-space from DC to the modulation frequency. Section 3.1.3.1 showed that certain types of noise are frequency dependent. Therefore it is important to modulate the stimulus at such a frequency to shift it to a relatively noise-free frequency range. Typically higher frequencies contain less noise.

There is a trade-off to higher modulation frequencies in terms of signal amplitude due to response times associated with detectors and samples.

In practice most modulations of a stimulus are not sinusoidal with a clear frequency but signals with triangular or square form, like transistor-transistor logic (TTL) signals.

Using a phase-locked-loop (PLL) the lock-in amplifier 'locks' onto a reference frequency ω_r, setting its internal oscillator $V_L \sin(\omega_r t + \theta_{ref})$ illustrated in in fig. 3.7.

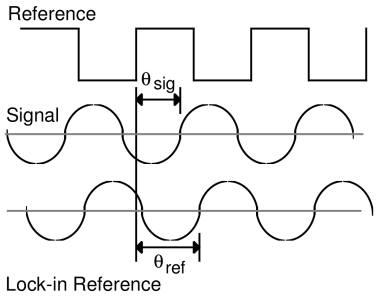

FIGURE 3.7: Illustration of the frequency of the modulation (e.g. a chopperwheel) and the resulting frequency in the signal and internal reference signal of the lock-in amplifier.

Low-pass filter & Time Constant

The low-pass (LP) filter determines the frequency bandwidth of the lock-in measurement. As can be seen in fig. 3.6 the LP-filter is applied after the PSD to attenuate the high-frequency noise components. The LP bandwidth is set by the filter roll-off n and time-constant τ. Equation 3.1 describes the filter's transmittance as a function of the time-constant τ, the slope roll-off n and the frequency ω.

$$T_{LP} = \left(\frac{1}{\sqrt{1 + (\omega\tau)^2}} \right)^n \tag{3.1}$$

The low-pass filter roll-off is determined through the amount of low-pass filters used. The roll-off order n, i.e. the number of filters, influences the bandwidth. A higher order results in a sharper filter.

The time constant is a measure for the time over which the lock-in input is Fourier-transformed to determine the frequency components. The time constant is inversely related to the filter bandwidth. Therefore, a large time constant means a sharp bandwidth.

The filter roll-off and time constant are connected in their experimental impact. Increased time constant and filter roll-off decrease the bandwidth , but share their trade-off of increasing the time needed for a measurement. The frequency bandwidth is inversely connected to the required time for the system to reach an equilibrium value. Therefore a waiting time must be included between consecutive measurements for independent, uncorrelated results. The increased measurement time is the direct trade-off for a narrow bandwidth.

TABLE 3.1: Overview of frequency bandwidth and associated necessary minimal waiting time for different time constants and filterslopes.

		Timeconstant									
		30ms		100ms		300ms		1s		3s	
Filterslope	6dB	8.33 Hz	0.15 s	2.5 Hz	0.5 s	0.83 Hz	1.5 s	0.25 Hz	5 s	0.083 Hz	15 s
	12dB	4.76 Hz	0.21 s	1.43 Hz	0.7 s	0.48 Hz	2.1 s	0.14 Hz	7 s	0.05 Hz	21 s
	18dB	3.70 Hz	0.27 s	1.11 Hz	0.9 s	0.37 Hz	2.7 s	0.11 Hz	9 s	0.04 Hz	27 s
	24dB	3.33 Hz	0.3 s	1 Hz	1 s	0.33 Hz	3 s	0.1 Hz	10 s	0.03 Hz	30 s

Dynamic Reserve

The Dynamic Reserve is a very abstract but key parameter for a lock-in amplifier. Dynamic reserve is denoted in decibel, given by eq. 3.2, it relates the signal- V_{signal} to the noise amplitude V_{noise}. A dynamic reserve of 60 dB implies that some signal buried by noise 6 times larger in magnitude should still be 'resolvable'[3]. Apart from the ambiguity in its definition however, changing the dynamic reserve has great impact on lock-in amplification.

$$\text{Dynamic Reserve(dB)} = 20\log_{10}\frac{V_{noise}}{V_{signal}} \tag{3.2}$$

Amplification of the signal occurs at three different stages in the signal processing scheme, illustrated in fig. 3.6. The first amplification stage is at the Low Noise Differential Amplifier directly after the input, secondly after the notch filters right before the PSD and finally after the LP filter the last amplification takes place. Changing the dynamic reserve redistributes the amplification over the amplification stages. The final goal is a signal amplified to a full-scale readout value. Preferably only the signal is amplified. Throughout the lock-in scheme frequencies other than the signal frequency are attenuated. Correct distribution of the gain, results in amplifying the input frequency at which the signal is found. To that end, in theory, it is preferable that all the amplification takes place after all filtering stages along the chain when solely the signal remains. This is the configuration for High Reserve in which the DC gain after the LP filter is very large and the input amplifier runs at very small at gain. This allows the lock-in to selectively amplify a signal to a full scale signal in the readout electronics. Homogeneous amplification would also amplify large noise components at nearby frequencies. That amplified noise then supersedes the operation ranges and causes overloading.

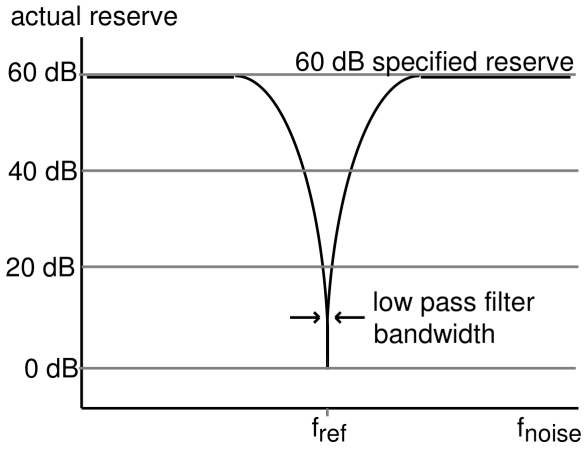

FIGURE 3.8: Dynamic Reserve as a function of frequency. The schematic representation shows how the reserve increases with increasing difference with respect to the reference frequency.

Input connection

The input connection can be set to Single-Ended Voltage, Differential Voltage or Current with two different pre-amplifier options. The differential voltage connection is preferred to single-ended connection. The former solely uses the inner conductors of two separate BNC cables, avoiding any noise pickup on the outer shields. Care must be taken not to have magnetic pickup in the area enclosed by the two BNC cables.

[3] In literature it is often defined as: (1) the ratio of the largest tolerable noise signal to the full scale signal[69] or as (2) the worst ratio upto which the noise can supersede the lock-in's selected sensitivity range for the signal without overloading of the systems electronics[48]. The ambiguity for the former lies with definition of what 'tolerable' entails. The second is so broad (clearly there should not be an overload) that it neither offers any new insight.

The SR830 lock-in amplifier overloads with a to high electrical current input. Therefore only for high impedance ($\gtrsim 10\text{M}\Omega$) samples direct current measurement is possible, avoiding the need of a shunt resistance.

Input Grounding
Input Grounding can be set to either a $10\text{k}\Omega$ (Floating) or 10Ω (Grounded) resistor that connects the BNC shields to the ground. It allows 'floating' of the experiments ground potential with respect to the lock-in's. However, any noise pickup on the shields[4] of the BNC cables will add to lock-in noise. Therefore the Grounded option is preferred when the lock-in amplifier and experiment operate with respect to the same ground potential.

AC Coupling
AC Coupling is useful to remove any DC offset in the input signal. It applies a high-pass filter to the input signal. It only attenuates very low frequency components between DC and $160\,\text{mHz}$. Otherwise any DC offset will be multiplied by the reference frequency at the PSD and fed to the LP filter. If the DC offset is larger than the applied LP filter attenuates, it ends up in the output.

Notch filters
The notch filters attenuate line frequency components at $50\,\text{Hz}$ and $100\,\text{Hz}$ from the input before the gain stage. Effective use decreases the necessary dynamic reserve. The notch filters can be used without drawback for reference frequencies with at least $10\,\text{Hz}$ difference to the line frequencies.

3.1.4 Measurement Protocol

A custom written LabVIEW[5] program controls the setup from a PC. Measurement paramaters are entered into the program prior to a measurement scan. Subsequently the setup scans through the entered spectral range, executing the measurement protocol shown below for the selected wavelengths.

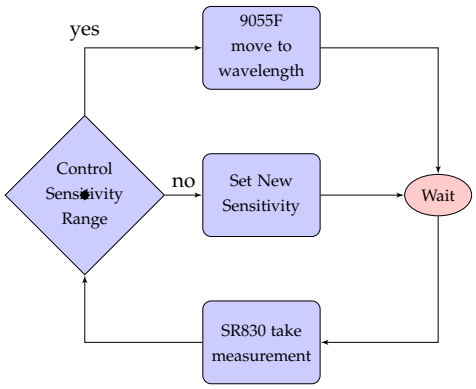

Once the monochromator has selected a new wavelength first (1) the system pauses a certain dwell-time depending on the time constant and filter roll-off (see page 26). Next (2) the lock-in amplifier is triggered to sample N measurement points into its internal buffer at a set repetition rate. After (3) filling the internal buffer the averaged value is checked to fall within the active sensitivity range of the lock-in amplifier. For an incompatible sensitivity (4) the parameter is changed and the setup pauses a new dwell-time for the readout value to re-equilibriate. When the measurement returns an averaged result within the sensitivity bounds (5) the data is recorded and the monochromator moves to the next wavelength.

[4] Noise pickup on the BNC shields is not filtered by the lock-in technique. Common mode noise between the center BNC conductor and the shields, however is rejected[69].
[5] LabVIEW version 2010, 32bit

TABLE 3.2: Overview of the different organic semiconducting materials and morphologies studied in this research.

	Rubrene	TIPS pentacene	TIPG pentacene
Single crystals	✓	✓	✗
Inkjet printed crystals	✗	✓	✗
Thin films	✓[6]	✓	✓

3.2 Samples

Samples made of three organic semiconducting materials were considered in this research (section 2.1.5). Out of these materials samples with different morphology and thickness were investigated (section 2.1.3). Additionally, different methods of mounting the electrodes onto the samples were studied. In the following paragraphs the differences are set out between the various samples.

The investigated organic semiconducting materials were rubrene, TIPS and TIPG. Samples of the three morphologies: SC, thin film and IP were available for these materials, depending on applicability of the necessary fabrication techniques. The different morphologies that were available per organic material can be seen in table 3.2. Rubrene samples were investigated with SC and thin film morphology. For the TIPS samples also IP samples are part of the research and the TIPG semiconductor was only available as thin film. Lastly, this research aims to provide insight in the impact of film thickness on the photocurrent. To this end rubrene films with thicknesses 13 nm, 52 nm and 101 nm have been measured.

The rubrene SC and thin film samples were synthesized at the University of Milan - Bicocca. The SCs were grown using PVT[73]. The thin films were grown on β-alanine substrates with organic molecular beam epitaxy (OMBE)[74].

The TIPS SCs were grown from solution at the University of Trieste. Also at the University of Trieste the IP crystals were fabricated. The TIPS thin films were made with drop-casting in-house at the University of Bologna.

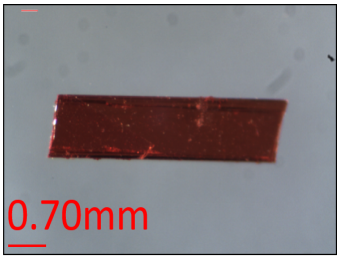

3.9 (A) Rubrene Single Crystal

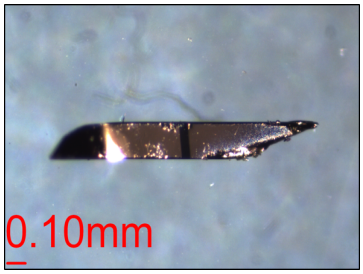

3.9 (B) TIPS Pentacene Single Crystal

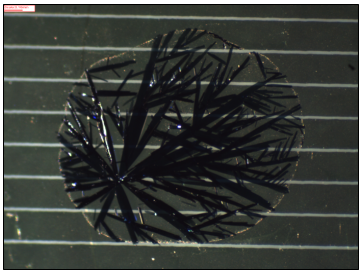

3.9 (C) TIPS Inkjet-Printed Crystal

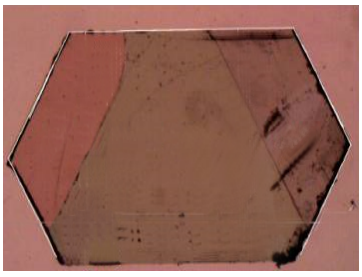

3.9 (D) Rubrene Thin Film

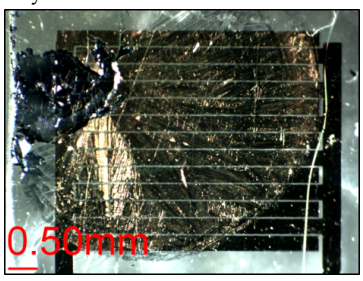

3.9 (E) TIPS Pentacene Thin Film

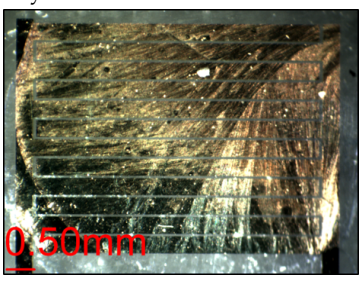

3.9 (F) TIPG Thin Film

[6]Rubrene thin films were also studied with different thicknesses: 13 nm, 52 nm and 101 nm.

3.2.1 Electrodes

The electrical connection with the samples is made via gold electrodes to which then electric wiring is soldered. The samples and electrodes are mounted on PET substrates. The TIPS pentacene thin films and IP crystals as well as the TIPG sample are deposited directly onto pre-fabricated, interdigitated electrodes illustrated in fig. 3.10a.

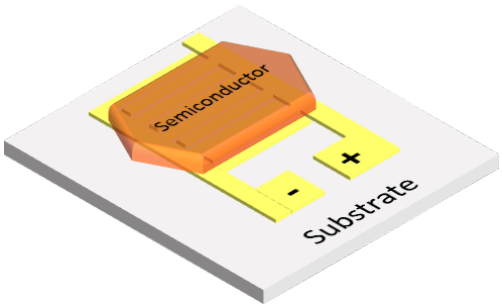

3.10 (A) Pre-fabricated, interdigitated eletrodes on PET substrate. The semiconductor is deposited directly on top of the electrodes.

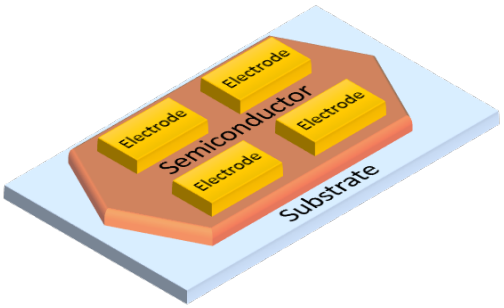

3.10 (B) Custom electrodes placed along the surface crystallographic axes of the semiconductor. The substrate is made of glass.

3.2.1.1 Photocurrent Anisotropy

Another goal of this research is the investigation of photocurrent anisotropy along different crystalline axes (see section 2.1.3). To this end the rubrene SC and thin film samples were prepared with electrodes attached along the α, β and γ crystallographic axes. The TIPS SCs were prepared with electrodes solely along the β-axis, with the highest carrier mobility.

These electrodes were fabricated in-house. The electrodes were made using thermal evaporation while masking the sample ensuring a channel separating the electrodes. The evaporation was carried out at high vacuum (10^{-5} Torr) from a thin tungsten wire ($\varnothing = 0.5$ mm). Gold wires ($\varnothing = 50$ μm) were used as mask.

In fig. 3.11 is shown how three different electrode geometries were used: between the sample and the substrate (BOTTOM), on top of the sample (TOP) and with a single electrode on either side of the sample (CROSS). The first two co-planar geometries specifically measure a surface current between the electrodes whereas the latter measures the current through the bulk.

Between the gold electrodes and the glass substrate a chromium adhesion layer is necessary. The adhesion layer is also made using thermal evaporation. First the glass, chromium and gold are cleaned sequentially in aceton, iso-propenol and deionized water baths. Afterwards, in a single execution, first the chromium is deposited onto the glass and next the gold is deposited onto the chromium layer. The thickness of the adhesion layer were determined and checked by means of atomic force microscopy (AFM). Subsequently also the width and depth of the channel between the gold electrodes were checked.

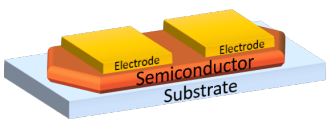

3.11 (A) TOP

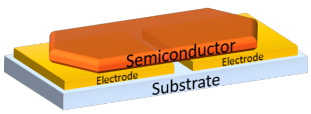

3.11 (B) BOTTOM

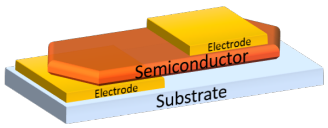

3.11 (C) CROSS

FIGURE 3.11: Custom electrodes placed either co-planar in the TOP or BOTTOM geometry or bi-planar in the CROSS geometry.

Chapter 4

Results

In the following chapter the experimental results are presented. It consists of three parts. The first addresses the setup characterization, calibration and optimization and presents the parameter values crucial for the following measurements. The middle part comprises the measurement results for the investigated samples. Finally the last part addresses the margin of error in the experimental data.

4.1 Setup Parameters

In the following sections the results of the spectral calibration, determination of the photon flux and experimental background noise analysis are presented.

4.1.1 Spectral Calibration

The monochromator has been calibrated for optimal spectral resolution and reproducibility. The calibration has been carried out with a mercury (Hg) source and a field-effect transistor (FET) amplified ultraviolet enhanced (UVS) photo-diode from Electro-Optical Systems Inc[2].

A slight mismatch in the calibration results has been observed between the two output slits. Consequently separate calibrations were performed. The monochromator side output has been used throughout this research and its calibration results are presented in fig. 4.1.

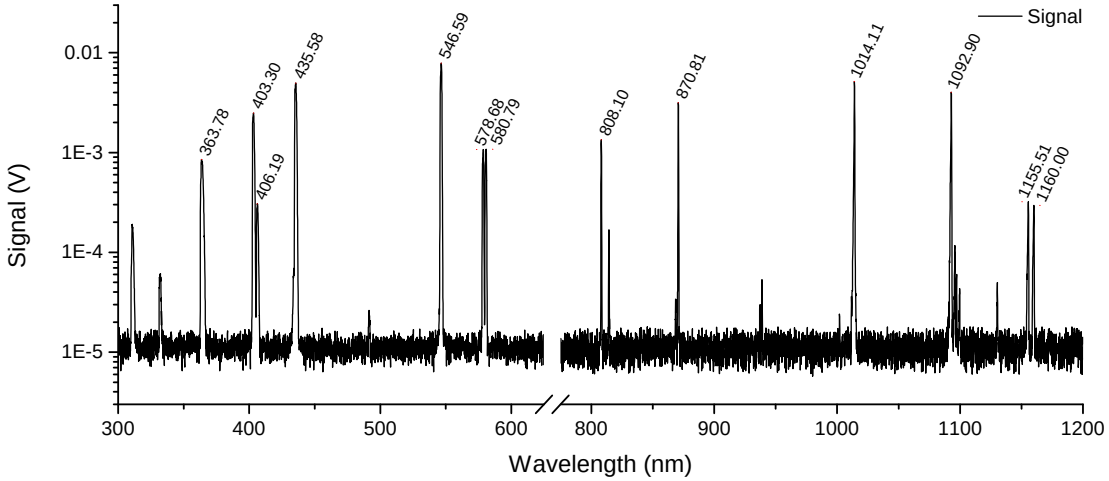

FIGURE 4.1: The Hg emission spectrum measured with a FET amplified UVS photodiode. Clear Hg emission lines are seen in the spectrum. The monochromator's mechanical accuracy limits the spectral resolution to $0.20(3)\,\mathrm{nm}$. Note the logarithmic scale on the y-axis.

The results were compared to the Hg persistent emission lines established by *NIST*[36]. The deviations in the detected peaks compared to the literature values are plotted against the corresponding wavelengths in fig. 4.2. The deviation scales with the diffraction order. Therefore higher order diffraction peaks have been compensated for their order.

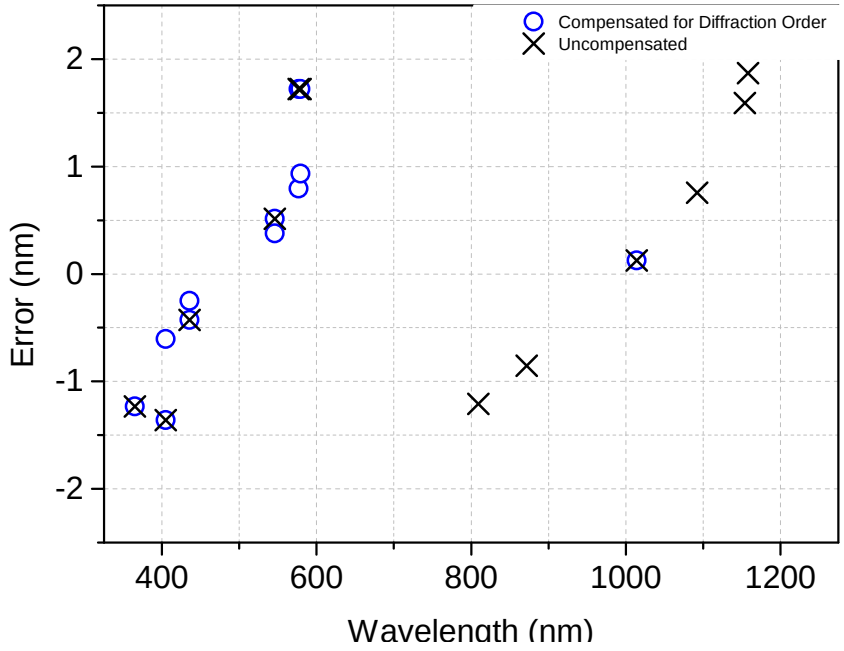

FIGURE 4.2: Deviation between Hg emission lines as defined by *NIST* and the measured peak wavelengths. The crosses illustrate the raw deviations and circles the values compensated by dividing the deviations by the diffraction error. For the compensated peaks the average deviation is $0.19\,\mathrm{nm}$ with a SD of $1.02\,\mathrm{nm}$.

The averaged deviation between the *NIST* values and the wavelengths found for the compensated emission peaks is $0.19(102)\,\mathrm{nm}$. This average systematic error agrees with the mechanical accuracy of the monochromator[62].

4.1.1.1 Monochromator Broadening

The spectral resolution of the setup can be determined from the FWHM of the measured peaks (see page 16). Therefore the peaks in the Hg spectrum were fitted with a Lorentzian function[1], from which the FWHM was taken. The indivual results are presented in table 4.1 along with the average FWHM value $0.63(36)$. Consequently the Hg spectrum in fig. 4.2 has a resolution of $0.63(36)\,\mathrm{nm}$.

TABLE 4.1: Monochromator broadening of emission lines.

	1	2	3	4	5	6	7	8	9	10	11	12	13	μ
Peaks	363.78	403.30	406.19	435.58	546.59	578.68	580.79	808.10	870.81	1014.11	1092.90	1155.51	1160.00	
FWHM	1.61	1.06	0.63	1.12	0.92	0.78	0.76	0.35	0.34	0.42	0.44	0.60	0.62	0.63(36)

[1]The natural linewidth of spectral emission lines has a Lorentzian shape: $\mathcal{L}(\omega) \equiv \frac{1}{\pi}\frac{1/\gamma}{(\omega-\omega_0)^2+(1/\gamma)^2}$, in which ω is the frequency, ω_0 the central peak frequency and γ the peak's FWHM[34]. $\mathcal{L}(\omega)$ is rewritten straightforwardly for wavelengths with the substitution $\lambda = \frac{2\pi c}{\omega}$. The fitting was performed with Originlab 9 Pro.

4.1.2 Photon Flux

A accurately defined photon flux is of importance due to the nonlinear sample response for high fluxes, see section 2.1.6.1. The pyroelectric detector has been gauged to determine the specific photon flux per wavelength incident on the samples. A relatively indirect approach has been necessary since neither the spectrum of the lamp nor the pyroelectric detector were calibrated. In fact, only the photodiode's responsivity is clearly defined by the manufacturer[2]: $0.6 \times 10^7\,\mathrm{V\,W^{-1}}$ at the peak of its spectral response curve (attached in appendix B). From the curve the peak wavelength value $763.31(92)\,\mathrm{nm}$ has been extracted[2].

Furthermore the responsivities of both the PD and PED depend on the illuminated area of the detector and the modulation frequency of the light. The detector area of the photodiode was vignetted to allow its operation for the same light intensities as necessary for the less sensitive PED. Next the frequency dependence of both detectors has been determined and, along with the vignetting details, has been enclosed in appendix B.

In the final configuration the monochromator was set at $763.31(92)\,\mathrm{nm}$, the chopperwheel operating at $1\,\mathrm{Hz}$ and the PD vignetted. The photon irradiance, calculated from the detector signal S_V using eq. 2.14, was $E_e = 2.11 \times 10^{11}\,\mathrm{s^{-1}\,mm^{-2}}$.

The pyroelectric detector's responsivity was calculated backwards from the established photon irradiance at equivalent conditions. The responsivity of $1624.05(272)\,\mathrm{V\,W^{-1}}$ at $1\,\mathrm{Hz}$ signal modulation agrees well with literature values for similar models[57].

With the established responsivity it has been possible to determine the dependence of the photon irradiance on the slit width and the source's operating power. Figure 4.3a and fig. 4.3b show the photon irradiance for varying experimental configuration. Both dependencies have been established with the PED and the PD at $763.31(92)\,\mathrm{nm}$, equal modulation frequency and fixed output slit width of $750(5)\,\mu\mathrm{m}$ that sets the spectral bandwidth.

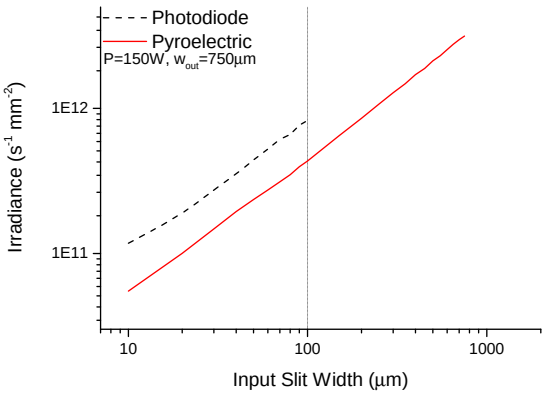

4.3 (A) A linear relation between slit width and photon irradiance for an illuminating light spot overfilling the input slit. The data is collected for fixed $150\,\mathrm{W}$ lamp output power and $750(5)\,\mu\mathrm{m}$ output slit. The high sensitivity of the photodiode restricts the maximal slit width. The vertical dotted line indicates the configuration equivalent to fig. 4.3b.

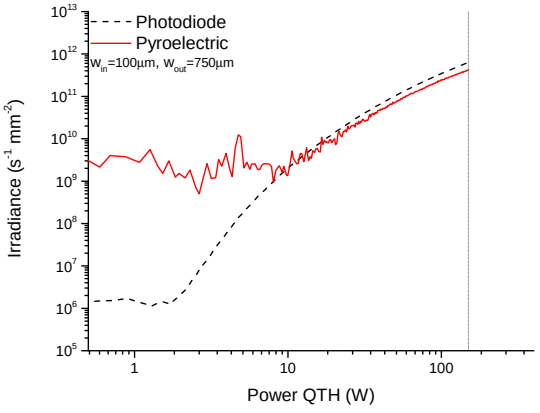

4.3 (B) Photon irradiance relation to QTH lamp output power for constant in- and output slits at $100(5)\,\mu\mathrm{m}$ and $750(5)\,\mu\mathrm{m}$. The PED can not correctly detect irradiances below $3 \times 10^9\,\mathrm{s^{-1}\,mm^2}$. The vertical dotted line indicates the configuration equivalent to fig. 4.3a.

[2]The curve has been digitized with roughly $0.9(2)\,\mathrm{nm}$ resolution. Next the peak value was calculated with Originlab 9 Pro. It was calculated by interpolating the function and calculating the maximum from the derivative.

Figure 4.3a shows the linear increase of irradiance for increasing the width of only the input slit. The linear relation is expected as the input slit is overfilled by the illuminating spot. Therefore widening the slit only increase the width of the effective aperture area. The PD data is restricted to narrower slit widths because of the photodiode overloading at higher irradiance. The measurement has been carried out at constant, maximal source operating power of $150\,\mathrm{W}$.

In fig. 4.3b the operating power dependency of the photon irradiance is shown. For constant input- and output slit of $100(5)\,\mu\mathrm{m}$ and $750(5)\,\mu\mathrm{m}$ an exponential relation is found between the operating power of the QTH source and the photon irradiance. The graph also shows that irradiances roughly $E_p < 3 \times 10^9\,\mathrm{s}^{-1}\,\mathrm{mm}^2$ fall outside the sensitivity range of the PED.

4.1.3 Signal Processing

The PC spectrum has a discontinuity at $700\,\mathrm{nm}$. At that wavelength the monochromator's gratings change to maintain an efficient diffraction, as mentioned in section 3.1.2.1. The light diffracted from the second grating, covering a range from $700\,\mathrm{nm}$ and onward, has a higher intensity. Consequently the optical intensity suddenly changes. This sudden change is compensated by the normalization of the PC with respect to the spectral distribution of the incident radiation. The spectrum was measured with the PED and was used as the reference data for th normalization, shown in fig. 4.4.

Figure 4.4 also shows the effect of the Savitzky-Golay smoothing algorithm[29]. For noise obscured spectra this algorithm was used as a filter to enhance the clarity of the signal. The algorithm is a common function in signal processing software[3]. The algorithm takes a preset number of data points and finds a polynomial using a linear least squares method. Clearly the use of this filter decreases resolution due to the approximation. In specific cases the choice was made to still apply the filter as the increase in graph quality outweighed the more coarse resolution. It is always indicated on the graph axis whenever the photocurrent is smoothed. A full treaty on this algorithm goes beyond the scope of this research but can be found in the original article Savitzky and Golay [60].

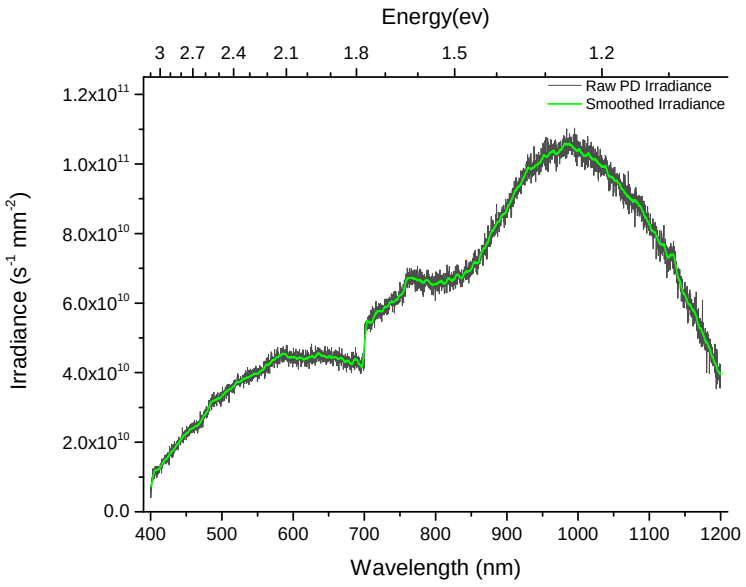

FIGURE 4.4: The spectrum as measured with the PED at the sample stage. The graph shows the sudden change in irradiance due to the grating change at $700\,\mathrm{nm}$. Additionally the effect of the Savitzky-Golay filter is presented by the raw dark graph and the smoothed light curve. The theoretical spectral resultion is $0.2\,\mathrm{nm}$.

[3]The software used in this research was Originlab 9 Pro.

4.1.4 Noise Analysis

A study has been carried out to distinguish the various sources and corresponding magnitudes of noise inherent to the setup. Specifically the noise distribution over different frequency ranges has been investigated. The approach was to start from the internal noise intrinsic to the lock-in amplifier and sequentially add components of the experimental setup to the electrical circuit. First of all the built-in function for noise measurements was tested along with various parameter configurations of the lock-in. In appendix C the complete analysis and accompanying graphs are presented. The following part addresses the final findings.

A distinction between voltage and current measurements needs to be made. The shunt resistance introduces noise proportional to the square root of its magnitude (see section 3.1.3.1). Figure 4.5 illustrates the difference in the noise spectrum for measurements with a shunt resistance and without. The frequency distribution of the noise in a current measurement shows a $^1/_f$ drop for frequencies roughly below 100 Hz beyond which Johnson-noise from the sample dominates and the noise no longer shows a clear frequency dependence. The frequency dependent decrease of noise in the low frequency regime for the voltage measurement is less strong. This is due to the increased resistance in the circuit, enlarging the noise throughout the entire frequency spectrum. The Johnson noise, that the resistance introduces to the measurement, sets the noise floor.

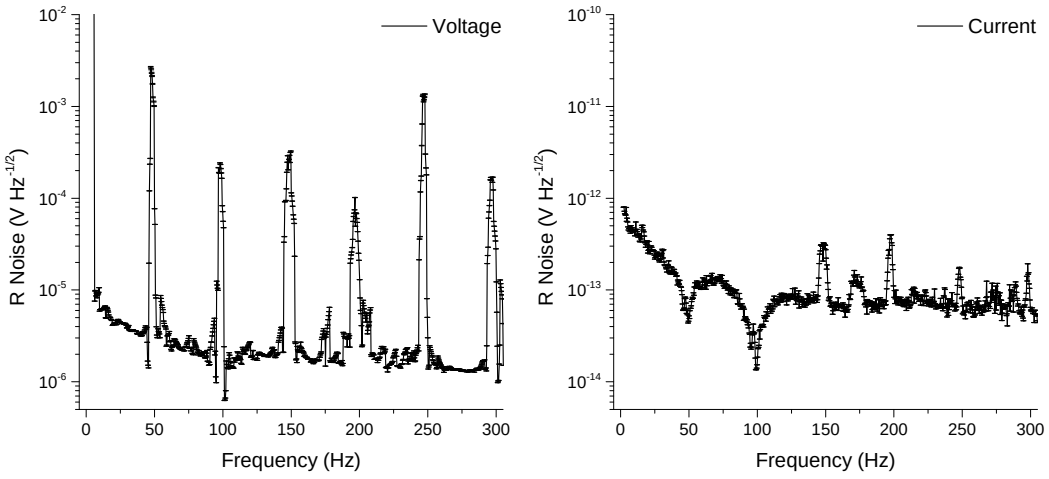

FIGURE 4.5: Noise measurements with a shunt resistance and of the electrical current.

4.2 Rubrene

The present section contains the results of the photocurrent spectroscopy measurements on rubrene. The measured data is normalized for the spectral distribution of the incident light. Figure 4.4 presents the reference spectrum used for the normalization[4]. Each graph is normalized with respect to its highest peak. Finally the normalized PC is plotted as a function of wavelength. The energies corresponding to the wavelength are plotted on the top-axis. The spectral resolution for each measurement is added to the graph caption. All measurement were conducted with a $410\,\mathrm{nm}$ to $1200\,\mathrm{nm}$ bandpass filter. The spectra for rubrene were measured from $410\,\mathrm{nm}$ to $650\,\mathrm{nm}$.

4.2.1 Photocurrent in Rubrene Single Crystals

4.2.1.1 Symbatic and Antibatic Photocurrent Response

In fig. 4.6 the solid curves show the normalized photocurrent response of two similar rubrene single crystals. The dashed curve represent the spectral absorption for rubrene as measured by Najafov et al. [51]. The photocurrent in both crystals is measured along the same crystalline axis and coplanar electrode geometry (TOP). From AFM measurements the crystals thickness was determined. TOP I (black) is $5.23\,\mu\mathrm{m}$ thick and TOP II (blue) is $6.27\,\mu\mathrm{m}$ thick. The potential bias applied to both samples was $1.5\,\mathrm{V}$ and the spectral resolution for this measurement was $0.2\,\mathrm{nm}$.

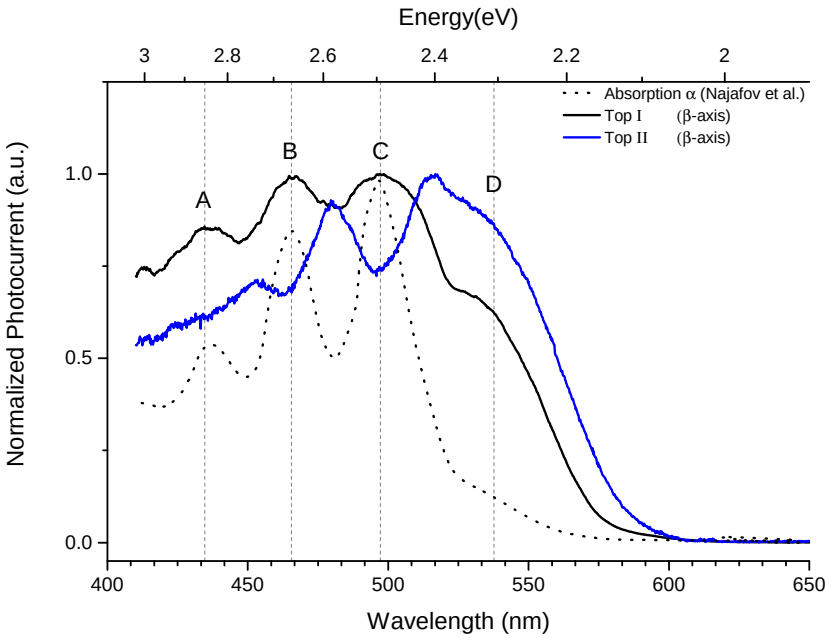

FIGURE 4.6: Photocurrent response of two rubrene single crystals with coplanar electrodes placed on top of the samples. The photocurrents are symbatic (black) and antibatic (blue) with respect to the absorption curve (dotted) from Najafov et al. [51] The symbatic maxima, coinciding with the antibatic minima, are found at $434.8\,\mathrm{nm}$, $466.4\,\mathrm{nm}$, $497.4\,\mathrm{nm}$ and $537.6\,\mathrm{nm}$. The PC spectra were acquired with a $1.5\,\mathrm{V}$ bias and the final data has $0.2\,\mathrm{nm}$ resolution.

From fig. 4.6 clearly follows that TOP I (black) has a symbatic photocurrent spectral response with respect to the spectral absorption. Good agreement is seen between the peaks in the absorption and the photocurrent at $434.8\,\mathrm{nm}$, $466.4\,\mathrm{nm}$, $497.4\,\mathrm{nm}$ and $537.6\,\mathrm{nm}$. In comparison to the absorption curve, the features in the photocurrent are less emphasized or seem somewhat smoothed or damped.

[4]The smoothed curve is used to avoid features in the normalized spectrum that originate from the reference spectrum.

TABLE 4.2: Energy values corresponding to the spectrum peaks in fig. 4.6. Added to the right are the differences in energy between adjacent peaks known as Davydov splitting. The uncertainty in the energy values is $\pm 0.001\,\mathrm{eV}$.

	A	B	C	D	ΔE_{D1}	ΔE_{D2}	ΔE_{D3}
Absorption α	2.845	2.658	2.489		0.187	0.169	
TOP I	2.852	2.658	2.493	2.306	0.193	0.166	0.186
TOP II (Minima)		2.681	2.503			0.179	
TOP II (Peaks)	2.732	2.576	2.424	2.399	0.155	0.153	0.125

A striking result from fig. 4.6 is the antibatic response of TOP II (blue). Despite the similarities to the other sample, the TOP II (blue) sample shows a anti-correlated response compared to the spectral absorption and previous sample. The features in the photocurrent curve are again less pronounced than the spectral absorption. Especially the photocurrent resulting from shorter wavelengths displays less features and is neither sym- nor antibatic.

4.2.1.2 Photocurrent Anisotropy

Coplanar perpendicular axes

The photocurrent has been measured in the same sample TOP I. It has been measured along the two perpendicular crystalline axis via coplanar electrodes placed on top of the sample. The normalized photocurrent is plotted in fig. 4.7. The potential bias applied to the sample was $1.5\,\mathrm{V}$ and the spectral resolution for this measurement was $0.2\,\mathrm{nm}$.

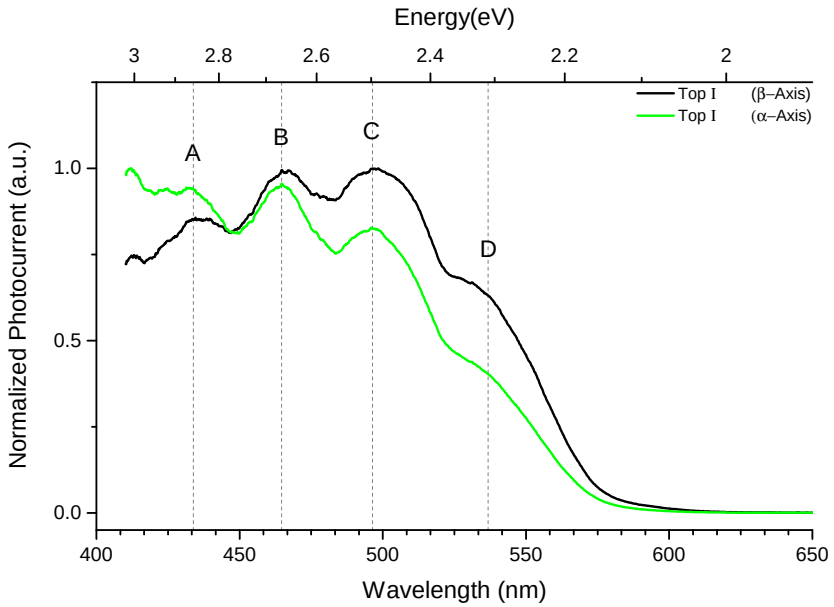

FIGURE 4.7: Photocurrent response of coplanar perpendicularly placed electrodes on the same single crystal sample. The electrodes were placed on TOP of the sample along the β axis (black) and α axis (green). The black curve in fig. 4.7 and fig. 4.6 is the same measurement. The PC spectra were acquired with a $1.5\,\mathrm{V}$ bias and the final data has $0.2\,\mathrm{nm}$ resolution.

The peaks for both curves along either axes agree well. However, for the long crystalline β-axis along which the charge mobility is highest, longer wavelengths relatively contribute more to the photocurrent. For the α-axis a relative increase for shorter wavelengths is seen. Furthermore a slight change in the onset of the bandgap is seen.

Coplanar and Biplanar electrode geometries

Figure 4.8 presents the photocurrent results for three similar samples measured with the different electrode geometries: TOP, BOTTOM and CROSS. The samples are measured along the crystalline β-axis except the CROSS-sample which' photocurrent also has a γ component. The crystals have similar thicknesses ranging from $4\,\mu m$ to $6\,\mu m$. The PC spectra were acquired with a $1.5\,V$ bias and the final data has $0.8\,nm$ resolution

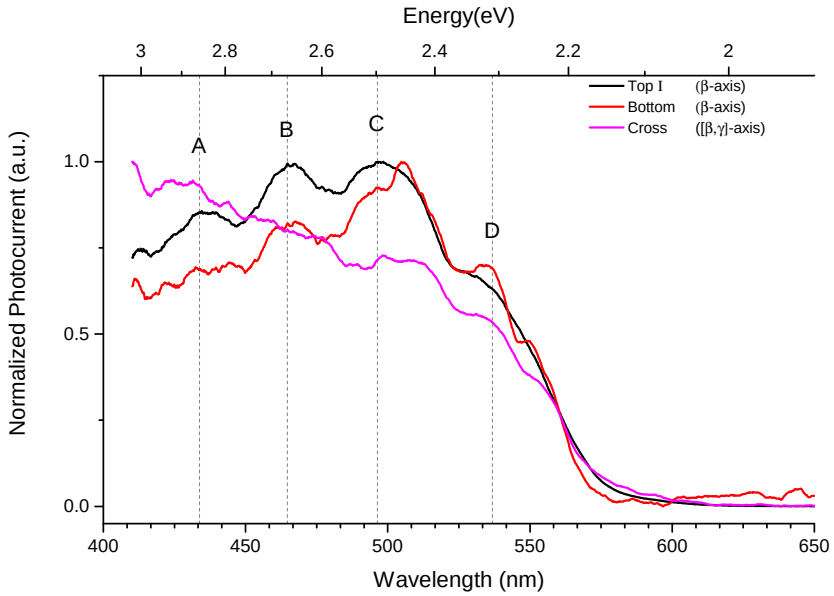

FIGURE 4.8: Photocurrent responses of three single crystal samples with TOP, BOTTOM and CROSS placed electrodes. The PC spectra were acquired with a $1.5\,V$ bias and the final data has $1.8\,nm$ resolution

For both coplanar TOP and BOTTOM geometries the photocurrent curves show a similar decrease for wavelengths longer than $510\,nm$ upto the bandgap. For shorter wavelengths the relative contribution to the photocurrent decreases in the BOTTOM sample.

This result can be explained by the shorter wavelengths having a larger penetration depth due to their decreased absorption (see fig. 4.6). As the light is incident on the top surface any charge carriers will be created farther from the surface. After creation the carriers have to dissociate a longer distance through the bulk. It is possible that a portion the the created charge carriers recombines before reaching the electrodes thus not contributing to the measured current.

The CROSS sample displays less pronounced features in its photocurrent curve. As the measurement is along the [0,β,γ] direction and through the bulk of the material, the photocurrent is integrated over those directions. Due to that integration any directional dependent features in the curve may turn out less pronounced.

4.2.2 Photocurrent in Rubrene Thin Films

The following section presents the measurement results for the rubrene thin films. Identically as the single crystal results the PC data is normalized for the incident light and plotted as a function of wavelength.

4.2.2.1 Coplanar TOP electrodes

Photocurrent spectropy measurements have been carried out on rubrene thin films of three thicknesses: $13\,nm$, $52\,nm$ and $101\,nm$. All electrodes were placed on top of the samples in a coplanar fashion. The PC spectra were acquired with a $1.5\,V$ bias and the final data has $0.8\,nm$ resolution

Perpendicular axes

The 13 nm, 52 nm and 101 nm samples were measured four[5] times. Each sample has been measured twice in different parts of the crystal along both their α axis (green & blue) and similarly twice along the β axis (red & black).

The 13 nm film figure contains three curves instead of four due to a disconnected electrode. The two main peaks and onset of the bandgap show good agreement between all three curves. The photocurrents measured along the β axis (red & black) appear higher for shorter wavelengths.

The 52 nm film displays good agreement for the two main peaks and onset of the bandgap between all curves. Contrary to the 13 nm sample the photocurrents for shorter wavelengths measured along the β axis (red & black) appear slightly lower than along the α axis.

The 101 nm film also show very good agreement between all curves for the main peaks and onset of the bandgap. No significant an-isotropic difference in the photocurrent for shorter wavelengths is seen.

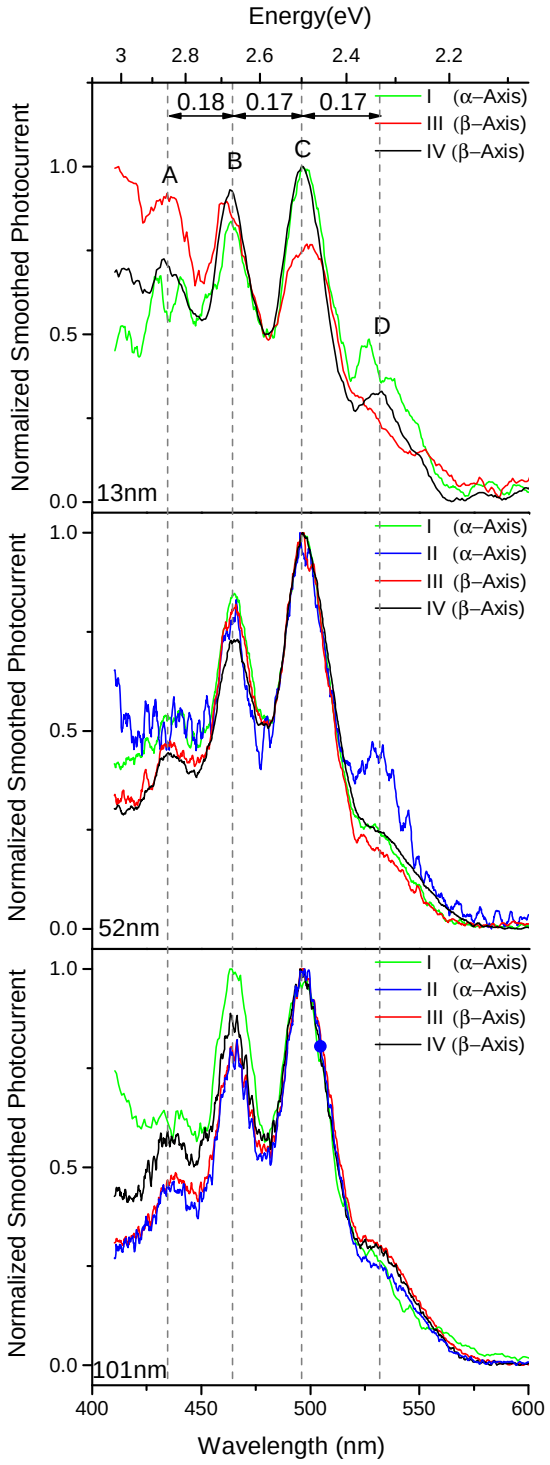

FIGURE 4.9: Photocurrent responses of rubrene of 13 nm, 52 nm and 101 nm thin films, combined per graph from top to bottom. For each thickness the PC results are shown for electrodes along the β axis (red & black) and α axis (green & blue). The PC spectra were acquired with 1.5 V bias and 0.8 nm resolution

[5]Except the 13 nm thin film sample for which 1 measurement is missing due to disconnected electrodes for 1 measurement.

Different Thickness

fig. 4.10a and fig. 4.10b contain the photocurrent spectra per crystalline axis compared for thicknesses 13 nm, 52 nm and 101 nm. For both axes there is good agreement for the main peaks and bandgap onset. Figure 4.10a indicates that for thinner films the features in the photocurrent are more strongly pronounced along the α axis. However, along the β axis only for the 13 nm sample emphasized features are seen in fig. 4.10b. Between the 52 nm and 101 nm films an excellent match between the photocurrents is found. It seems that for films thicker than $\geq$50 nm the response does not drastically change with thickness.

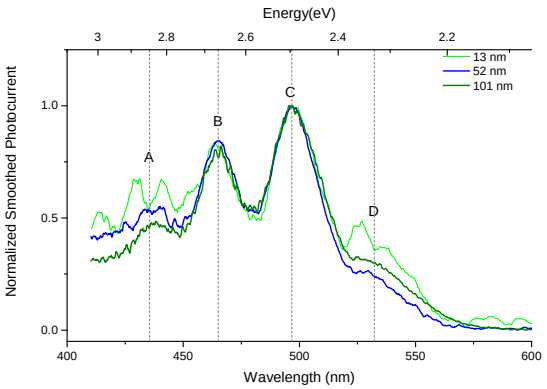

4.10 (A) PC along the α axis in rubrene 13 nm, 52 nm and 101 nm thin films. The PC spectra were acquired with 1.5 V bias and 0.8 nm resolution.

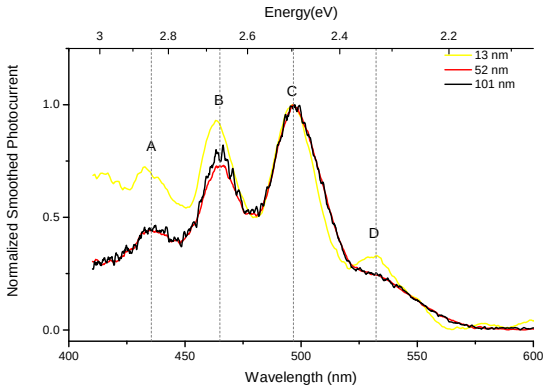

4.10 (B) PC along the β axis in rubrene 13 nm, 52 nm and 101 nm thin films. The PC spectra were acquired with 1.5 V bias and 0.8 nm resolution.

From fig. 4.10a and fig. 4.10b can be seen that the thinnest 13 nm sample shows increased photocurrent response for the shortest wavelengths. Especially along the highest mobility β axis this behavior is clearly seen.

4.2.2.2 Coplanar and Biplanar Electrode Geometries

Rubrene thin films have been mounted with electrodes in TOP, BOTTOM and CROSS geometries and were measured in the same fashion as the single crystal samples. Their photocurrents are displayed in fig. 4.11. All samples are measured along the β axis, except again the CROSS-sample which' photocurrent also has a γ component beside the β component.

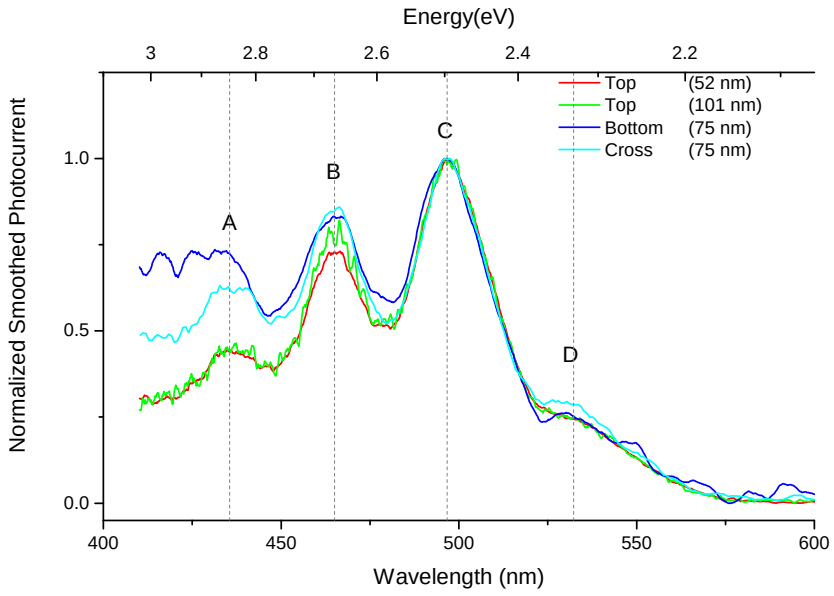

FIGURE 4.11: PC in rubrene thin films of comparable thickness with TOP, BOTTOM and CROSS placed electrodes. The PC in each sample was measured along the β axis (for the CROSS also along the γ axis). The PC spectra were acquired with $1.5\,\mathrm{V}$ bias and $0.8\,\mathrm{nm}$ resolution.

Note that the samples have different thickness; $52\,\mathrm{nm}$, $75\,\mathrm{nm}$ and $101\,\mathrm{nm}$. However, from fig. 4.10b in the previous paragraph, the photocurrent for samples thicker than $\geq 50\,\mathrm{nm}$ does no longer drastically change with thickness. Therefore the differences for the photocurrent curves seen in fig. 4.11 are believed to primarily result from the different electrode placements.

Figure 4.11 presents excellent correlation between the different geometries for the bandgap onset and largest peak in the photocurrent spectrum. Conversely to the excellent match for all wavelengths as earlier seen for TOP electrodes, the BOTTOM and CROSS sample responses diverge for shorter wavelengths. The BOTTOM sample displays the relatively highest measured current for short wavelengths and the CROSS mounted sample exhibits an intermediate response.

4.2.3 Photocurrent in Rubrene Single Crystals vs Thin Films

The following section presents the comparison between the rubrene single crystals (SC) and thin films, separately discussed in the preceding paragraphs.

4.2.3.1 Coplanar TOP Electrodes

Figure 4.12 and fig. 4.13 combine the SC and films results with electrodes mounted on TOP of the samples, respectively along the α and β axes. Matched maxima in the photocurrent curves between the films and SC can be distinguished for both crystalline axes. For both directions the bandgap appears red-shifted in the SC, however more clearly along the β axis.

Furthermore it stands out from both fig. 4.12 and fig. 4.13 that the single crystals display more broadened spectra. In addition to the broadening, specifically the shorter wavelengths contribute more in SC samples than thin films. Especially for the α axis this increase for short wavelengths in SC is notable.

Finally, it is noteworthy that the thinnest, $13\,\mathrm{nm}$, film displays more features in the photocurrent spectrum resembling the SC. This is in contrast to the thicker films with thicknesses that are more comparable to the SC.

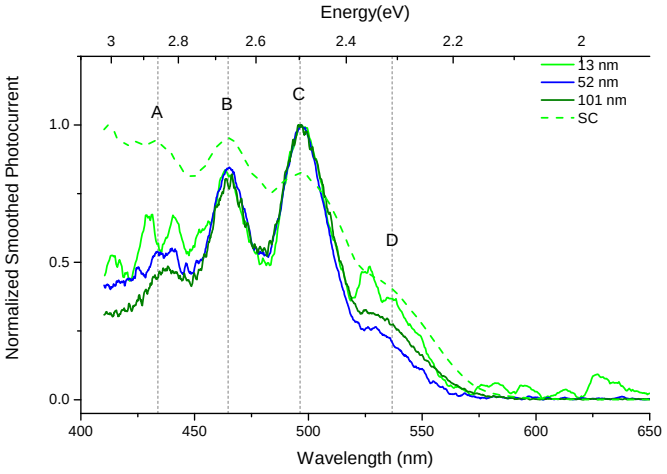

FIGURE 4.12: Comparison of PC spectra in rubrene SC and thin films along the α axis with TOP electrodes. The solid curves correspond to the thin films equivalent to fig. 4.10a and the dashed curve belongs to the SC from fig. 4.7. The PC spectra were acquired with $1.5\,\mathrm{V}$ bias and $0.8\,\mathrm{nm}$.

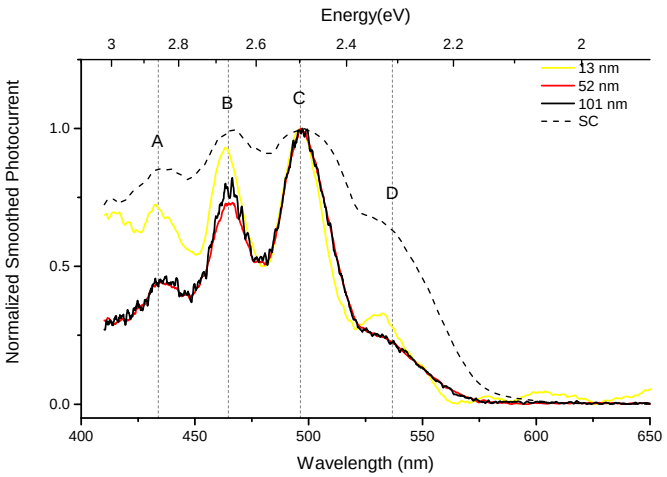

FIGURE 4.13: Comparison of PC spectra in rubrene SC and thin films along the β axis with TOP electrodes. The solid curves correspond to the thin films equivalent to fig. 4.10b and the dashed curve belongs to the SC from fig. 4.7. The PC spectra were acquired with $1.5\,\mathrm{V}$ bias and $0.8\,\mathrm{nm}$.

4.2.3.2 Coplanar and Biplanar Electrode Geometries

fig. 4.14 and fig. 4.15 depict the combined photocurrent spectra of rubrene films and SC's measured along the β axis with BOTTOM and CROSS electrodes. For both geometries the measured spectra display broader peaks for the SC's, equivalent to the samples in the preceding paragraph.

Firstly, fig. 4.14 reveals a mismatch in the primary photocurrent spectrum peak. Secondly the spectra exhibit similar efficiency in the PC response for shorter wavelengths in contrast to the other electrode geometries.

The CROSS mounted samples, shown in fig. 4.15, present far more distinct PC spectra. Primarily the spectrum of the bulk SC sample shows has far less features. Furthermore does the photocurrent in the SC mostly result from shorter wavelengths. Subsequently, the bandgap is seems to red-shifted for the single crystalline morphology.

The suppressed features in the SC curve may be understood as a consequence of integration over the different directional axes along which the current propagates. In general different behavior for bulk- and surface-currents might be suspected. However, the difference between the thick SC and the thin films stands out. This difference may result from a transition in the charge-carrier creation and dissociation mechanisms.

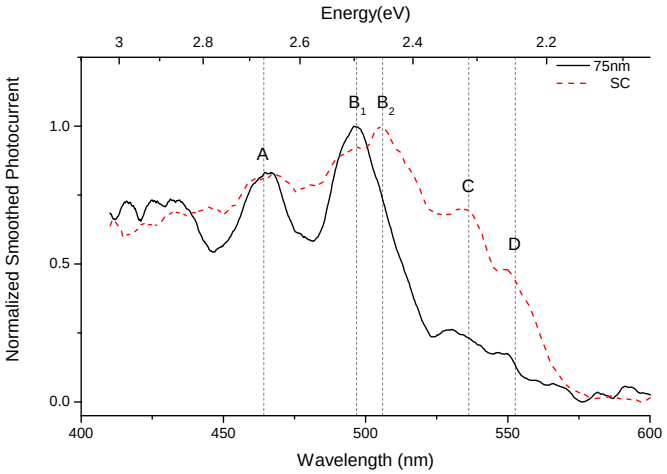

FIGURE 4.14: Comparison of PC spectra in a rubrene SC and thin film with BOTTOM placed electrodes. The solid curves correspond to the thin film from fig. 4.11 and the dashed curve belongs to the SC from fig. 4.8. The PC spectra were acquired with 1.5 V bias and 0.8 nm.

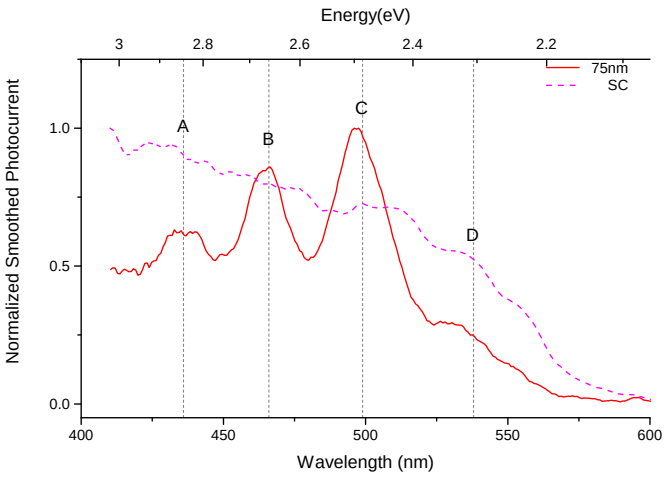

FIGURE 4.15: Comparison of PC spectra in a rubrene SC and thin film with CROSS placed electrodes. The solid curves correspond to the thin film from fig. 4.11 and the dashed curve belongs to the SC from fig. 4.8. The PC spectra were acquired with 1.5 V bias and 0.8 nm.

4.3 Pentacene

This section consists of the results for the pentacene based samples. First, the TIPS samples' PC spectra are demonstrated for each morphology after which their comparison. Finally, the results of the TIPG measurements and the comparison to a TIPS sample is presented.

As usually, the PC data is normalized for the spectral distribution of the incident light and plotted as a function of wavelength. After normalization the data was processed with the Savitzky-Golay smoothing algorithm for clearer graphs. All measurements were conducted with a $1.5\,\mathrm{V}$ bias over the samples and with a $31\,\mathrm{Hz}$ modulation of the light.

4.3.1 Photocurrent in TIPS Single Crystals

The PC in TIPS SCs was measured directly as current along the long β-axis of the crystals (see fig. 4.16). The four crystal had similar thicknesses of $200\,\mu\mathrm{m}$. The spectrum for TIPS was acquired from $410\,\mathrm{nm}$ to $900\,\mathrm{nm}$, the lower boundary set by the bandpass filter that was used. The beyond $900\,\mathrm{nm}$ no PC signal was measured. The spectral resolution is $0.8\,\mathrm{nm}$.

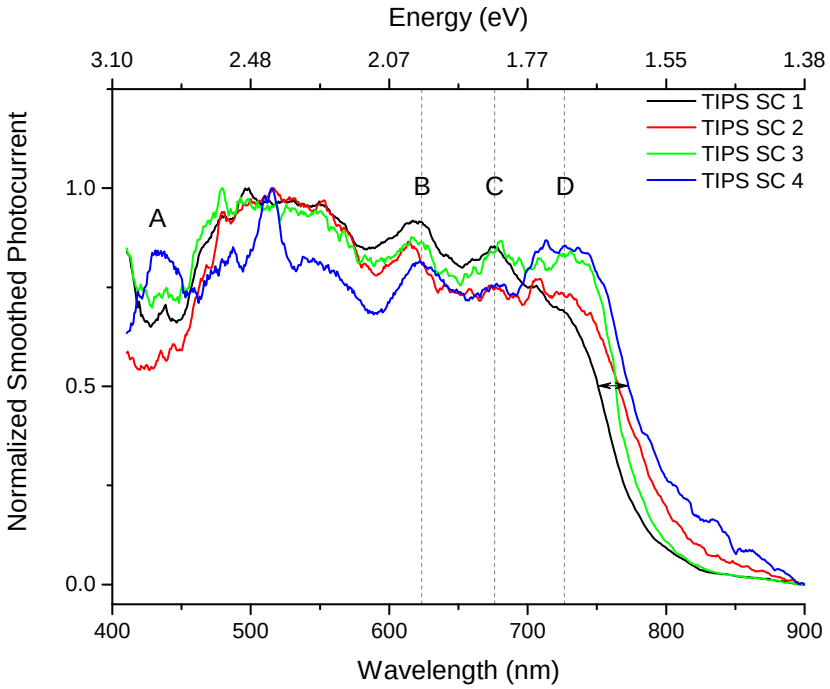

FIGURE 4.16: The PC spectra corresponding to four TIPS pentacene SC's. The PC spectra were acquired with $1.5\,\mathrm{V}$ bias and $0.8\,\mathrm{nm}$.

The PC spectra display reasonably similar curves. For wavelengths roughly shorter than $750\,\mathrm{nm}$ a good PC signal is detected that appears to decrease around $450\,\mathrm{nm}$. Peaks (B & C) can be recognized in all curves around $623.4(8)\,\mathrm{nm}$ and $676.1(8)\,\mathrm{nm}$. For crystals 1 and 2 there is a shoulder D, for crystals 3 and 4 it is rather a peak, visible around $726.6(8)\,\mathrm{nm}$. The spectral spacing between the peaks correspond to energies of $0.155\,\mathrm{eV}$ and $0.127\,\mathrm{eV}$.

A spread of approximately $\Delta 22\,\mathrm{nm} \approx \Delta 0.05\,\mathrm{eV}$ can be seen in the onset of the bandgap. It does not appear to be a redshift of the entire spectrum as the peaks at shorter wavelenth show much better agreement.

4.3.2 Photocurrent in TIPS Thin Films

The PC's of two $100\,\mathrm{nm}$ to $200\,\mathrm{nm}$ thin film were measured with a $0.8\,\mathrm{nm}$ resolution using a $9.9(0)\,\mathrm{M\Omega}$ shunt resistance. This is in contrast to the SC and IP samples that allowed direct measurement of the current (see page 27). The resulting spectra are shown in fig. 4.17, ranging from $410\,\mathrm{nm}$ to $850\,\mathrm{nm}$.

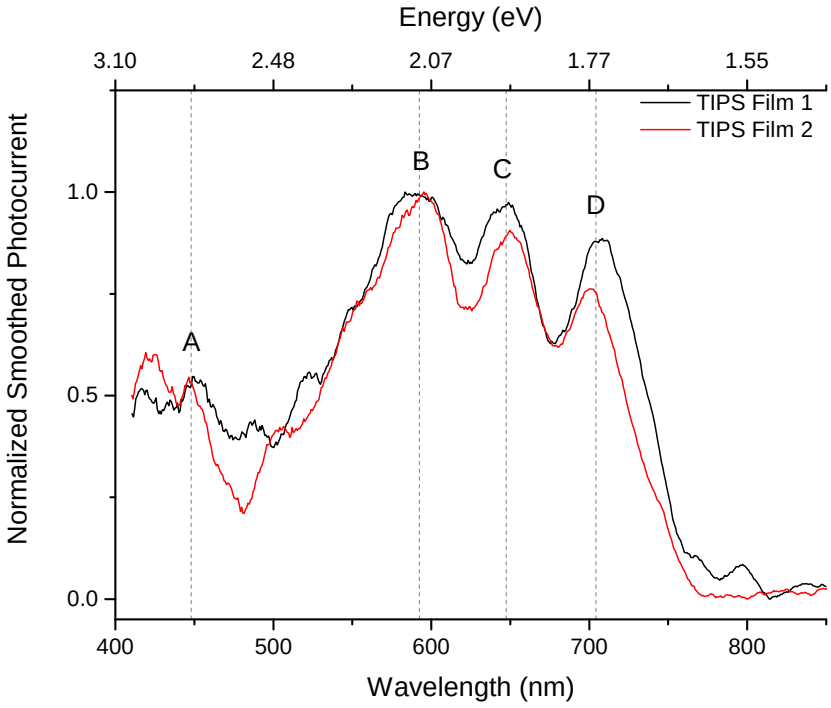

FIGURE 4.17: The PC spectra corresponding to two TIPS pentacene thin films. The PC was measured with a $9.9\,\mathrm{M\Omega}$ shunt resistance. The PC spectra were acquired with $1.5\,\mathrm{V}$ bias and $0.8\,\mathrm{nm}$.

The thin film PC spectra display more noise that was partly smoothed with the Savitzky-Golay algorithm. The graphs in fig. 4.17 show reasonable agreement for the peaks A=$448.5(8)\,\mathrm{nm}$, B=$592.5(8)\,\mathrm{nm}$, C=$646.5(8)\,\mathrm{nm}$ and D=$703.5(8)\,\mathrm{nm}$. The separations between peaks B, C & D expressed in energy are $0.175\,\mathrm{eV}$ and $0.155\,\mathrm{eV}$. The features left of peak A are believed to be artifacts due to normalization and the low raw PC signal for those short wavelengths.

4.3.3 Photocurrent in TIPS Printed Crystals

In fig. 4.18 the PC results are combined for 5 similar printed crystals. The IP crystals had thicknesses ranging from $10\,\mu m$ to $20\,\mu m$. The signal was measured directly as a current at a $1.5\,V$ bias between the pre-fabricated interdigited electrodes (see section 3.2.1). Consequently there is no specific direction along which the PC has been measured. The spectra were measured for the same range as the single crystals and thin films, $410\,nm$ to $900\,nm$, with a resolution of $0.8\,nm$.

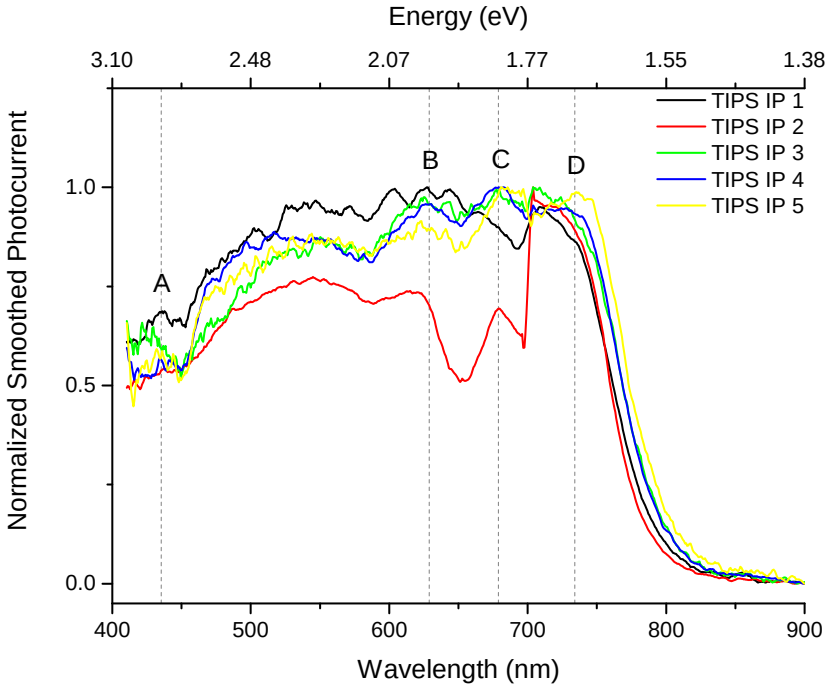

FIGURE 4.18: The PC spectra corresponding to five TIPS pentacene inkjet-printed crystals. The PC spectra were acquired with $1.5\,V$ bias and $0.8\,nm$.

The IP crystal PC spectra display a similar spectral dependence. The PC is clearly present for wavelengths shorter than $750\,nm$. For wavelengths even shorter than $450\,nm$ the signal decreases slightly in a similar fashion as the SC.

Most notably from fig. 4.18 is the large discontinuity in the TIPS IP 2 (red) PC spectrum. It is believed to result from the grating change causing a change in polarization of the incident light, which is further addressed in chapter 5. Note that the spectral features still coincide with those of the other samples.

The spectra of samples 2 to 5 show peaks around A=$435.4(8)\,nm$, B=$628.9(8)\,nm$, C=$678.8(8)\,nm$ and D=$734.0(8)\,nm$. The separations between peaks B, C & D expressed in energy are $0.145\,eV$ and $0.137\,eV$.

The PC spectrum of sample TIPS IP 1 (black) presents an anti-correlated behavior for peaks C & D. However, peak A and the onset of the bandgap are in good agreement with the other samples.

4.3.4 TIPS Morphology Comparison

In fig. 4.19 the PC spectra are compared of a single crystal (green) an inkjet printed sample (blue) and a thin film (red). The graphs correspond to the SC sample (TIPS SC 3), IP sample (TIPS IP 4) and thin film (TIPS Film 2). These samples have been selected as representative cases as their PC spectra display good average values compared to the other samples of the same morphology. Furthermore they showed a relatively high PC signal and low noise.

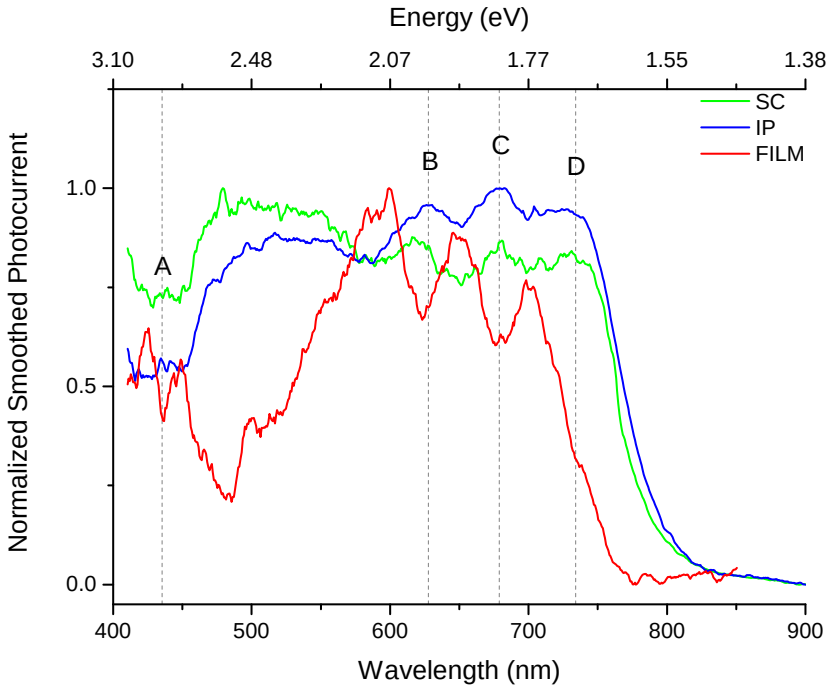

FIGURE 4.19: A comparison between the studied TIPS pentacene morphologies: SC, thin film and IP crystals. The PC spectra correspond to TIPS SC 3, TIPS Film 2 and TIPS IP 4 from respectively figs. 4.16 to 4.18. The PC spectra were acquired with $1.5\,\mathrm{V}$ bias and $0.8\,\mathrm{nm}$.

The impact of morphology is directly apparent from fig. 4.19. The thin film sample has a very distinct spectrum, but the SC and IP sample display a much more similar behavior. First of all, there is a very good agreement in the onset of the SC and IP bandgap. Secondly, their peaks labeled with B, C & D are centered at similar wavelengths. And thirdly, a similar sharp decrease in the PC response can be seen for wavelengths roughly shorter than $475\,\mathrm{nm}$.

A distinction in the SC and IP spectra can be made for wavelengths shorter or longer than circa $600\,\mathrm{nm}$. For wavelengths shorter than $600\,\mathrm{nm}$ the SC sample has a higher PC than the IP sample, whereas the opposite holds for wavelengths between $600\,\mathrm{nm}$ and the bandgap.

The thin film spectrum is different from the spectra belonging to the more bulky samples. The three main peaks and inter-spaced minima seem to anti-correlate with the SC and IP samples. Also the bandgap is blueshifted with respect to the SC and IP bandgaps. Lastly, also a decrease in the PC signal is seen for shorter wavelengths, but it is found around $550\,\mathrm{nm}$, resulting in a much narrower spectral range for which the thin film has an efficient PC response.

4.4 TIPG

The normalized PC spectrum belonging to the TIPG is presented in fig. 4.20. In the same figure the spectrum of a TIPS sample (TIPS Film 2) with comparable morphology is shown. The TIPG spectrum was measured from $410\,\mathrm{nm}$ to $850\,\mathrm{nm}$ with a $3.3\,\mathrm{nm}$ resolution. The coarser resolution, due to larger slit widths, was necessary as a result of the relatively low PC signal in the TIPG sample. The other circumstances were equivalent to the measurements on TIPS samples: it was mounted on interdigitated electrodes with a $1.5\,\mathrm{V}$ bias over the sample, a $9.9(0)\,\mathrm{M\Omega}$ shunt resistance was used to measure the signal and a $31\,\mathrm{Hz}$ modulation was applied to the incident light.

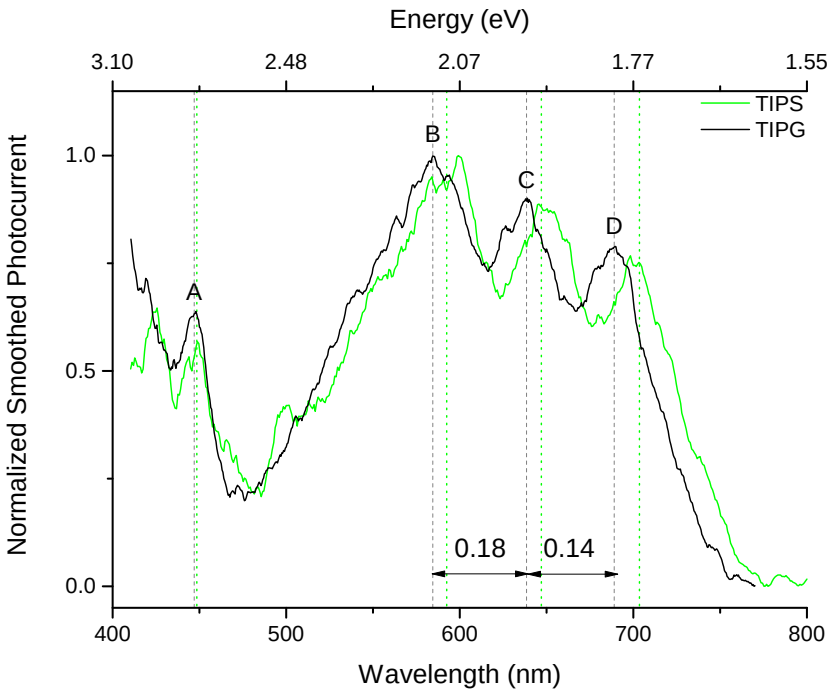

FIGURE 4.20: A PC spectrum comparison between TIPG pentacene and TIPS pentacene thin films. The selected TIPS sample is TIPS Film 2 from fig. 4.17. The PC spectra were acquired with $1.5\,\mathrm{V}$ bias and $0.8\,\mathrm{nm}$

The TIPG spectrum displays a similar spectral dependency as the TIPS sample. Comparable to TIPS, peaks are seen in the TIPG PC response at A=$447.0(8)\,\mathrm{nm}$, B=$584.5(8)\,\mathrm{nm}$, C=$638.5(8)\,\mathrm{nm}$ and D=$689.0(8)\,\mathrm{nm}$. In table 4.3 a quantitative comparison has been made between the TIPG and TIPS peaks. From table 4.3 can be concluded that within the margin of error the peak A in the TIPG spectrum coincides with TIPS. The other TIPG peaks B, C, D along with the bandgap are blueshifted an average of $\Delta 8(3)\,\mathrm{nm}$, corresponding to $\Delta 0.03(9)\,\mathrm{eV}$.

TABLE 4.3: Energy values corresponding to the TIPG and TIPS spectrum peaks in fig. 4.20. The bottom row contains the difference in energy per peak. The Davydov splitting values are shown at the right side of the table. The uncertainty in the energy values is $\pm 0.01\,\mathrm{eV}$.

	A	B	C	D	ΔE_{D1}	ΔE_{D2}
TIPG	2.77	2.12	1.94	1.80	0.18	0.16
TIPS	2.77	2.09	1.92	1.76	0.18	0.14
ΔE	0.01	0.03	0.02	0.04		

4.5 Experimental Error

The uncertainty in the experimental data is partly due to a systematic error in the measurement and partly statistical of nature. The following sections address first the systematic margin of error in the experimental setup and afterward the statistical uncertainty of the reported results.

4.5.1 Systematic Error

The acquired spectral data has an intrinsic margin of error due to the bandpass and resulting resolution of the involved instruments (see section 2.2.1.2). The monochromator has been calibrated for optimal precision but a systematic error persists. The spectral margin of error depends on the grating's dispersion, the slit widths and the mechanical precision and reproducibility.

The monochromator (as described in section 3.1.2.1) has a reciprocal linear dispersion of $3.3\,\mathrm{nm\,mm^{-1}}$[62] . From eq. 2.10, with the smallest possible slit widths of $10.0(5)\,\mu$ the (theoretical) best resolution is $33(17) \times 10^{-3}\,\mathrm{nm}$.

The mechanical accuracy of the stepper motor that rotates the grating limits the precision with which the diffraction angle can be set. The mechanical accuracy according to the manufacturer is $\pm 0.2\,\mathrm{nm}$[64].

The calibration of the monochromator (section 4.1.1) showed an average deviation in the measurement results of $0.02(122)\,\mathrm{nm}$. Furthermore an average FWHM value of $0.95(45)\,\mathrm{nm}$ was found for the peaks in the calibration spectrum.

4.5.2 Statistical Error

In section 3.1.4 is described how the lock-in amplifier uses an internal buffer. It allows the fast measurement and internal storage of N data points. Subsequently the average μ and standard deviation (SD) σ are calculated of the stored points (see eqs. 4.1 to 4.2). The calculation of the average is straightforward. The calculated SD is the *corrected sample* standard deviation. It corrects for the fact that the N points are a randomly taken sample. The correction entails subtracting the denominator by 1, as shown in eq. 4.2.

$$\mu = \frac{1}{N}\sum_{i=1}^{N} x_i \tag{4.1}$$

$$\sigma = \sqrt{\frac{\sum_{i=1}^{N}(x_i - \mu)^2}{N-1}} \tag{4.2}$$

Chapter 5

Discussion

Single Crystals
Both symbatic and antibatic PC spectra for rubrene SCs were presented in section 4.2.1.1. Recent studies attribute the antibatic behavior of the PC response to oxidation of the material[52]. Furthermore the oxidation is triggered by light. No oxidation occurs in the dark, even for samples kept in pure oxygen. Najafov et al. [52] showed how the depth up to which the material oxidizes is correlated with the absorption depth of the incident light. The antibatic PC results in fig. 4.6 support the importance of oxidation depth for an antibatic response. The PC spectrum is no longer antibatic for shorter wavelengths, that penetrate deeper into the material before absorption. This indicates that an antibatic PC relation to the spectral absorption is a oxidation related phenomenon that occurs up to a certain depth from the material's surface. In fact, for wavelengths roughly shorter than $450\,\mathrm{nm}$, no real antibatic nor symbatic behavior is seen, possibly indicating a crossover regime.

Thin Films
Distinct PC spectra corresponding to different electrode geometries attached to rubrene thin films were displayed in section 4.2.2.2. The results support a photocurrent generation mechanism that depends on the absorption depth of the incident wavelength. Subsequently, the photo-generated charge-carriers drift through the medium to the electrodes. Shorter wavelengths, having large penetration depth, create charge-carriers further from the top surface, but closer to the bottom placed electrodes. Consequently charge-carrier created by short wavelengths generally will have shorter distance to drift trough the bulk, decreasing the possibility of earlier recombination and increasing their likeness to contribute to the measured current.

TIPS Inkjet Printed Crystals
The PC spectra belonging to the IP TIPS samples in section 4.3.3 require some discussion. First of all the discontinuity observed in the normalized PC spectrum of sample TIPS IP 2. It occurs at $700\,\mathrm{nm}$, the wavelength at which the monochromator's gratings are changed.

It is unlikely that the discontinuity is due to the jump in optical intensity or results from a nonlinear sample response that is incorrectly normalized. The jump in optical intensity is compensated by the normalization as for the other samples. The observed nonlinear photocurrent response yields a suppression of the PC at higher intensities. As a result, a decrease is seen at the discontinuity after normalization. The sudden increase of PC at the grating change refutes nonlinearity or incorrect normalization of the photocurrent as cause for the discontinuity.

The sudden increase in PC may result from a change in the polarization of the incident light. The QTH light incident on the grating is unpolarized. Ideally the light that is diffracted of the grating is also unpolarized. For wavelengths near the blaze wavelength λ_b this holds, but according to the "2/3 - 3/2" rule (see page 15) the diffraction of longer wavelengths $> {}^{3}\!/_{2}\,\lambda_b$ results in strongly polarized light. Therefore it is safe to assume the polarization of the output light around $700\,\mathrm{nm}$ depends greatly on which grating is used. Furthermore the spectral absorption of TIPS pentacene thin films depends on the polarization of the light[66, 81]. The aforementioned indicates that the discontinuity observed in the PC spectrum of sample TIPS IP 2 results from the grating change causing a sudden change of the incident light polarization and a polarization dependent absorption in the sample. Note that the spectrum is only shifted in magnitude but no shift in the wavelength dependency is seen.

It is noteworthy this discontinuity is not seen for other TIPS pentacene samples of any morphology. Different polarization dependency of the spectral absorption for the single crystals, thin films and printed crystals is expected due to their different crystalline order. Single crystals and thin films might exhibit less polarization dependency in the spectral absorption. The apparent absent polarization dependency in other printed crystals is most likely explained by the arbitrary orientation of the samples' crystalline axes relative to the polarization direction of the light. The polarization of diffracted light is less of an issue for the rubrene spectra. The rubrene spectra cover a range from $410\,\mathrm{nm}$ to $650\,\mathrm{nm}$ and were measured with a single grating.

Chapter 6

Conclusions

In this research a new PC spectroscopy setup has been developed that enables the measurement of $I_{RMS} = 0.1\,\mathrm{pA}$ currents with an excellent spectral resolution of $0.63\,\mathrm{nm}$. The configuration that measured the PC directly, without shunt resistance, achieved results with the least noise. Evaluation of the setup's performance in reference to the commonly used organic semiconductor rubrene yielded PC spectra comparable to literature and with good reproducibility.

The measurements on rubrene SCs revealed symbatic and antibatic PC spectra relative to the spectral absorption. The antibatic behavior decreases for wavelengths with a larger absorption depth. Recent publications have shown that oxidation decreases with depth and its impact on the PC response. In combination with the results of this study there is indication that the antibatic PC spectra results from oxidation. In addition, the symbatic SC indicate that the PC through the bulk of the rubrene displays a different spectrum than the PC measured at the surface with coplanar electrodes.

The rubrene thin film spectra support the conclusion that film thickness affects the PC up to a thickness of $52\,\mathrm{nm}$. Relative to TOP placed electrodes, rubrene films show increased PC response in the $410\,\mathrm{nm}$ to $475\,\mathrm{nm}$ range for BOTTOM placed electrodes. CROSS placed electrodes show intermediate results. Therefore it is concluded that photocurrent generation depends on the photon absorption depth. The thin film results do not significantly support PC anisotropy.

The TIPS PC spectra support the conclusion that the electronic structure of inkjet-printed crystals is similar to SCs. The SCs react relatively stronger to shorter wavelengths than the IP crystals and the oposite holds for longer wavelengths. The crossover is at roughly $600\,\mathrm{nm}$.

Finally, the TIPG thin film PC spectrum's similarity with TIPS films leads to the conclusion that the Si substitution for Ge does not drastically alter the electronic structure.

Chapter 7

Outlook

In this research the initial development was completed of an experimental setup that successfully applies photocurrent spectroscopy to study organic semiconductors. During the course of this process a number of insights were acquired how this setup could be further developed or applied.

- The setup's performance may be improved by resolving the need for the shunt resistance for low impedance samples. Incorporation of a low noise current amplifier that converts the current to a voltage signal could replace the shunt resistance. Another possibility is effectively increasing the impedance of the samples by reducing the contact area of the electrodes.
- The Sciencetech 9055F is an asymmetric Czerny-Turner monochromator that has an internal magnification of 1.25. Therefore the exit slit can be operated at 1.25 times the width of the input slit without affecting the spectral resolution. However, the photon flux that is passed trough the slit is increased, increasing the optical stimulus and ultimately the photocurrent.
- The PC signal may be further increased by enlarging the spotsize of the incident light on the sample. As a result of the increased area the incident irradiance is decreased. Subsequently the total light input flux may be increased. This increases the net incident photon flux, whilst maintaining a low irradiance to avoid a PC response.
- The polarization of the diffracted light that is put out by the monochromator currently is uncontrolled. This research indicates the impact of the incident light polarization on the PC. Making use of a polarizer in the beampath after the monochromator provides controlled polarization for future measurements.

Based on the results in this research a range of followup experiments may be of interest. The current setup, or with minor adjustments, could be applied toward these measurements.

- With the aforementioned polarizer a study could easily be conducted on the impact of the incident light's polarization on the PC response.
- Another interesting possible continuance is presented by the indicated PC dependency on the presence of oxidation and the oxidation depth dependency to exposing light's wavelength. Further exploration of this phenomenon by studying samples that were prior exposed to monochromatic light, would be very interesting.

Acknowledgements

First of all, I would like to thank everyone from the Organic Semiconductor and Devices research group at the University of Bologna for receiving me this last year. I thank professor dr. Beatrice Fraboni for offering me the possibility to collaborate within the research group, her help with the bureaucracy associated with this internal endeavor and for the supervision throughout the year.

Also I thank the post-docs dr. Laura Basiricò, dr. Tobias Cramer, dr. Isacco Gualandi, dr. Martina Perani and dr. Marta Tessarolo for the great amount of shared advice for the research and everyday life in a new country. A special thanks to dr. Andrea Ciavatti who worked with me on a daily basis and who's help was of great importance throughout this research.

Next I would like to say thank you to the PhD students Maria Antonietta Fazio, Marco Marzocchi, Marco Calizzi and Giacomo Rossi and master students Dario Cavedale, Francesco Decataldo and Margherita Sola for the times and talks spent together in the lab or during lunch this past year.

Also I would like to express my gratitude to my examiners professor dr. Thomas Peitzmann and dr. Dries van Oosten for enabling me to conduct this very interesting research and experience in general, notwithstanding the added bureaucratic difficulties associated with this international collaboration.

I am grateful to my friends and family who have supported me during this research with their interest and their visits abroad. Thanks to my brother Ewout van der Feltz for his feedback from a chemist's point of view. Particularly I am indebted to my parents who's support during this past year underlines once more their invaluable support throughout my entire education.

Lastly, I would like to acknowledge the Erasmus+ program and i-FLEXIS program for the funding that made this research possible.

List of Figures

2.1 . . . 5
2.1a Kekulé representation of benzene . . . 5
2.1b Carbon energy level diagram . . . 5
2.1c Degeneracy decrease for increasing number of atoms . . . 5
2.2 . . . 10
2.2a Kekulé representation of rubrene . . . 10
2.2b Kekulé representation of TIPS pentacene . . . 10
2.2c Kekulé representation of TIPS pentacene . . . 10
2.3 Rubrene endoperoxide . . . 10
2.4 . . . 11
2.4a Herringbone packing . . . 11
2.4b Brickwall packing . . . 11
2.5 Jablonski diagram of electronic transitions commonly found for organic semiconductors . . . 12
2.6 Symmetric Czerny-Turner monochromator configuration . . . 14
2.7 The projected solid angle on a sphere. . . . 17
2.8 . . . 18
2.8a Photodiode p-n junction . . . 18
2.8b Mode of operation of a pyroelectric detector . . . 18

3.1 Schematic overview of the experimental setup . . . 20
3.2 Condenser-focusing lens system . . . 21
3.3 Internal Czerny-Turner geometry of the Sciencetech 9055F monochromator . . . 22
3.4 The electrical circuit connected to the sample . . . 23
3.5 Internal noise density distribition over the frequency spectrum . . . 24
3.6 SR830 Lock-in Amplifier functional block diagram . . . 25
3.7 Frequencies of the modulation, signal and lock-in amplifier . . . 26
3.8 Schematic representation of the dynamic reserve . . . 27
3.9 . . . 29
3.9a Rubrene Single Crystal . . . 29
3.9b TIPS Pentacene Single Crystal . . . 29
3.9c TIPS Inkjet-Printed Crystal . . . 29
3.9d Rubrene Thin Film . . . 29
3.9e TIPS Pentacene Thin Film . . . 29
3.9f TIPG Thin Film . . . 29
3.10 . . . 30
3.10a Pre-fabricated, interdigitated eletrodes on PET substrate . . . 30
3.10b Custom electrodes placed along the semiconductor's surface crystallographic axes . . . 30
3.11 Custom electrodes geometries . . . 30
3.11a Custom eletrodes in TOP configuration . . . 30
3.11b Custom eletrodes in BOTTOM configuration . . . 30
3.11c Custom eletrodes in CROSS configuration . . . 30

4.1 Measured Hg emission spectrum . . . 31
4.2 Measured Hg emission line deviations . . . 32
4.3 . . . 33
4.3a Photon irradiance as a function of input slit width . . . 33

4.3b Photon irradiance as a function of lamp operating power . . . 33
4.4 Spectra due to the grating change and Savitzky-Golay smoothing . . . 34
4.5 Noise measurements with a shunt resistance and of the electrical current. . . . 35
4.6 Symbatic and Antibatic PC spectra of rubrene SC's . . . 36
4.7 Rubrene SC with perpendicular electrodes in TOP geometry . . . 37
4.8 Rubrene SC in TOP, BOTTOM and CROSS geometry . . . 38
4.9 Perpendicular electrodes on rubrene thin films per thickness . . . 39
4.10 . . . 40
4.10a PC along the α axis in rubrene $13\,\mathrm{nm}$, $52\,\mathrm{nm}$ and $101\,\mathrm{nm}$ thin films . . . 40
4.10b PC along the β axis in rubrene $13\,\mathrm{nm}$, $52\,\mathrm{nm}$ and $101\,\mathrm{nm}$ thin films . . . 40
4.11 PC rubrene thin films with TOP, BOTTOM and CROSS electrode geometries . . . 41
4.12 Comparison rubrene SC and thin films along the α axis with TOP electrodes . . . 42
4.13 Comparison rubrene SC and thin films along the β axis with TOP electrodes . . . 42
4.14 Comparison rubrene SC and thin film with BOTTOM placed electrodes . . . 43
4.15 Comparison rubrene SC and thin film with CROSS placed electrodes . . . 43
4.16 PC spectra of TIPS pentacene SC's . . . 44
4.17 PC spectra of TIPS pentacene thin films . . . 45
4.18 PC spectra of TIPS pentacene IP crystals . . . 46
4.19 PC spectra comparison between TIPS pentacene SC, thin film and IP crystals . . . 47
4.20 PC spectra comparison between TIPG pentacene and TIPS pentacene . . . 48

A.1 . . . 58
A.1a 3D model image of the optics in the setup. . . . 58
A.1b Schematic overview of the optics in the setup. . . . 58

B.1 Photodiode spectral responsivity. . . . 59
B.2 . . . 60
B.2a Photodiode response as a function of modulation frequency. . . . 60
B.2b Pyroelectric detector response as a function of modulation frequency. . . . 60
B.3 Detector area relative to slit area . . . 60

C.1 . . . 61
C.1a Study of the internal measurement routine in the SR830 lock-in amplifier. The red curve shows the results from the MAD routine. The black curve is averaged RMS signal that is normally measured. . . . 61
C.1b Change in noise distribution depending on included setup components. Johnson noise becomes more important when more parts of the setup are included. . . . 61
C.2 . . . 62
C.2a Comparison of grounded or floating input connection. . . . 62
C.2b Comparison of single-ended or differential voltage input connection. . . . 62

List of Tables

2.1 Material properties of the inorganic semiconductor amorphous Silicon and organic semiconductors Rubrene and Pentacene 9

3.1 Overview of frequency bandwidth and associated necessary minimal waiting time for different time constants and filterslopes. 26
3.2 Sample materials and morphologies 29

4.1 Monochromator broadening of emission lines. 32
4.2 Energy values corresponding to the spectrum peaks in fig. 4.6. Added to the right are the differences in energy between adjacent peaks known as Davydov splitting. The uncertainty in the energy values is $\pm 0.001\,\mathrm{eV}$. 37
4.3 Energy values corresponding to the TIPG and TIPS spectrum peaks in fig. 4.20. The bottom row contains the difference in energy per peak. The Davydov splitting values are shown at the right side of the table. The uncertainty in the energy values is $\pm 0.01\,\mathrm{eV}$. 48

A.1 Etendue 58

Appendix A

Etendue

The geometric etendue has been calculated for the optical components in the setup. A threedimensional model was built with Google Sketchup for optimization of the etendue. A zoomed in selection of the optics is shown in fig. A.1a. Figure B.3 gives a schematic overview of the setup.

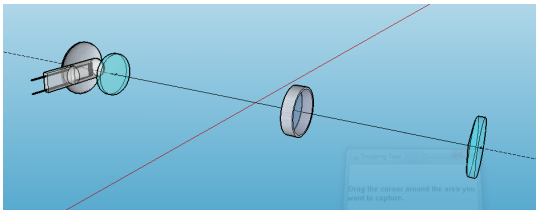

A.1 (A) 3D model image of the optics in the setup.

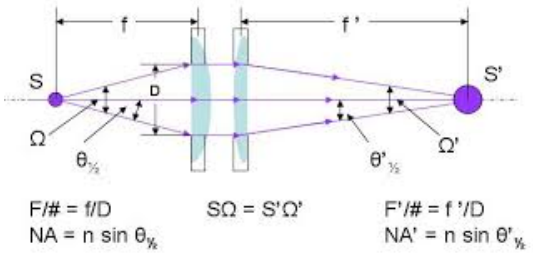

A.1 (B) Schematic overview of the optics in the setup.

Table A.1 shows the etendue values that were calculated with eq. 2.12 for the QTH lamp optics illustrated in fig. A.1a and the etendue corresponding to either slit of the monochromator. The output slit limits the light throughput of the system with a etendue of $277\,659 \times 10^{-3}\,\mathrm{mm^2\,sr}$.

TABLE A.1: Etendue

	Etendue [$\mathrm{mm^2\,sr}$]
Lamp	37.3511
Input Slit	0.535 87
Output Slit	0.277 659

Appendix B

Detector Specifics

Photodiode Responsivity

Figure B.1 shows the spectral response of the photodiode. From fig. B.1 the peak of the photodiode's responsivity was extracted as adressed in chapter 4.

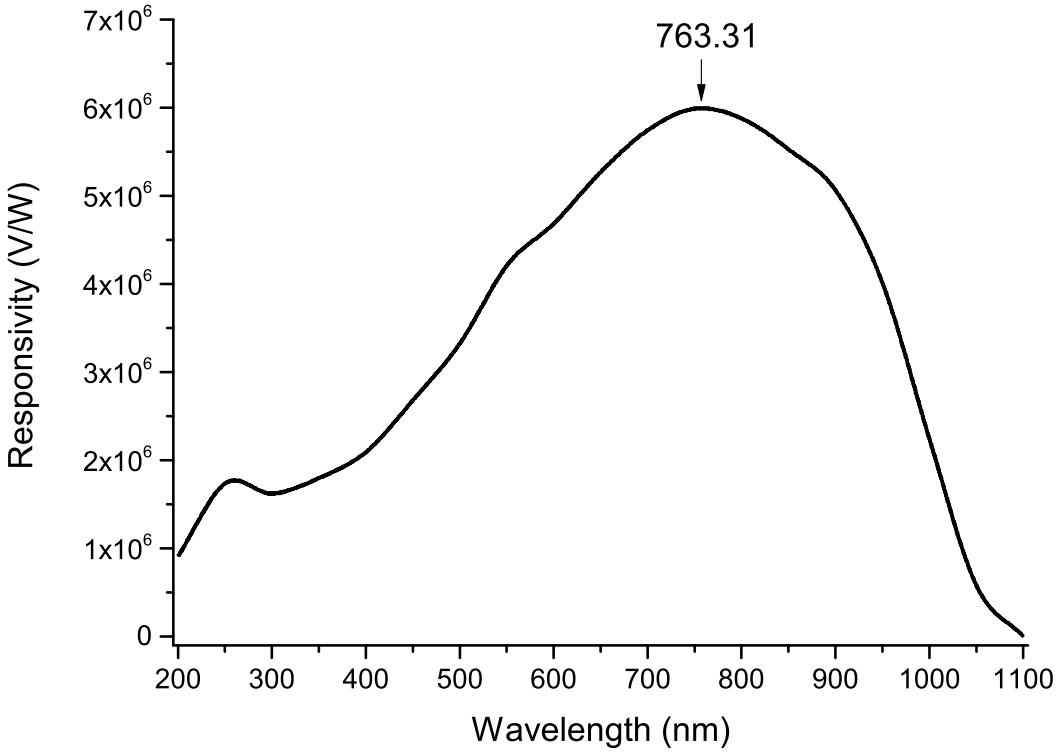

FIGURE B.1: Photodiode spectral responsivity.

Detector Modulation Frequency Dependence

Figures B.2b and B.2b show respectively the photodiode's and pyroelectric detector's dependencies on the modulation frequency of the input signal. In the inset the dependency for low frequencies is shown.

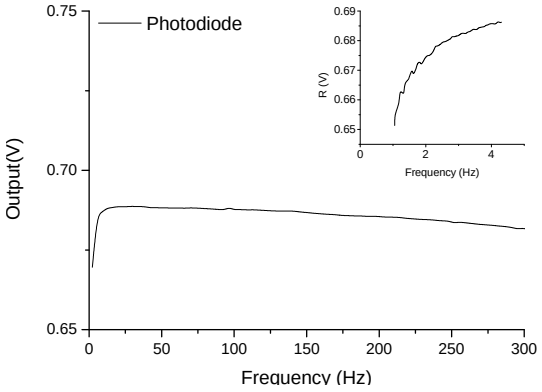

B.2 (A) Photodiode response as a function of modulation frequency.

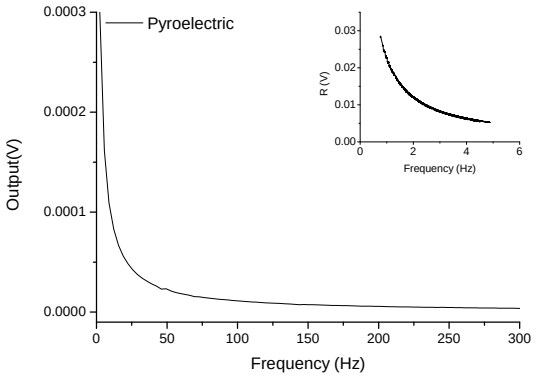

B.2 (B) Pyroelectric detector response as a function of modulation frequency.

Slit geometry

The photodiode and the pyroelectic both have circular active areas with respectively 2.5 mm and 1 mm diameter. However the photodiode is much more sensitive. Therefore it had to be vignetted to allow large enough slit widths for to have a clear signal with the pyroelectric but without overloading the photodiode. This is illustrated by fig. B.3 and the resulting effective area can be calculated with eq. B.1.

$$A_{eff} = \frac{2dR}{\sqrt{1+\frac{d}{2R}^2}} + R^2(2\arctan(\frac{d}{2R}) - \sin(2\arctan(\frac{d}{2R}))) \tag{B.1}$$

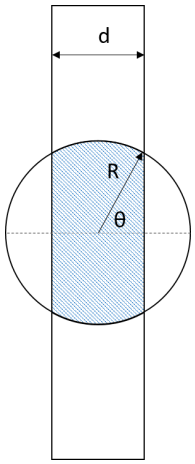

FIGURE B.3: Detector area relative to slit area

Appendix C

Noise

This appendix contains supporting information and figures to the noise measurement in section 4.1.4

The SR830 has an internal noise measurement function that calculates the noise based on the MAD method. It calculates the deviation of the signal compared to a moving average of the previously measured signal. Next it takes the moving average of this deviation. Figure C.1a shows the results from this routine compared to the regular measurement of the signal. The MAD results present a more stable indication of the noise.

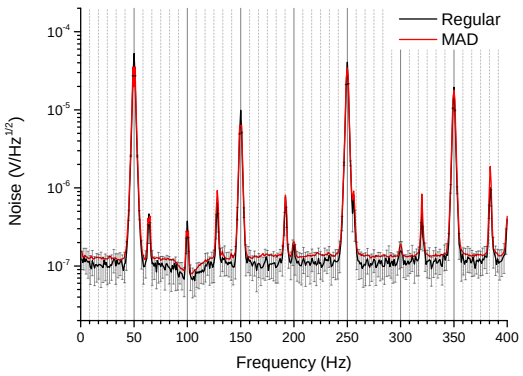

C.1 (A) Study of the internal measurement routine in the SR830 lock-in amplifier. The red curve shows the results from the MAD routine. The black curve is averaged RMS signal that is normally measured.

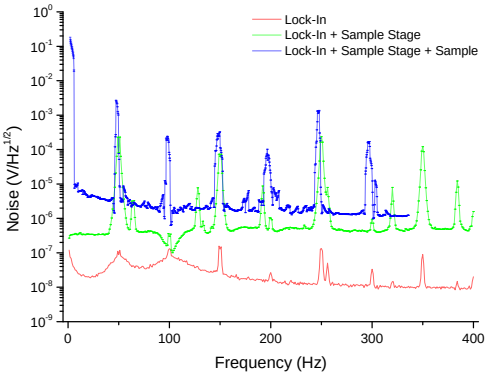

C.1 (B) Change in noise distribution depending on included setup components. Johnson noise becomes more important when more parts of the setup are included.

Figure C.1b illustrates the frequency distributions of the noise. The different curves represent various measurements each including more components of the complete experimental setup. As expected, the measured noise increases as more components are included in the setup. The distribution of the noise over the frequency spectrum also changes.

A comparison for floating or grounded input connection on the lock-in amplifier yielded the results shown in fig. C.2a. The difference is very small, but slightly better results are obtained with the grounded input configuration.

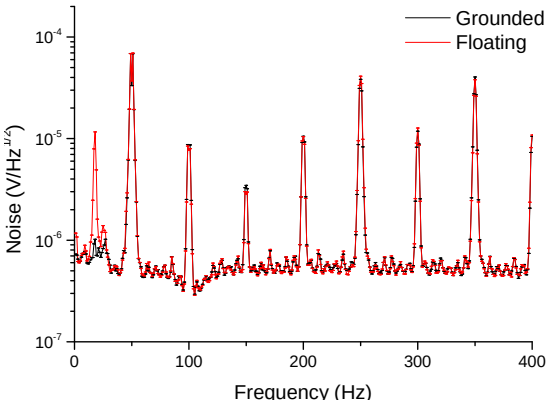

C.2 (A) Comparison of grounded or floating input connection.

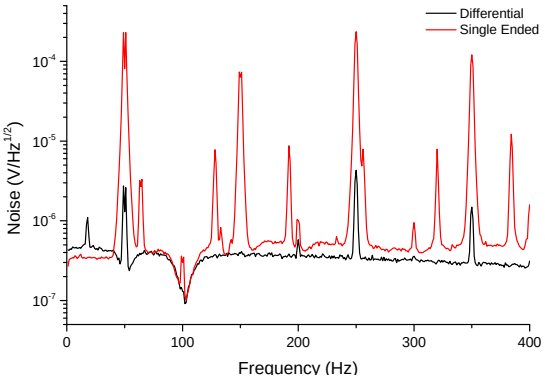

C.2 (B) Comparison of single-ended or differential voltage input connection.

A comparison between the two voltage input connection modes: single-ended or differntial led to the results shown in fig. C.2b. The differential voltage input configuration offers superior results in terms of noise.

Bibliography

[1] *10LWF-400-B Long-Wave Pass Filter Tech Specs*. 10LWF-400-B. Newport Inc., Feb. 2009.

[2] *2-Color Photodiode/Receiver*. http://www.eosystems.com/. Electro - Optical Systems Inc. 1039 West Bridge St, Phoenixville, PA 19460, Nov. 2015.

[3] Nikos Arvanitidis. "Chair of the EGS Mineral Resources Expert Group Nikolaos Arvanitidis talks to SETIS". In: *SETIS* (2015).

[4] AzoOptics. *Lighting a Monochromator*. English. Mar. 2014. URL: http://www.azooptics.com/Article.aspx?ArticleID=835.

[5] Laura Basiricò. "Inkjet printing of organic transistor devices". PhD thesis. 2012.

[6] Satria Zulkarnaen Bisri et al. "Electron transport in rubrene single-crystal transistors". In: *Applied Physics Letters* 96.18, 183304 (2010). DOI: 10.1063/1.3419899.

[7] D. Braga et al. "Bulk electrical properties of rubrene single crystals: Measurements and analysis". In: *Phys. Rev. B* 77 (11 Mar. 2008), p. 115205. DOI: 10.1103/PhysRevB.77.115205.

[8] Alejandro L Briseno et al. "High-performance organic single-crystal transistors on flexible substrates". In: *Advanced Materials* 18.17 (2006), pp. 2320–2324.

[9] R.H. Bube. *Photoconductivity of solids*. Wiley, 1960.

[10] R.H. Bube. *Photoelectronic Properties of Semiconductors*. Cambridge University Press, 1992.

[11] VY Butko et al. "Field-effect transistor on pentacene single crystal". In: *Applied physics letters* 83.23 (2003), pp. 4773–4775.

[12] *Characteristics and use of infrared detectors*. Technical Information SD-12. 1126-1 Ichino-cho, Hamamatsu City, 435-8558 Japan: Hamamatsu, July 2016.

[13] Chung Chieh. *Bond Lengths and Energies*. July 2016. URL: http://www.science.uwaterloo.ca/~cchieh/cact/c120/bondel.html.

[14] Andrea Ciavatti. "Transport Properties and Novel Sensing Applications of Organic Semiconducting Crystals". PhD thesis. Università di Bologna, 2013/2014.

[15] Ying Diao et al. "Solution coating of large-area organic semiconductor thin films with aligned single-crystalline domains". In: *Nature materials* 12.7 (2013), pp. 665–671.

[16] Yvonne Dienes et al. "Phosphorus-Based Heteropentacenes: Efficiently Tunable Materials for Organic n-Type Semiconductors". In: *Chemistry–A European Journal* 14.32 (2008), pp. 9878–9889.

[17] Christos D Dimitrakopoulos and Patrick RL Malenfant. "Organic thin film transistors for large area electronics". In: *Advanced Materials* 14.2 (2002), pp. 99–117.

[18] Christos D Dimitrakopoulos and Debra J Mascaro. "Organic thin-film transistors: A review of recent advances". In: *IBM Journal of Research and Development* 45.1 (2001), pp. 11–27.

[19] Instruments S.A. Jobin Yvon/Spex Division. *Guide for Spectroscopy*. Instruments S.A., Jobin Yvon/Spex Division, 1994.

[20] RG Endres et al. "Structural and electronic properties of pentacene molecule and molecular pentacene solid". In: *Computational materials science* 29.3 (2004), pp. 362–370.

[21] Tadesse Haile Fereja, Ariaya Hymete, and Thirumurugan Gunasekaran. "A recent review on chemiluminescence reaction, principle and application on pharmaceutical analysis". In: *ISRN Spectroscopy* 2013 (2013).

[22] B Fraboni et al. “Spectroscopic investigation of the semiconductor molecular packing in fully operational organic thin-film transistors”. In: *Applied Physics Letters* 96.16 (2010), p. 163302.

[23] Beatrice Fraboni. *i-FLEXIS Website*. English. Aug. 2017. URL: http://www.iflexis.eu/.

[24] Beatrice Fraboni et al. “Organic Semiconducting Single Crystals as Next Generation of Low-Cost, Room-Temperature Electrical X-ray Detectors”. In: *Advanced Materials* 24.17 (2012), pp. 2289–2293.

[25] Beatrice Fraboni et al. “Organic semiconducting single crystals as solid-state sensors for ionizing radiation”. In: *Faraday discussions* 174 (2014), pp. 219–234.

[26] *Getting Light into a Monochromator*. Newport Corporation. Mar. 2016. URL: http://www.newport.com/Getting-Light-into-a-Monochromator/383722/1033/content.aspx.

[27] C Goldmann et al. “Hole mobility in organic single crystals measured by a “flip-crystal" field-effect technique”. In: *Journal of Applied Physics* 96.4 (2004), pp. 2080–2086.

[28] S Gorgolis et al. “Impact of pentacene film thickness on the photoresponse spectra: Determination of the photocarrier generation mechanism”. In: *Journal of Applied Physics* 112.1 (2012), p. 013101.

[29] Peter A Gorry. “General least-squares smoothing and differentiation by the convolution (Savitzky-Golay) method”. In: *Analytical Chemistry* 62.6 (1990), pp. 570–573.

[30] David J Gundlach et al. “Pentacene organic thin-film transistors-molecular ordering and mobility”. In: *IEEE Electron Device Letters* 18.3 (1997), pp. 87–89.

[31] OB Gusev et al. “Lifetime of excitons localized in Si nanocrystals in amorphous silicon”. In: *Semiconductors* 50.5 (2016), pp. 627–631.

[32] *HALOSTAR 24 V 150 W 24 V GY6.35 Lamp Supplement*. http://www.osram.com/. OSRAM GmbH. Marcel-Breuer-Strasse 6, 80807 Munich, Germany, Mar. 2016.

[33] James R Heath and Mark A Ratner. “Molecular electronics”. In: (2003).

[34] S. Hooker and C. Webb. *Laser Physics*. Oxford Master Series in Physics. OUP Oxford, 2010.

[35] Gilles Horowitz et al. “Organic field-effect transistors”. In: *Advanced Materials* 10.5 (1998), pp. 365–377.

[36] *http://physics.nist.gov/PhysRefData/Handbook/Tables/mercurytable2.htm*. URL: http://physics.nist.gov/PhysRefData/Handbook/Tables/mercurytable2.htm.

[37] Liwei Huang et al. “Rubrene micro-crystals from solution routes: their crystallography, morphology and optical properties”. In: *J. Mater. Chem.* 20 (1 2010), pp. 159–166. DOI: 10.1039/B914334C.

[38] P Irkhin, H Najafov, and V Podzorov. “Steady-state photoconductivity and multi-particle interactions in high-mobility organic semiconductors”. In: *Scientific reports* 5 (2015).

[39] Kibum Kim et al. “Optical properties of solid pentacene”. In: *Journal of superconductivity* 15.6 (2002), pp. 595–598.

[40] Hagen Klauk et al. “Pentacene organic thin-film transistors for circuit and display applications”. In: *IEEE Transactions on Electron Devices* 46.6 (1999), pp. 1258–1263.

[41] M Kytka et al. “Real-time observation of oxidation and photo-oxidation of rubrene thin films by spectroscopic ellipsometry”. In: *arXiv preprint cond-mat/0703522* (2007).

[42] Jeremy M Lerner. “Imaging spectrometer fundamentals for researchers in the biosciencesâ€”a tutorial”. In: *Cytometry Part A* 69.8 (2006), pp. 712–734.

[43] Feng Li et al. “Electrical and optical characteristics of red organic light-emitting diodes doped with two guest dyes”. In: *Synthetic metals* 139.2 (2003), pp. 341–346.

[44] *Light Collection and Systems Throughput*. Newport Corporation. Mar. 2016. URL: http://www.newport.com/Getting-Light-into-a-Monochromator/383722/1033/content.aspx.

[45] Meena Devi Lysko. "Measurement and Models of Solar Irradiance". PhD thesis. 2006.

[46] George Malliaras and Richard Friend. "An organic electronics primer". In: *Physics Today* 58.5 (2005), pp. 53–58.

[47] Christine Corinne Mattheus. "Polymorphism and electronic properties of pentacene". In: *Links* 13 (2015), p. 07.

[48] Mike L Meade. *Lock-in amplifiers: principles and applications*. 1. Mike Meade, 1983.

[49] Oleksandr Viktorovich Mikhnenko. "Dynamics of Singlet and Triplet Excitons in Organic Semiconductors". PhD thesis. University of Groningen, 2012.

[50] H Mohammadi and E Eslami. "Investigation of spectral resolution in a Czerny Turner spectrograph". In: *Instruments and Experimental Techniques* 53.4 (2010), pp. 549–552.

[51] H Najafov et al. "Observation of long-range exciton diffusion in highly ordered organic semiconductors". In: *Nature materials* 9.11 (2010), pp. 938–943.

[52] Hikmet Najafov et al. "Photon-Assisted Oxygen Diffusion and Oxygen-Related Traps in Organic Semiconductors". In: *Advanced Materials* 23.8 (2011), pp. 981–985. DOI: 10.1002/adma.201004239.

[53] SP Park et al. "Optical and luminescence characteristics of thermally evaporated pentacene films on Si". In: *Applied physics letters* 80.16 (2002), pp. 2872–2874.

[54] V Podzorov et al. "Intrinsic charge transport on the surface of organic semiconductors". In: *Physical review letters* 93.8 (2004), p. 086602.

[55] Vitaly Podzorov. "Organic single crystals: Addressing the fundamentals of organic electronics". In: *MRS bulletin* 38.01 (2013), pp. 15–24.

[56] Martin Pope and Charles E Swenberg. *Electronic processes in organic crystals and polymers*. Oxford University Press on Demand, 1999.

[57] *Pyroelectric detector P2613 series*. http://www.datasheetarchive.com/dlmain/Datasheets-28/DSA-543303.pdf. Hamamatsu Corp. 1126-1 Ichino-cho, Hamamatsu City, 435-8558 Japan, July 2016.

[58] Transparency Market Research, ed. *GaN Semiconductor Devices Market (Power semiconductors, Opto semiconductors) - Global Industry Analysis, Size, Share, Growth, Trends and Forecast 2013 - 2019*. Market Report. Transparency Market Research. 2014. URL: http://www.transparencymarketresearch.com/gallium-nitride.html.

[59] Marcos A Reyes-Martinez, Alfred J Crosby, and Alejandro L Briseno. "Rubrene crystal field-effect mobility modulation via conducting channel wrinkling". In: *Nature communications* 6 (2015).

[60] Abraham Savitzky and Marcel JE Golay. "Smoothing and differentiation of data by simplified least squares procedures." In: *Analytical chemistry* 36.8 (1964), pp. 1627–1639.

[61] Markus Schwoerer and Hans Christoph Wolf. *Organic molecular solids*. John Wiley & Sons, 2007.

[62] *Sciencetech 9055-9055F Monochromator Manual*. Sciencetech Inc. 1450 Global Drive, London, Ontario, Canada, Mar. 2016.

[63] *Sciencetech Light Sources Brochure*. http://www.sciencetech-inc.com/. Sciencetech Inc. 1450 Global Drive, London, Ontario, Canada, Mar. 2016.

[64] *Sciencetech Monochromators & Spectrographs Brochure*. http://www.sciencetech-inc.com/. Sciencetech Inc. 1450 Global Drive, London, Ontario, Canada, June 2016.

[65] *Sciencetech Standard Series Monochromators*. http://www.sciencetech-inc.com/. Sciencetech Inc. 1450 Global Drive, London, Ontario, Canada, Mar. 2016.

[66] Sahar Sharifzadeh et al. "Relating the Physical Structure and Optoelectronic Function of Crystalline TIPS-Pentacene". In: *Advanced Functional Materials* 25 (2015), pp. 2038–2046. DOI: 10.1002/adfm.201403005.

[67] Sigma-Aldrich. *Homepage*. Ed. by Sigma-Aldrich Co. LLC. 2016. URL: http://www.sigmaaldrich.com/.

[68] Henning Sirringhaus and Tatsuya Shimoda. "Inkjet printing of functional materials". In: *MRS bulletin* 28.11 (2003), pp. 802–806.

[69] *SR830 User's Manual*. Revision 2.5. Stanford Research Systems, Inc. 1290-D Reamwood Avenue, Sunnyvale , California 94089, United States, 2011.

[70] P.P. Stallinga. *Electrical Characterization of Organic Electronic Materials and Devices*. Wiley, 2009.

[71] Takashi Takahashi et al. "Gas and solid phase photoelectron spectra of 5, 6, 11, 12-tetraphenylnaphthacene (rubrene)." In: *Bulletin of the Chemical Society of Japan* 52.2 (1979), pp. 380–382.

[72] J Takeya et al. "Effects of polarized organosilane self-assembled monolayers on organic single-crystal field-effect transistors". In: *Applied physics letters* 85.21 (2004), pp. 5078–5080.

[73] J Thornton. "Physical vapor deposition". In: *Noyes Data Corporation, Noyes Publications, Semiconductor Materials and Process Technology Handbook for Very Large Scale Integration(VLSI) and Ultra Large Scale Integration(ULSI),* (1988), pp. 329–454.

[74] Silvia Trabattoni et al. "Substrate Selection for Full Exploitation of Organic Semiconductor Films: Epitaxial Rubrene on β-Alanine Single Crystals". In: *Advanced Materials Interfaces* 2.18 (2015).

[75] S Uttiya et al. "Connecting molecule oxidation to single crystal structural and charge transport properties in rubrene derivatives". In: *Journal of Materials Chemistry C* 2.21 (2014), pp. 4147–4155.

[76] Brian J Walker et al. "Singlet exciton fission in solution". In: *Nature chemistry* 5.12 (2013), pp. 1019–1024.

[77] Qi Wang and Howard M Branz. "Exciton splitting and carrier transport across the amorphous-silicon/polymer solar cell interface". In: *Applied Physics Letters* 89 (2006), p. 252102.

[78] Xiaodong Wang et al. "A diaminomaleonitrile derivative as a new dopant for red-light-emitting electroluminescent device". In: *Journal of Physics D: Applied Physics* 36.15 (2003), p. 1789.

[79] Jennifer Weinberg-Wolf. "Optical characterization of organic semiconducting single crystals". PhD thesis. University of North Carolina at Chapel Hill, 2006.

[80] Paul H Wobkenberg et al. "Low-voltage organic transistors based on solution processed semiconductors and self-assembled monolayer gate dielectrics". In: *Applied Physics Letters* 93.1 (2008), p. 13303.

[81] Cathy Y Wong et al. "Exciton dynamics reveal aggregates with intermolecular order at hidden interfaces in solution-cast organic semiconducting films". In: *Nature communications* 6 (2015).

[82] Sang Yoon Yang et al. "Detection of transmitter release from single living cells using conducting polymer microelectrodes". In: *Advanced Materials* 23.24 (2011).

[83] Gunsu S. Yun, Setthivoine You, and Paul M. Bellan. "Large density amplification measured on jets ejected from a magnetized plasma gun". In: *Nuclear Fusion* 47.3 (2007), p. 181.

Glossary

Symbols

π bond 4
σ bond 4

Numbers

$^1/_f$ noise 24
2/3 - 3/2 rule 15, 50

A

absorption 12, 13, 36, 50, 51
absorption coefficient α 12, *see also* absorption
acceptance *see also* etendue
alternating current vi, 19
amplification 19, 27
angular dispersion 15, *see also* dispersion
anisotropy 7, 30, 52
antibatic 13, 36, 50, 52
atomic Z number 11
atomic force microscopy vi, 30
atomic orbital 4
Aufbau Principle 4

B

bandgap 5, 6
bandpass 16, 21, 22
bandstructure 5, 6, 8
bandwidth 16, 17, 22, 26, 33
Beer-Lambert law 8
benzene 4, 11
bias 18, 23
blaze 15, 22, 50
brick-wall packing 11

C

carbon vi, 4, 5, 11
charge-carrier 6–13, 24, 50
chopperwheel 21, 33
collecting power *see also* etendue
conduction band vi, 4, 5
conductivity 7, 9, 10, 12, 13
conjugated bond 4, 10
Coulomb 5, 6, 9
covalent 1, 4, 6
crystallinity 6
Curie temperature 18
Czerny-Turner 14, 21, 53

D

Davydov splitting 6, 8
default current vi, 19
defect 8
degeneracy 5
depletion region 17
detectivity 17
dielectric constant 9
diffraction 14, 15, 21, 22, 32, 34, 49, 50
diffraction equation 14, *see also* diffraction
dimer 6
dispersion 15, 22, 49
drop-casting 11, 29
dynamic reserve 27

E

etendue 16, 21
exciton 7, 9, 12, 13

F

F-number 16, 17, 22
Faraday cage 23
field-effect transistor vi, 31
fluorescence 13
flux 16, 17, 33
full width at half maximum vi, 16

G

gallium arsenide vi, 1
gallium nitride vi, 1
geometrical extent *see also* etendue
germanium vi, 10, 11
grating 14, 15, 22, 34, 50
groove density 14, 15

H

herringbone packing 11
highest occupied molecular orbital vi, 5
hole 5, 8, 9, 12, 17, 18
hopping transport 7

I

impedance 53
inkjet printed vi, 7, 29

irradiance E_e 33, 34, 53

J

Johnson noise 23, 24, 35

K

Kekulé structure 4

L

lead zirconate titanate vi, 18
lifetime 9, 12, 13
linear dispersion 15, *see also* dispersion
low-pass vi, 19, 26
lowest unoccupied molecular orbital vi, 5

M

magnification 17, 22, 53
mercury vi, 31
mobility 7, 8, 10, 11, 30
molecular orbital 5, 6, 8
monochromator 14, 15, 21, 22, 31, 33, 49, 50, 53
morphology 7, 29, 47, 51

N

noise equivalent power vi, 17
nonlinear photocurrent 13, 23, 50
numerical aperture vi, 16
Nyquist noise *see also* Johnson

O

organic field-effect transistor vi, 2
organic light emitting diode vi
organic molecular beam epitaxy vi, 29
organic semiconducting single crystal vi, 7
oxidation 2, 7, 8, 10, 13, 50, 52

P

p **orbital** 4
p-n junction 7, 17
pentacene 9, 11, 13
phase-locked-loop vi, 26
phase-sensitive detector vi, 19
phosphorescence 13
photoconductivity 12
photoconductor 12
photocurrent vi, 12
photodiode vi, 17
photovoltaic 18
physical vapour deposition vi, 10
pink noise *see also* $1/f$ noise
polarization 15, 18, 50, 53
polaron 6
polycrystalline 10
polyethylene terephthalate vi, 2
Poole-Frenkel 7
pyroelectric detector vi, 18
pyroelectricity 18

Q

quartz tungsten halogen vi, 21

R

Rayleigh criterion 15
reciprocal linear dispersion 15, *see also* dispersion
recombination 9, 13, 18, 50
recombine 5, 9, 12, 17, *see also* recombination
refractive index 16
resolution 14–16, 36–41, 49, 52
resolving power 16
responsivity 16, 17, 33
root-mean-squared vi, 19
rubrene 9, 10, 13, 29, 30, 50–52

S

s **orbital** 4
Savitzky-Golay smoothing algorithm 34, 44
shot noise 24
shunt resistance 23, 28, 35, 53
silicon vi, 1, 9, 10, 57
single crystal vi, 7, 29
singlet 9
solid angle 16, 17
spectral resolution 15, *see also* resolution
spectroscopy 14
standard deviation vi, 49
symbatic 13, 36, 50, 52

T

thermal noise *see also* Johnson
thin film 7, 29, 30, 45, 47, 50, 52
throughput 21, *see also* etendue
time constant 26, 28
TIPG pentacene vi, 11, 29
TIPS pentacene vi, 11, 29
transistor-transistor logic vi, 26
trap 8, 12, 13
triplet 9, 13

U

ultraviolet enhanced vi, 31

V

valence band vi, 4, 5
Van der Waals 4–6, 8

W

white noise *see also* Johnson

X

X-ray 1, 2, 11

Z

Z number *see also* atomic Z number